HIGH-RESOLUTION INFRARED SPECTROSCOPY: JET-COOLED HALOGENATED METHYL RADICALS AND REACTIVE SCATTERING DYNAMICS IN AN ATOM + POLYATOM SYSTEM

by

ERIN SUE WHITNEY
B.A., Williams College, 1996

A thesis submitted to the
Faculty of the Graduate School of the
University of Colorado in partial fulfillment
of the requirement for the degree of
Doctor of Philosophy
Department of Chemistry and Biochemistry
2006

UMI Number: 3207681

ProQuest Information and Learning Company
300 North Zeeb Road
P.O. Box 1346
Ann Arbor, MI 48106-1346

This thesis for the Doctor of Philosophy degree
entitled:

High resolution infrared spectroscopy: Jet cooled halogenated methyl radicals and reactive scattering dynamics in an atom + polyatom system

written by Erin Sue Whitney
has been approved for the Department of Chemistry and Biochemistry
by

_____

David J. Nesbitt

_____

Veronica M. Bierbaum

Date _____

Whitney, Erin S. (Ph.D., Chemistry)

High-Resolution Infrared Spectroscopy: Jet-cooled halogenated methyl radicals and reactive scattering dynamics in an atom + polyatomic system

Thesis directed by Professor David J. Nesbitt.

This thesis describes a series of projects whose common theme comprises the structure and internal energy distribution of gas-phase radicals. In the first two projects, shot noise-limited direct absorption spectroscopy is combined with long path-length slit supersonic discharges to obtain first high-resolution infrared spectra for jet-cooled CH_2F and CH_2Cl in the symmetric and antisymmetric CH_2 stretching modes. Drawing motivation from the question of the equilibrium structures of halogen-substituted methyl radicals, spectral assignment yields refined lower and upper state rotational constants, as well as fine-structure parameters from least-square fits to the sub-Doppler lineshapes for individual transitions. High-level CCSD(T) calculations extrapolated to the complete basis set (CBS) limit confirm the existence of a non-planar ($\theta = 29^\circ$) CH_2F equilibrium structure with a 132 cm^{-1} barrier to planarity and a vibrational bend frequency of 276 cm^{-1}. Similar calculations for CH_2Cl predict a slightly nonplanar equilibrium structure ($\theta = 11^\circ$) with a vibrationally adiabatic one-dimensional treatment of the bend coordinate yielding a fundamental anharmonic frequency (393 cm^{-1}). Both sets of calculations are in excellent agreement with previous studies.

More interesting, however, are the unexpected intensity ratios of the symmetric vs. antisymmetric bands for CH_2F and the absence of an antisymmetric

band for CH_2Cl. While a simple bond-dipole picture predicts a ratio of 1:3 for the symmetric vs. antisymmetric intensities, the experimentally observed value for CH_2F is ~2:1. This ratio is confirmed by DFT [B3LYP/aug-cc-pVTZ] calculations in a novel albeit indirect probe of the effective non-planarity for CH_2F. For CH_2Cl, similar DFT calculations predict a *30-fold* decrease between the intensity of the symmetric and antisymmetric CH_2 stretches, leading to the postulation of a nearly perfect cancellation of antisymmetric stretch intensity transition moment with chlorination.

These two projects are followed by an investigation utilizing a well-characterized radical source, F, in a reaction with ethane to form HF and ethyl radical. The *non-radical* HF product is detected directly through similar high-resolution infrared absorption methods as described above, and its analysis is used to make inferences about the internal energy redistribution of the other *radical* fragment, ethyl. State-to-state reaction dynamics under single collision conditions are interpreted in the context of a simple impulsive model based on conservation of linear/angular momentum yields predictions in good agreement with experiment. Deviations from the model indicate only minor excitation of the ethyl vibrations, in contrast with a picture of extensive intramolecular vibrational energy flow but consistent with Franck-Condon excitation of the methylene CH_2 bending mode. The results suggest a relatively simple dynamical picture for exothermic atom + polyatomic scattering, i.e., that of early barrier dynamics in atom + diatom systems but modified by impulsive recoil coupling at the transition state between translational/rotational degrees of freedom.

DEDICATION

To women in science

ACKNOWLEDGMENTS

Graduate school has been a long and twisting path for me, and one full of personal and professional challenges. I am grateful to my advisor, David Nesbitt, for facilitating a graduate experience which has taught me scientific discipline and inner fortitude. My fellow group members and the amazing JILA support staff have provided invaluable camaraderie and help. Special thanks go to Brad Perkins and Tom Baker for their comic relief and encouragement, as well as to the fearless and amazing women of our research group for their personal examples. Margaret Murnane, Veronica Vaida, Carl Lineberger, Veronica Bierbaum, and especially Anne McCoy have cheered me on and offered invaluable expertise.

Outside the academic setting, I owe more than I can express to Julie Emmerman, truly an earthbound angel, for helping me to more fully understand, love, and believe in myself and others. I have laughed, cried, and been immeasurably sustained by wonderful girlfriends – Stacey Quesada, Dianne Ahmann, Cornelia Alden, Elizabeth Pike, Deb Casher, and others too numerous to list. So many people and experiences have inspired and shaped my journey here in Boulder.

I thank my family for their unconditional support over the years, especially during these last months. My precocious malamute, Kenai, has continually kept me grounded and sane by reminding me of simple joys such as dawn walks in the Canyon and long trail runs in the mountains. And finally, to Frank Witmer, my best friend and partner in life's adventures, thank you for your unwavering support, patience, love, and enthusiasm.

CONTENTS

CHAPTER	PAGE
1. INTRODUCTION	1
References for Chapter 1	8
2. JET-COOLED INFRARED SPECTROSCOPY IN SLIT SUPERSONIC DISCHARGES: SYMMETRIC AND ANTISYMMETRIC CH_2 STRETCHING MODES OF FLUOROMETHYHL (CH_2F) RADICAL	10
2.1 Introduction	10
2.2 Experiment	16
2.3 Results and Analysis	18
2.3.1 *Symmetric CH_2 stretch line center assignments*	18
2.3.2 *Antisymmetric CH_2 stretch line center assignments*	23
2.3.3 *Fine and hyperfine structure and analysis*	26
2.4 Discussion	30
2.4.1 *Boltzmann intensity analysis*	31
2.4.2 *Complete Basis Set (CBS) inversion potential for CH_2F*	36
2.4.3 *Intensity-based vidence for a nonplanar equilibrium geometry*	40
2.5 Summary and Conclusion	43
References for Chapter 2	46

3. HIGH-RESOLUTION INFRARED STUDIES IN SLIT-JET DISCHARGES: SYMMETRIC CH_2 STRETCH EXCITATION OF JET-COOLED CH_2Cl RADICAL 49

3.1 Introduction 49

3.2 Experiment 54

3.3 Results and Analysis 56

3.3.1 *Symmetric CH_2 stretch line center assignments* 56

3.3.2 *Fine and hyperfine structure and analysis* 64

3.4 Discussion 67

3.4.1 *CCSD(T) Complete Basis Set (CBS) bending potential* 67

3.4.2 *Vibrational band intensities* 71

3.5 Summary and Conclusion 79

References for Chapter 3 82

4. REACTIVE SCATTERING DYNAMICS IN ATOM + POLYATOM SYSTEMS: $F + C_2H_6 \rightarrow HF(v,J) + C_2H_5$ 85

4.1 Introduction 85

4.2 Experiment 90

4.3 Results and Analysis 92

4.3.1 *Data collection* 92

4.3.2 *Nascent column-integrated densities* 94

4.3.3 *High-resolution infrared dopplerimetry* 97

4.4 Discussion 101

4.4.1 *Impulsive model (rotation/translation)* 101

4.4.2 *Density-to-flux transformation* 104

4.4.3 *Nascent HF (v,J) populations* 105

4.4.4 *Dynamic Franck-Condon impulsive model* 110

4.5 Summary and Conclusion 113

References for Chapter 4 115

BIBLIOGRAPHY 119

APPENDIX 127

A. PROCESSING AND CONCATENATION PROGRAMS 128

A.1 Introduction 128

A.2 Pre-processing of data 129

A.3 Fringe counting and spreadsheet tabulations 131

A.4 Concatenation with Fortran programs 135

A.5 Concatenation with Origin scripts 136

B. SPECTRAL PREDICTION AND LEAST-SQUARES FITTING PROGRAMS 141

B.1 Predictions 141

B.2 Least-squares fitting programs 143

B.3 Gaussian convolutions of predictions using Origin programs 144

C. LEAST-SQUARES FITTING PROGRAM FOR *LINESHAPES* 147

TABLES

CHAPTER 2

2.1 Observed fine/hyperfine free line centers and (obs-calc) values from Watson asymmetric top Hamiltonian least-squares fit to the symmetric stretch (ν_1) band of CH_2F. 22

2.2 Observed fine/hyperfine free line centers and (obs-calc) values from Watson asymmetric top Hamiltonian least squares fit to the antisymmetric stretch (ν_5) band of CH_2F. 24

2.3 Simultaneous least-squares fit results for CH_2 symmetric and antisymmetric stretch rotational constants (in cm^{-1}), with 1σ uncertainties in parentheses. 26

2.4 Least-squares results for spin rotation fine-structure constants obtained from simultaneous fit to symmetric and antisymmetric CH_2 stretch line contours, with 1σ uncertainties in parentheses. Ground state fine/hyperfine constants, as well as excited-state hyperfine constants are held fixed at values from microwave studies.{Endo, 1983} 30

CHAPTER 3

3.1 Transition frequencies and least-squares fit for the $CH_2{}^{35}Cl$ symmetric stretch 61

3.2 Transition frequencies and least-squares fit for the $CH_2{}^{37}Cl$ symmetric stretch 63

3.3 Least-squares fitting results for the symmetric CH_2 stretch line centers in $CH_2{}^{35}Cl$ and $CH_2{}^{37}Cl$. The uncertainties in parenthesis represent one standard deviation from the least-squares fit to the Watson asymmetric top Hamiltonian. 64

3.4 Least-squares fitting results for the CH_2 symmetric stretch fine-structure constants. The uncertainties in parentheses represent one standard deviation from the least-squares fit to the effective Hamiltonian detailed in the text. 67

CHAPTER 4

4.1 *Ab initio* results for H-C-C bond angle θ, moment of inertia I, and distance to center-of-mass λ at transition state geometry. 112

FIGURES

CHAPTER 2

2.1 One-dimensional potential energy function, illustrating inversion of CH_2F over a symmetric barrier and orientation of molecular axes. 15

2.2 Schematic of the slit-jet discharge spectrometer apparatus. 17

2.3 Sample CH_2F data in the CH_2 symmetric stretch region, comparing experimental (top) to simulated (bottom) spectra predicted from the least-squares fits. 20

2.4 Sample Q branch CH_2F data for CH_2 antisymmetric stretch, comparing experimental (top) to simulated (bottom) spectra predicted from the least-squares fits and illustrating fully resolved fine structure. 23

2.5 Sample data and contour predictions for the $2_{11} \leftarrow 2_{02}$ transition, systematically including fine and hyperfine terms in the Hamiltonian. a) Asymmetric top only. b) Asymmetric top plus spin rotation. c) Asymmetric top, spin rotation and hyperfine terms. d) Experimental data. 29

2.6 Boltzmann plot for ground state rotational populations monitored in symmetric and antisymmetric CH_2 stretch modes, verifying jet-cooled conditions [T_{rot} = 20.8(8) K] in the slit discharge and demonstrating a 1.8(2):1 ratio between the two bands. 33

2.7 Cartoon illustrating the competition between “bond dipole” and “charge sloshing” contributions to symmetric and antisymmetric CH stretch intensities in CH_2F. 35

2.8 One-dimensional potential energy curve (solid line) obtained from CCSD(T) complete basis set (CBS) calculations (see text for details), with zero-point energies in all remaining coordinates included adiabatically (dashed line). Ground and excited state eigenvalues (dotted line) and eigenfunctions (solid line) from a multidimensional Rush-Wiberg analysis are also indicated, which predict the $\nu_4=1\leftarrow0$ anharmonic bending frequency to be 276 cm^{-1}. 38

2.9 Calculated intensity ratios for symmetric and antisymmetric CH_2 stretches in CH_2F, highlighting a remarkably strong dependence on inversion angle. Note the essentially constant ratio predicted for CH_2D. Though large amplitude averaging is clearly important, the experimental intensity ratio of 1.8(2):1 for CH_2F is qualitatively consistent with the potential surface equilibrium angle of $\theta = 29^o$. 43

CHAPTER 3

3.1 Sample spectral data (a) for selected P-branch transitions in the CH_2 symmetric stretch band of CH_2Cl, compared with a calculated spectrum from the full least squares fit. 58

3.2 Comparison between high resolution predictions (a-c) and experiment (d) for a sample symmetric stretch rovibrational transition ($3_{13} \leftarrow 2_{12}$) of CH_2Cl. The simulations begin with a pure asymmetric top transition (i.e. $S = I_{Cl} = I_H = 0$) (a), successively including fine (b) and hyperfine (c) interaction terms in the Hamiltonian. 66

3.3 One dimensional potential energy curve from CCSD(T)/AVnZ/CBS calculations, adiabatically corrected for zero point energy in all remaining non-bend coordinates. Also shown are ground and first excited vibrational state (v_4) eigenfunctions and eigenenergies, calculated via methods of Rush and Wiberg and explicitly including G matrix element dependence on the bend angle (see text for details). 70

3.4 Comparison of one dimensional potential energy curves from CCSD(T)/AVnZ/CBS calculations, for CH_3, CH_2Cl, and CH_2F. Note the clear progression toward a non-planar equilibrium geometry, due to increasing sp^3 vs sp^2 hybridization of the carbon atom with increasing electronegativity of the halogen substituent. 72

3.5 Boltzmann temperature analysis of the $CH_2{}^{35}Cl$ symmetric stretch band verifying rotational equilibration to $T_{rot} \approx 15$ K in the slit jet. 74

3.6 Predicted band intensities of CH_2 symmetric and antisymmetric stretch vibrations for CH_2Cl, CH_2F, and CH_2D as a function of inversion angle. 75

3.7 Comparison of symmetric (I_{sym}) and asymmetric (I_{asym}) stretch band intensities for CH_2D, CH_2Br, CH_2Cl, and CH_2F. Note the dramatic minimum in I_{asym} for CH_2Cl due to near cancellation of bond-dipole and "charge-sloshing" contributions, which becomes nonzero for either greater (CH_2F) or weaker (CH_2Br) electron withdrawing nature of the halogen substituent. 79

CHAPTER 4

4.1 Energetics for the F + C_2H_6 reaction. The sum of reaction exothermicity ($\Delta H \approx 37.8$) and center-of-mass collision energy ($E_{com} \approx 3.2$) yields 41(1) kcal/mol, allowing energetic access to product states as high as HF(v=3,$J \approx 13$). 93

4.2 Nascent column-integrated densities for formation of HF(v,J) in specific rovibrational states from single collision F + C_2H_6 reactive events at E_{com} = 3.2(6) kcal/mol. Note the extraction of *absolute* densities that are feasible in direct IR laser studies due to measurement of *absolute* absorbances. 96

4.3 Sample high resolution profiles of HF(v,J) nascent product states from the F + C_2H_6 reaction, indicating strongly competing Doppler structures due to (i) stimulated absorption [HF($v = 4 \leftarrow$

3),$R(0)$], (ii) competition between stimulated emission and stimulated absorption [HF($v = 3 \leftarrow 2$),$R(2)$], and (iii) stimulated emission [HF($v = 2 \leftarrow 1$),$R(1)$]. Solid lines are least-squares fits to Gaussian line-shape functions, revealing velocity-dependent population-inversion effects dependent on upper- and lower-state translational energies. 98

4.4 Recoil energy plots from high-resolution Dopplerimetry of single HF(v,J) quantum states. The data indicate a clear linear dependence between (i) $\langle E_{HF}(trans)\rangle \approx 3\langle E_z\rangle$ and (ii) $E_{avail} = E_{tot} - E_{HF}(v,J)$, i.e., the remaining energy available for both HF/ethyl translation and vibration/rotation/translational excitation of the ethyl radical. Note the excellent qualitative agreement with simple impulsive model predictions. 100

4.5 Cartoon depiction of the rotation/translation impulsive model, based purely on the conservation of linear and angular momentum. The angle (θ) and moment arm (λ) for delivering torque are calculated from CCSD(T) *ab initio* calculations of the transition state (see Table 4.1). 102

4.6 Nascent product-state fluxes (in relative units) based on Monte Carlo modeling of the density-to-flux transformation. Note the modest sensitivity of these fluxes to modeling of the differential cross sections. 106

4.7 Comparison of current HF($\nu = 2,J$) nascent fluxes with previous vibrational "arrested relaxation" studies of Bogan and Setser. Agreement is generally quite good, though evidence for partial rotational relaxation is present. However, the nascent vibrational populations from these previous studies, summed over final rotational states, are in excellent agreement with the current collision-free results. 109

APPENDIX

A.1 A sample "scanlist" file. 132

CHAPTER 1

INTRODUCTION

The name "free radicals" may suggest a quirky group of political intellectuals, a similarity to a common local bumper sticker advocating freedom for a particular Himalayan country, or even a reference to a backcountry ski technique that is also known to “free the mind.” But, in fact, free radicals comprise a group of chemical species that is highly reactive, short-lived, and characterized by one or more unpaired electrons. Often used interchangeably with the term “transient species,” the idea of an intermediate, short-lived chemical species first surfaced as a way to explain chemical reaction mechanisms. As such, their existences were at first only hypothetical.[1] It is now known that free radicals, in particular, last only for the length of time it takes for their constituent atoms to rearrange themselves with other molecules into new molecules – a few millionths of a second – making it extremely difficult to obtain a spectrum of such fleeting entities. To be fair, the classification of

"free radicals" does also include several stable species such as the ground states of O_2, NO, and NO_2. But, in general, the term is not associated with stability.[2]

The first recorded measurement of a radical species was in the emission spectrum of a Bunsen flame by Wollaston in 1802 and then again by Swan in 1857.[2] However, the more general study of radicals did not gain prominence until the advent of significant advances in the understanding of molecular spectroscopy in the early part of the 20th century.[3-5] The chemical detection and, more importantly, *identification* of molecular free radicals in the gas phase was first demonstrated in the classic thermal decomposition experiments of lead tetramethyl by Paneth and Hofeditz in 1929,[6] validating the incorporation of radicals into the mechanism of chemical reactions.[7] Subsequently, their study gained particular prominence through the work of Nobel Prize winner Gerhard Herzberg,[8] among others, with his pioneering investigations of methyl and methylene radical – well known from organic chemistry. His work, in turn, helped stimulate a resurgence of investigations into the chemical reactions of gases, most notably by Polanyi,[9] and followed by numerous others.

Today, radicals are recognized as important species in numerous chemical processes in both the laboratory as well as industry. Reactions involving radicals span the range from fundamental gas reactions to condensed phase processes and occur in flames, propellant systems, atmospheric pollution, chemical vapor deposition, and plasma processing.[10,11] These chemical processes consist of a complex sequence of interrelated reactions in which molecular fragments play crucial

roles, often significantly influencing product distribution and yield even when present in only very small concentrations.

Along these lines, the central theme of the work in this thesis is that of transient phenomena, and specifically polyatomic gas-phase radicals. In our studies, they are studied both directly and indirectly using high-resolution infrared spectroscopic methods. This thesis begins with the two most recent studies, utilizing *direct* absorption high-resolution infrared spectroscopy of CH_2F and CH_2Cl radicals. Following that, the final project presents a nice parallel to the historical resurgence of gas-phase dynamics investigations after pioneering free radical studies. This particular project follows the reaction of a well-characterized fluorine radical source with ethane, and focuses on the detection of the *non-radical* product HF to make inferences about the internal energy redistribution in the other product *radical* fragment, ethyl.

The first project, described in Chapter 2, uses a combination of shot noise limited direct absorption spectroscopy with long path length slit supersonic discharges to obtain the first high resolution infrared spectra for jet cooled CH_2F radicals in the symmetric (ν_1) and antisymmetric (ν_5) CH_2 stretching modes. This work builds directly on Herzberg's and others' investigations of the methyl radical.[12-16] In ESR experiments by Fessenden and Schuler, methyl radical was determined to have an effectively planar structure, at least vibrationally averaged over the ground state wave function.[17] However, other spectroscopic efforts demonstrated that the fully-fluorinated methyl radical, i.e. CF_3, has a pyramidal structure in its ground electronic state.[14,18-23] Stated simply, such changes in equilibrium geometry reflect a

competition between sp^2 (planar) and sp^3 (pyramidal) hybridization of the C atom as a function of electron-donating (or withdrawing) group substitution.

As such, our experiments with CH_2F probe the effect of mono-halogen substitution in the methyl radical. Spectral assignment has yielded refined lower and upper state rotational constants, as well as fine-structure parameters, from least-squares fits to the sub-Doppler line shapes for individual transitions. Indeed, the rotational constants provide indications of large amplitude vibrational averaging over a low barrier double minimum inversion bending potential. This is further confirmed by high level CCSD(T) calculations, extrapolated to the complete basis set (CBS) limit, which predict a non-planar equilibrium structure ($\theta \approx 29^o$, where θ is defined as 180^o minus the angle between the C-X bond and the CH_2 plane)) with a 132 cm^{-1} barrier to planarity, and a vibrational bend frequency ($\nu_{bend} \approx 276$ cm^{-1}) in excellent agreement with previous microwave studies by Hirota and coworkers ($\nu_{bend} = 300(20)$ cm^{-1}).[24-26] The nearly 2:1 ratio of absorption intensities for the symmetric vs. antisymmetric bands is in good agreement with DFT calculations, but in 6-fold contrast with simple local mode CH_2 bond dipole predictions of 1:3. This arises from a surprisingly strong dependence of the symmetric stretch intensity on the inversion bend angle and provides further experimental support for a non-planar equilibrium structure.

The anomalous ratio between the symmetric and antisymmetric stretch intensities in CH_2F provides motivation for the next project, described in Chapter 3. In this second study, the effect of the halogen atom identity is probed, moving from *fluorine*-substituted methyl radical to *chlorine*-substituted methyl radical, and first

high-resolution infrared spectra are presented for jet-cooled $CH_2{}^{35}Cl$ and $CH_2{}^{37}Cl$ radicals in the symmetric (ν_1) CH_2 stretching mode. A detailed spectral assignment yields refined lower- and upper- state rotational constants, as well as fine-structure spin rotation parameters from least-squares fits to the sub-Doppler line shapes for individual transitions. The rotational constants are consistent with a nearly planar structure, but do not exclude substantial large-amplitude-bending motion over a small barrier to planarity accessible with zero-point excitation. High level coupled cluster (singles/doubles/triples) calculations, extrapolated to the complete basis set (CBS) limit, predict a slightly nonplanar equilibrium structure ($\theta \sim 11$ degrees), with a 1-D vibrationally adiabatic treatment of the bend coordinate yielding a $v = 1 \leftarrow 0$ anharmonic frequency (393 cm^{-1}) in excellent agreement with matrix studies ($\nu_{bend} \sim$ 400 cm^{-1}). The antisymmetric CH_2 stretch vibration is not observed despite high sensitivity detection (S/N > 20:1) in the symmetric stretch band. This is consistent with density functional theory (DFT) intensity calculations indicating a > 35-fold smaller antisymmetric stretch transition moment for CH_2Cl, and yet contrasts dramatically with high-resolution infrared studies of CH_2F radical, for which both symmetric and antisymmetric CH_2 stretches are observed in a nearly 2:1 intensity ratio. A simple physical analysis is presented based on a competition between bond dipole and "charge sloshing" contributions to the transition moment, which nicely explains the trends in CH_2X symmetric vs asymmetric stretch intensities as a function of electron withdrawing group (X=D, Br, Cl, F).

Although conducted earlier in chronology than the first two projects, the final project, described in Chapter 4, is a natural extension of the first two projects. The

investigation uses a well-characterized fluorine radical source to react with ethane rather than as the object of the study itself. The *non-radical* HF product is then directly detected through similar high-resolution infrared absorption methods and used to make inferences about the internal energy redistribution of the other *radical* fragment, ethyl. State-to-state scattering dynamics of $F + C_2H_6 \rightarrow HF(v,J) + C_2H_5$ have been investigated at E_{com} = 3.2(6) kcal/mol under single collision conditions, via detection of nascent rovibrationally resolved HF(v,J) product states with high resolution infrared laser absorption methods. State-resolved Doppler absorption profiles are recorded for multiple HF(v,J) transitions originating in the v=0, 1, 2, 3 manifold, analyzed to yield absolute column-integrated densities via known HF transition moments, and converted into nascent probabilities via density-to-flux analysis.

The spectral resolution of the probe laser also permits Doppler study of translational energy release into quantum-state-resolved HF fragments, which reveals a remarkable linear correlation between (i) HF(v,J) translational recoil and (ii) the remaining energy available, $E_{avail} = E_{tot} - E_{HF(v,J)}$. The dynamics are interpreted in the context of a simple impulsive model based on conservation of linear/angular momentum that yields predictions in good agreement with experiment. Deviations from the model indicate only minor excitation of ethyl vibrations, in contrast with a picture of extensive intramolecular vibrational energy flow but consistent with Franck-Condon excitation of the methylene CH_2 bending mode. The results suggest a relatively simple dynamical picture for exothermic atom + polyatomic scattering, i.e., that of early barrier dynamics in atom + diatom systems but modified by impulsive

recoil coupling at the transition state between translational/rotational degrees of freedom.

References for Chapter 1

[1] E. Hirota, Chem. Rev. **92**, 141 (1992).

[2] J. C. Whitehead, Rep. Prog. Phys. **59**, 993 (1996).

[3] R. S. Mulliken, Phys. Rev. **30**, 785 (1927).

[4] W. E. Pretty, Proc. Phys. Soc. **40**, 71 (1928).

[5] F. Hund, 36, 657 (1926).

[6] F. Paneth and W. Hofeditz, Ber. Chem. Ges. **62**, 1335 (1929).

[7] F. O. Rice, J. Am. Chem. Soc. **53**, 1959 (1931).

[8] G. Herzberg, *The Spectra and Structure of Simple Free Radicals*. (Cornell University Press, Ithaca, NY, 1971).

[9] J. C. Polanyi, Accts Chem. Rsrch. **5**, 161 (1972).

[10] M. E. Jacox, J. Phys. Chem. Ref. Data **32**, 1 (2003).

[11] J. G. Anderson, Ann. Rev. Phys. Chem. **38**, 489 (1987).

[12] G. Herzberg, *Molecular Spectra and Molecular Structure III. Electronic Spectra and Electronic Structure of Polyatomic Molecules*. (Van Nostrand, New York, 1966).

[13] S. Davis, Ph.D. Thesis, University of Colorado (1999).

[14] K. Morokuma, L. Pedersen, and M. Karplus, J. Chem. Phys. **48**, 4801 (1968).

[15] D. M. Schrader and M. Karplus, J. Chem. Phys. **40**, 1593 (1964).

[16] C. Yamada, E. Hirota, and K. Kawaguchi, J. Chem. Phys. **75**, 5256 (1981).

[17] R. W. Fessenden and R. H. Schuler, J. Chem. Phys. **39**, 2147 (1963).

[18] G. A. Carlson and G. C. Pimentel, J. Chem. Phys. **44**, 4053 (1966).

[19] F. Bernardi, W. Cherry, S. Shaik, and N. D. Epiotis, J. Am. Chem. Soc. **100**, 1352 (1978).

[20] Y. Endo, C. Yamada, S. Saito, and E. Hirota, J. Chem. Phys. **77**, 3376 (1982).

[21] R. W. Fessenden and R. H. Schuler, J. Chem. Phys. **43**, 2704 (1965).

[22] J. Nolte and H. G. Wagner, Ber. Bunsenges. Phys. Chem. **101**, 1421 (1997).

[23] C. Yamada and E. Hirota, J. Chem. Phys. **78**, 1703 (1983).

[24] J. W. Hudgens, C. S. Dulcey, G. R. Long, and D. J. Bogan, J. Chem. Phys. **87**, 4546 (1987).

[25] Y. Endo, C. Hamada, S. Saito, and E. Hirota, J. Chem. Phys. **79**, 1605 (1983).

[26] S. V. Levchenko and A. I. Krylov, J. Phys. Chem. A **106**, 5169 (2002).

[27] L. Andrews and D. W. Smith, J. Chem. Phys. **53**, 2956 (1970).

[28] Y. Endo, S. Saito, and E. Hirota, Can. J. Phys. **62**, 1347 (1984).

[29] M. E. Jacox and D. E. Milligan, J. Chem. Phys. **53**, 2688 (1970).

[30] J. P. Michaut and J. Roncin, Chem. Phys. Lett. **12**, 95 (1971).

CHAPTER 2

JET-COOLED INFRARED SPECTROSCOPY IN SLIT SUPERSONIC DISCHARGES: SYMMETRIC AND ANTISYMMETRIC CH_2 STRETCHING MODES OF FLUOROMETHYHL (CH_2F) RADICAL

2.1 Introduction

Free radicals, with their characteristic unpaired electron spin and resulting enhanced reactivity, play essential roles as transient intermediates in a wide range of chemical reactions. These reactions encompass both fundamental gas and condensed phase processes in the realms of atmospheric chemistry and pollution, molecular biology, combustion, propellant systems, and chemical vapor deposition.[1,2] Indeed, radical intermediates were first proposed as hypothetical species to explain reaction mechanisms, spurring a half-century of development and refinement of numerous sophisticated experimental methods to confirm their transient existence and precisely measure them.[3] Spectroscopic probes of the vibrational, rotational, and even spin

angular momentum degrees of freedom provide a particularly detailed view into the mechanical and electronic structure of these ubiquitous, albeit elusive, species.

One of the early developments along these lines was flash photolysis,[4] which in combination with electronic spectroscopy, enabled the production of radical species in sufficient concentrations for spectral observation and lifetime determination.[5] Subsequent introduction of matrix isolation techniques[6] allowed the study of gaseous radicals deposited on a cold surface with a buffer gas or generated directly in an inert gas matrix. Such methods for trapped and low temperature radical species have proven an exceptionally productive source for probing with visible, infrared, and electron spin resonance (ESR) or electronic paramagnetic resonance (EPR) spectroscopy.[7]

With enhancements in detection sensitivity, infrared spectroscopy of gas phase radical species became possible, with further high-resolution extension of microwave methods into the millimeter- and submillimeter-wave regions.[3] The use of fixed-frequency lasers also increased sensitivity and was combined with electric-field or magnetic-field tuning of molecular transitions in laser magnetic resonance (LMR).[8,9] Spectral ranges were increased with the development of tunable infrared sources, such as diode and color-center lasers, as well as nonlinear difference frequency generation methods.[3] In addition to experimental efforts, recently improved computational strategies have also informed the interaction between gas-phase and matrix isolation spectroscopists. Specifically, *ab initio* and density functional methods have achieved better estimations of structures and ground-state vibrational frequencies of small radical molecules, as surveyed by Byrd and co-workers in

2001.[10] Still, significant discrepancies exist between the most reliable computational methods and existing experimental data.

Of particular interest in the current study is the fluoromethyl radical, CH_2F. As a benchmark intermediate in the photodecomposition and oxidation of partially hydrogenated chlorofluorocarbons, it is one of a number of important sources of halogen atoms in the atmosphere.[11,12] Photodissociation of the fluoromethyl radical itself, as well as similar halomethyl radicals, may also compete with nonphotochemical decomposition pathways such as bimolecular reactions with other species.[13] Halomethyl radicals are products of radical attack (reaction with H or OH) on halomethanes, which are part of a family of halocarbons widely used as fire suppressants, solvents, and refrigerants.[14,15] The unreactive parent halocarbons can accumulate in the urban atmosphere and may be relevant to atmospheric ozone depletion and high global warming potentials.[16] Models of incomplete combustion processes, such as flame inhibition and waste incineration, or atmospheric chemistry involving halocarbons require accurate values of the thermodynamics and kinetics parameters of these molecules and their decomposition products.[14,17-20]

Experimental and theoretical investigations of the fluoromethyl radical have naturally emerged from the study of methyl radical and its family of halogen-substituted derivatives. Methyl radical was first identified by Fessenden and Schuler[21] using ESR and determined to have an effectively planar structure, at least vibrationally averaged over the ground-state wave function.[22] However, other spectroscopic efforts demonstrated that the fully fluorinated methyl radical, CF_3, has a pyramidal structure in its ground electronic state.[23-25] Stated simply, such changes

in equilibrium geometry reflect a competition between sp^2 (planar) and sp^3 (pyrimidal) hybridization of the C atom as a function of electron-donating (or withdrawing) group substitution. Indeed, this competition is clearly present even in the nominally "planar" (sp^2-hybridized) methyl radical. The sp^3 hybridization adds in a small double minimum contribution, which when summed with the more harmonic sp^2 contribution centered around planarity, results in an unusually flat inversion potential and therefore an anomalous progression of levels shifting strongly to the higher frequencies (i.e., negatively anharmonic) with increasing vibrational quantum number.[26] In fact, it is still somewhat controversial whether the equilibrium geometry of CH_3 is actually planar,[2] though the size of any putative barrier must be quite small with respect to the zero point energy. On the other hand, the stronger propensity for sp^3 hybridization in CF_3 results in a clear double minimum potential which, in combination with the much larger reduced mass, leads to significant localization of the wave function in a nonplanar geometry.

This qualitative difference in potential surface topology and vibrationally averaged geometry for "planar" CH_3 versus "pyramidal" CF_3 radical naturally raises interesting questions about the structure of partially substituted species such as CH_2F radical, which serves as a main focus of the current study. The history of the detection and analysis of the monofluoromethyl (CH_2F) radical is summarized nicely by Nolte.[27] Briefly, CH_2F was first detected in krypton and xenon matrices, again by Fessenden and Schuler.[24] Shortly thereafter, Jacox and others[28,29] identified the C-F stretching band in an argon matrix, and Raymond described the CH_2 scissors mode.[28] Mucha and co-workers made the first gas-phase detection of CH_2F radicals using far-

infrared laser magnetic resonance (FIR-LMR) spectroscopy and also hypothesized a near-prolate ground vibronic state.[30] Microwave spectroscopy studies identified A-type transitions out of the ground vibronic state as well as satellite transitions assigned as arising from a thermally excited inversion vibrational mode (ν_4) ≈ 300(30) cm^{-1}.[31,32] The ground state hyperfine structure was consistent with B_1 electronic symmetry, implying odd parity with respect to reflection through a planar geometry (as expected for a p-type unpaired radical center on the C atom). Hudgens and co-workers followed these efforts with the REMPI measurements of the out-of-plane vibrational frequency for ground-state CH_2F and CD_2F radicals and recommended a value of 260(30) cm^{-1} for CH_2F and 170(30) cm^{-1} for CD_2F.[33] Infrared diode laser spectra of CH_2F were also obtained by the Hirota group by exciting the CF-stretching mode (ν_3) and yielding A-type rovibrational transitions with resolved spin-rotation fine structure.[31,32] Only $\Delta K_a = 0$ transitions could be observed in these two studies because of dipole and dipole-derivative transition moments along the C-F bond. This precluded least-squares determination of the ground state A rotational constant, though sufficient asymmetric top $J_{Ka, Kc}$ lines were observed to provide good first estimates for structural purposes. No C-type transitions were reported in either study, consistent with a planar-averaged structure with vanishing dipole moment along the C-axis. These observations were all interpreted to be consistent with a vibrationally averaged planar CH_2F geometry, though the presence of a small barrier at the planar configuration could not be ruled out.

Interestingly, although spectroscopic experiments to date yield data consistent with *planar* geometries, *ab initio* theoretical efforts clearly predict a *nonplanar*

equilibrium structure.[26] Levchenko and Krylov reconcile these differences as the result of zero-point vibrational averaging over a shallow double minimum potential, which would also result in a large negative anharmonicity in the out-of-plane vibrational mode.[26] Additional information can be obtained in the CH_2 stretch vibrational spectral region, which represents the specific focus of this chapter. Here, transition dipole moment derivatives yield oscillator strength for both A-type (symmetric CH_2 stretch) and B-type (antisymmetric CH_2 stretch) bands (see Figure 2.1), which provides opportunity for direct spectroscopic determination of all three ground-state rotational constants, as well as fine structure spectral splittings resulting from the coupling of unpaired electron spin angular momentum and the end-over-end tumbling angular momenta.

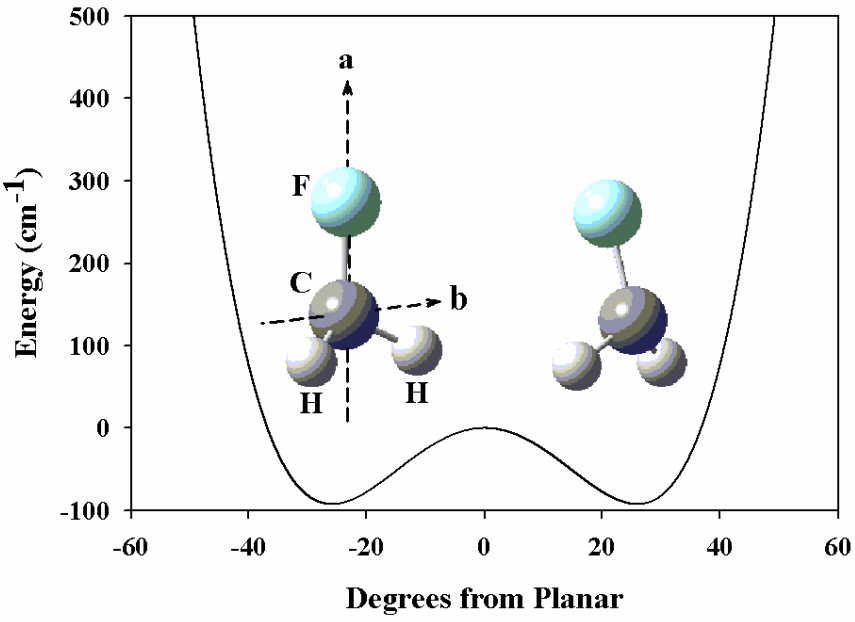

Figure 2.1 One-dimensional potential energy function, illustrating inversion of CH_2F over a symmetric barrier and orientation of molecular axes.

In this study, we utilize high-resolution infrared absorption spectroscopy coupled with slit-jet expansion methods to provide the first vibrational and rotational structure of both the symmetric (ν_1) and antisymmetric (ν_5) CH_2-stretching vibrational modes of the CH_2F radical. The organization of this chapter is as follows. Section 2.2 summarizes relevant experimental details of the slit-jet-cooled CH_2F discharge generation and concentration modulation laser spectroscopy. In Section 2.3, least-squares fittings of the spectra to a Watson asymmetric top Hamiltonian are presented which, under sub-Doppler conditions, also yields fully resolved fine and partially resolved hyperfine structure. Section 2.4 tackles a number of topics comprising a comparison of density-functional theory (DFT) calculations with experimental determinations of vibrational band intensities, the development of a one-dimensional (1D) CBS potential energy curve and associated wave functions, and the extraction of structural information. Section 2.5 summarizes and concludes the chapter.

2.2 Experiment

The slit-discharge laser spectrometer techniques have been discussed in previous papers;[34-37] the following description contains a brief summary relevant to the current study. Figure 2.2 shows a simplified diagram of the experimental apparatus. CH_2F radicals are produced by adiabatically expanding an optimal mixture of 0.5% CH_2F_2 in 70%/30% neon/helium buffer gas through a pulsed slit-jet (19 Hz, 500 μs pulse duration). The radicals are formed by electron dissociative attachment from neutral CH_2F_2 precursor by a 50 kHz square-wave-modulated discharge (500 V,

0.8 A) localized upstream of the expansion orifice. Radicals are probed by direct absorption of transmitted infrared laser light (tunable from 2500-5000 cm^{-1}) with a combination of time-domain gating and 50 kHz lock-in detection to eliminate low-frequency amplitude noise. At 600 Torr backing pressures and 4 cm x 300 μm slit orifice dimensions, one routinely obtains as many as 10^{13}-10^{14} radicals/cm^3 in the laser probe region ≈1 cm downstream.

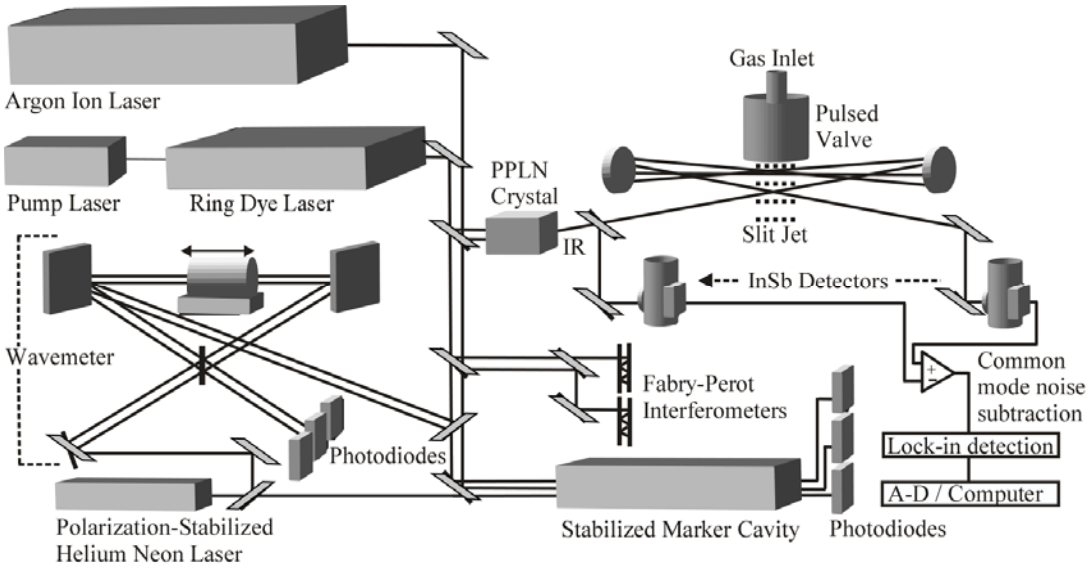

Figure 2.2 Schematic of the slit-jet discharge spectrometer apparatus.

The laser probe is produced via nonlinear difference-frequency generation of fixed-frequency single-mode argon ion laser light (514.5 nm) and tunable single-mode ring-dye laser light (R6G) in a temperature-controlled and heated periodically-poled $LiNbO_3$ (PPLN) crystal.[38] The resulting infrared light frequency is stabilized to a few MHz by servo-loop locking of the argon ion laser to a confocal Fabry-Perot etalon, which, in turn, is locked onto a polarization-stabilized He-Ne laser. Relative

frequencies are determined to 0.0001 cm^{-1} precision by monitoring dye laser transmission fringes on the same Fabry Perot etalon, with absolute frequencies determined by referencing to the R(0) methane absorption line[39] at 3028.7528 cm^{-1}.

The infrared light is split into reference and signal beams of roughly the same intensity, and the signal beam is multipassed in a Herriot cell 16 times through the long axis of the slit-jet expansion region. Both the exiting signal beam and the reference beam are focused onto matched InSb photovoltaic detectors. Detection sensitivities of $5 \times 10^{-7}/Hz^{1/2}$ are achieved through elimination of common-mode infrared noise by subtracting signal and reference beams under servo-loop control. Peak absorbances in the CH_2F spectra observed under these expansion conditions are on the order of 0.3%, and peak signal-to-noise ratios are approximately 100:1.

2.3 Results and Analysis

2.3.1 Symmetric CH_2 stretch line center assignments

The choice of CH_2 stretch regions for high-resolution investigation requires some theoretical input. The spectral search area is initially guided by DFT calculations [B3LYP/G-311**6(3df,3pd)], where the harmonic predictions are scaled by $\nu_{exp}/\nu_{predict} = 0.9637$. This factor has been empirically benchmarked from a least-squares fit to CH and OH stretch band origins for ≈10 jet-cooled radical and molecular ion species.[40] Such methods predict symmetric and antisymmetric stretch band centers to be approximately 3044 cm^{-1} and 3209 cm^{-1}, respectively, with an estimated uncertainty of 10 cm^{-1}. Additional DFT calculations [B3LYP/AUG-cc-pVTZ] also predict the ratio of symmetric to antisymetric band intensities to be

$I_{sym}/I_{antisym}$ = 2.1. For later discussion, it is worth noting that this ratio differs substantially from the usual CH_2 bond dipole expectations, which predict a 6-fold smaller value of $I_{sym}/I_{antisym} \approx 1/3$. Based on these surprising intensity predictions, a search for the stronger symmetric stretch was attempted first to optimize gas mixture concentration before tackling the antisymmetric stretch.

Trial scans for the symmetric stretch quickly revealed strong progressions of jet-cooled CH_2F absorption lines centered around the 3045 cm^{-1} region, in close agreement with the DFT-scaled predictions above. After optimizing gas mixture and scanning conditions, continuous single mode spectra ranging from 3027 cm^{-1} to 3071 cm^{-1} were then pursued, yielding extensive R and P branches with a much weaker Q structure near the band origin. Sample data in the R-branch region are presented in Figure 2.3, illustrating a clear A-type band progression of K_a=0←0, 1←1, and 2←2 transitions spaced by B + C ≈ 1.96 cm^{-1}. Note the roughly 3:1 intensity ratio between the K_a=0 and K_a=1 lines; this ratio is consistent with ortho/para nuclear spin statistical predictions for the equivalent H atoms (i.e., $I_{H(eff)}$ = 0,1) and provides further confirmation of the ground state B_1 electronic symmetry of CH_2F. There is also a clear sequential shift to lower frequency for K_a=0←0, 1←1, and 2←2 transitions, which indicates a decrease in the A constant with vibrational excitation. At higher resolution, each line is split into fully resolved fine and partially resolved hyperfine structure components, as will be discussed later.

After extraction of a vibrational band origin estimate from the strongest transitions confirmed by approximate ground-state combination differences, the assignment proceeds rapidly by comparing experimental data with rigid asymmetric

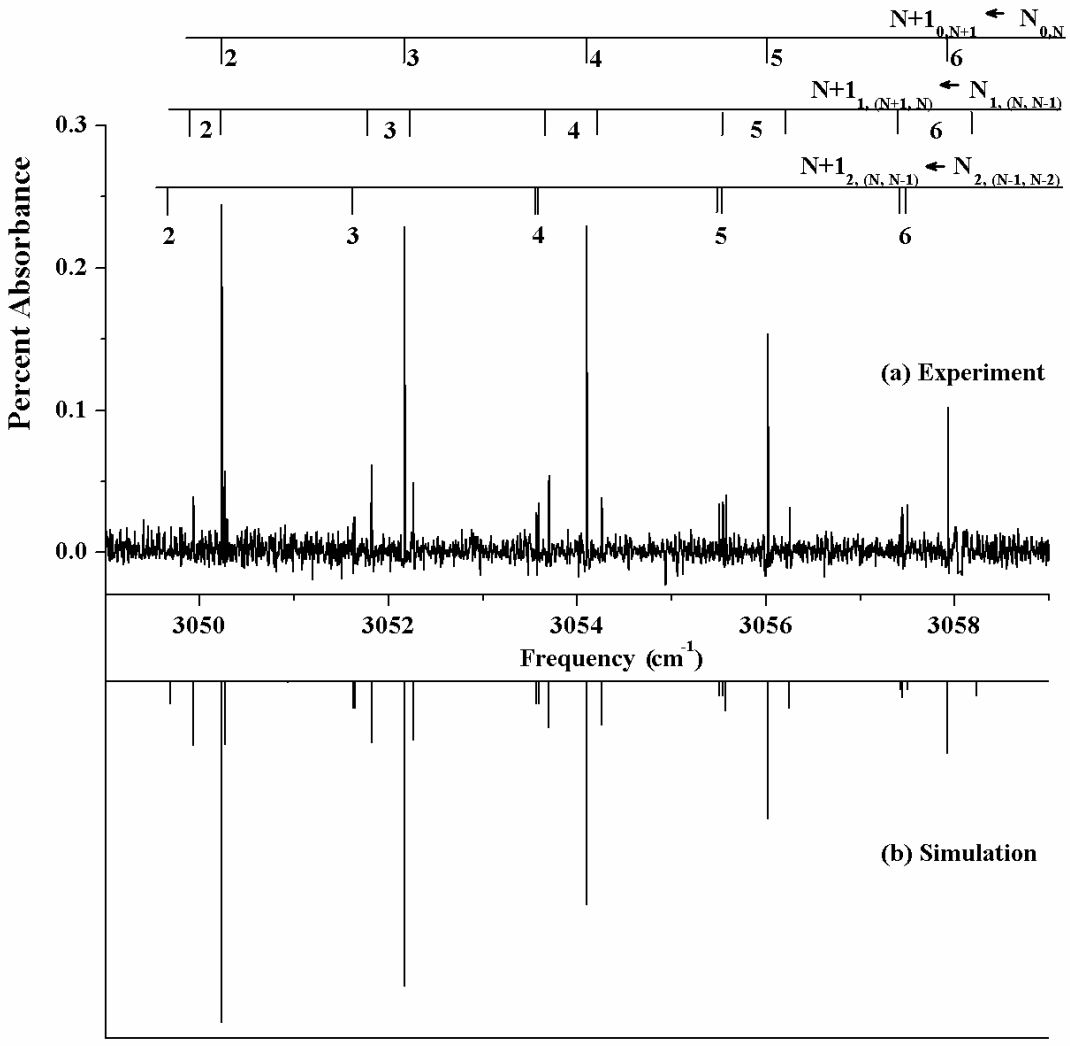

Figure 2.3 Sample CH_2F data in the CH_2 symmetric stretch region, comparing experimental (top) to simulated (bottom) spectra predicted from the least-squares fits.

top spectra predicted from the microwave constants. However, attempts to further confirm these assignments with more precise four-line (and ground state two-line) combination differences are complicated by the extensive fine and hyperfine structure superimposed on each $N_{Ka,Kc} \leftarrow N_{Ka,Kc}$ transition. This structure results in shifts/splittings up to a few GHz; i.e., greatly in excess of our experimental precision

(< 10 MHz) and yet quite small on the ≈1000 GHz scale of the infrared spectrum. We therefore developed a more sophisticated simulation program which includes the standard asymmetric top Hamiltonian, plus all fine (spin rotation) and hyperfine (Fermi contact, dipole-dipole and electric quadrupole) coupling terms utilized in the microwave analysis for a spin 1/2 electron and two nuclei (i.e. $I_{H(eff)}$ and I_F) with nonzero spin. This complete effective Hamiltonian is used for the final least-squares analysis of the line profiles, as will be discussed in more detail later in this section.

For the moment, however, we focus exclusively on the rovibrational information by predicting fine/hyperfine line intensities for a given $N_{Ka,Kc} \leftarrow N_{Ka,Kc}$ transition (estimated from Hirota's ground-state constants) and convoluted over a ≈ 60 MHz sub-Doppler linewidth in the slit jet. By simply shifting these predictions with respect to the high-resolution data, the pure asymmetric top (i.e., fine/hyperfine free) transition frequencies can be determined to an estimated precision of < 0.0001 cm^{-1}; i.e., less than our experimental uncertainty. In this fashion, 40 fine/hyperfine-free line centers (see Table 2.1) have been identified in the symmetric stretch, comprising transitions from states up to N=8 and 6 in the R and P branch, respectively. By way of initial analysis, these fine/hyperfine-free transition frequencies are least-squares fit to a Watson asymmetric top Hamiltonian for the ground and symmetric stretch-excited state.[41] However, the results reported in Table 2.3 reflect a more complete contour fit to both symmetric and antisymmetric stretch bands, as described below.

Table 2.1: Observed fine/hyperfine free line centers and (obs-calc) values from Watson asymmetric top Hamiltonian least-squares fit to the symmetric stretch (ν_1) band of CH_2F.

J'	K_a'	K_c'	*J"*	K_a"	K_c"	*Obs. (cm^{-1})*	*Obs. – calc. (10^{-4} cm^{-1})*
9	0	9	8	0	8	3061.71113	-1.4
8	0	8	7	0	7	3059.82793	3.4
8	1	8	7	1	7	3059.30971	-9.9
7	0	7	6	0	6	3057.93083	3.6
7	1	7	6	1	6	3057.44685	-4.8
6	1	5	5	1	4	3056.25346	0.2
6	0	6	5	0	5	3056.02127	1.2
6	1	6	5	1	5	3055.57726	-2.4
5	1	4	4	1	3	3054.26141	-1.3
5	0	5	4	0	4	3054.10114	2.2
5	1	5	4	1	4	3053.70186	-1.7
5	2	3	4	2	2	3053.59370	3.9
5	2	4	4	2	3	3053.56964	-0.1
4	1	3	3	1	2	3052.26520	-2.2
4	0	4	3	0	3	3052.17164	4.4
4	1	4	3	1	3	3051.82056	-2.6
4	2	2	3	2	1	3051.64177	-3.7
4	2	3	3	2	2	3051.63043	0.0
3	1	2	2	1	1	3050.26515	-4.0
3	0	3	2	0	2	3050.23363	2.7
3	1	3	2	1	2	3049.93449	0.8
2	0	2	1	0	1	3048.28887	1.1
2	1	1	1	1	0	3048.26293	5.9
2	1	2	1	1	1	3048.04361	4.7
1	0	1	0	0	0	3046.33860	-1.1
1	1	1	1	1	0	3044.13825	17.
2	1	2	2	1	1	3043.91543	8.9
0	0	0	1	0	1	3042.42706	-2.3
1	0	1	2	0	2	3040.46804	-2.5
1	1	0	2	1	1	3040.22320	-4.6
1	1	1	2	1	2	3040.43635	-7.6
2	1	2	3	1	3	3038.52536	-12.
2	0	2	3	0	3	3038.50852	-5.7
2	1	1	3	1	2	3038.20898	-7.5
3	1	3	4	1	4	3036.61337	-1.1
3	0	3	4	0	4	3036.54900	-1.9
4	1	4	5	1	5	3034.69938	16.
4	0	4	5	0	5	3034.59081	-2.
5	1	5	6	1	6	3032.78429	46.
5	0	5	6	0	6	3032.63456	-6.1

2.3.2 Antisymmetric CH_2 stretch line center assignments

The results from least-squares fits of the symmetric stretch line centers generate an improved rotational prediction for the B-type antisymmetric stretch band which, from DFT calculations, should have an origin near 3209 cm^{-1}. Single mode scans have therefore been performed from 3167 cm^{-1} to 3234 cm^{-1}, revealing a clear R, P branch progression but also a strong Q branch feature characteristic of a B-type vibrational transition (see Figure 2.4 for an enlarged view of partially resolved fine/hyperfine structure in the Q branch).

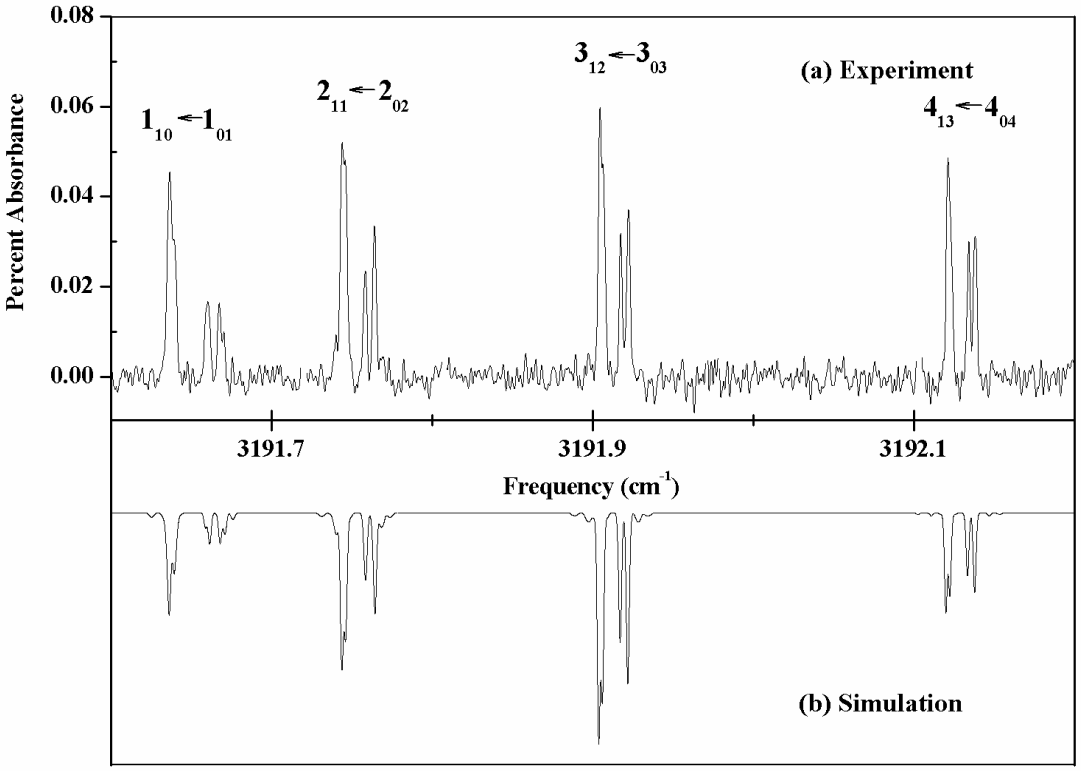

Figure 2.4 Sample Q branch CH_2F data for CH_2 antisymmetric stretch, comparing experimental (top) to simulated (bottom) spectra predicted from the least-squares fits and illustrating fully resolved fine structure.

Table 2.2 Observed fine/hyperfine free line centers and (obs-calc) values from Watson asymmetric top Hamiltonian least squares fit to the antisymmetric stretch (ν_5) band of CH_2F.

J'	K_a'	K_c'	*J"*	K_a"	K_c"	*Obs. (cm^{-1})*	*Obs. – calc. (10^{-4} cm^{-1})*
3	0	3	4	1	4	3168.68289	1.5
2	0	2	3	1	3	3170.43244	3.6
1	0	1	2	1	2	3172.23208	3.4
0	0	0	1	1	1	3174.08329	1.7
4	0	4	4	1	3	3175.42105	-1.7
3	0	3	3	1	2	3175.65076	-0.7
2	0	2	2	1	1	3175.82016	1.4
1	0	1	1	1	0	3175.93124	-2.3
5	1	5	6	0	6	3179.09192	2.1
3	0	3	2	1	2	3182.00361	-0.6
3	1	3	4	0	4	3183.44996	-0.5
4	0	4	3	1	3	3184.10389	-6.4
2	1	2	3	0	3	3185.56290	1.5
1	1	1	2	0	2	3187.62633	1.6
1	1	0	1	0	1	3191.64644	-2.9
2	1	1	2	0	2	3191.75168	-0.1
3	1	2	3	0	3	3191.9111	-0.3
5	1	4	5	0	5	3192.40397	0.6
6	1	5	6	0	6	3192.74437	1.0
1	1	1	0	0	0	3193.49639	-2.0
2	1	2	1	0	1	3195.34283	-1.0
4	1	4	3	0	3	3198.87162	-0.1
3	2	1	3	1	2	3206.60779	4.4
2	2	1	1	1	0	3210.78900	-3.2
2	2	0	1	1	1	3210.89776	2.5
3	2	2	2	1	1	3212.63329	2.8
3	2	1	2	1	2	3212.95985	-3.9

In contrast to the symmetric stretch, the antisymmetric stretch spectrum shows very little congestion due to precursor species. A similar procedure of 2-line combination differences with fine/hyperfine structure removed is then used for assigning and verifying the transitions, as described for the symmetric stretch band. In total, 27 transitions (see Table 2.2) are identified, with rotational levels sampling up

to N=6. Most notably, the peak antisymmetric stretch absorption strengths are found to be nearly two times *less* intense than those of the symmetric stretch, despite expectations of a threefold increase from bond dipole predictions discussed further in Section 2.4. As a result, transitions from both nuclear spin ground states (i.e. K_a=0 and 1) are readily identified (see Figure 2.4), but no transitions out of any thermally excited K_a states (K_a>1) are observed.

The analysis proceeds with both the symmetric and antisymmetric band line centers simultaneously least-squares fit with a common ground state, yielding a residual standard deviation of 15.6 MHz. This procedure allows further least-squares adjustment of rotational constants (see Table 2.3) and identification of symmetric and antisymmetric stretch band centers of 3044.3850(2) cm^{-1} and 3183.8560(2) cm^{-1}, respectively. Of particular importance to this study is that the additional inclusion of antisymmetric B-type stretch transitions (ΔK_a = +/-1, ΔK_c = +/-1) allows determination of all three rotational constants for both the ground state as well as both symmetric and antisymmetric vibrationally excited states. This is particularly relevant to a discussion of CH_2F radical vibrationally averaged versus equilibrium geometry, based on previous difficulties in least-squares fitting the ground state *A* rotational constant from microwave/near IR A-type bands. Unconstrained asymmetric rotor fits to the combined near IR data yield ground-state B, C and centrifugal distortion constants in agreement with the microwave studies to within experimental uncertainty. However, the combined fits now yield independent information on the ground state A constant, as well as rotational and partial centrifugal distortion constants for both symmetric and antisymmetric stretch excited manifolds. The

results are summarized in Table 2.3, where the quoted values reflect fits to the full line contours, as described below.

Table 2.3: Simultaneous least-squares fit results for CH_2 symmetric and antisymmetric stretch rotational constants (in cm^{-1}), with 1σ uncertainties in parentheses.

Constants (cm^{-1})	Ground state	Symmetric Stretch	Antisymmetric Stretch
A	8.8488(3)	8.78098(3)	8.7179(2)
B	1.03228(3)	1.03159(3)	1.03152(2)
C	0.92492(2)	0.92264(3)	0.92405(3)
Δ_N (10^{-5})	0.26[a]	0.27(2)	0.27(2
Δ_{NK} (10^{-5})	3.78[a]	5.0(8)	5.0(8)
Δ_K (10^{-5})	64.79[a]	78(6)	78(6)
ν_0		3044.3650(2)	3183.8560(2)

[a] Parameters previously determined by Hirota et al.

2.3.3 Fine and hyperfine structure and analysis

As is clear from the Q branch transitions in Figure 2.4, the experimental spectra show evidence of *fine* and *hyperfine* splittings resulting from different couplings of molecular rotation, electron spin, and nuclear spin angular momentum. To reproduce this structure and also to identify line centers for the least-squares fit described above, considerable effort was invested into developing a program to simulate and simultaneously least-squares fit actual line shapes of both the symmetric and antisymmetric bands. This program works for doublet asymmetric top radicals (S=1/2) with two different nonzero nuclear spin atoms [$I_F = 1/2$ and $I_H = 0$(para) and

1(ortho)], as well as includes spin rotation, Fermi contact, and dipole-dipole and electric quadrupole interactions. Exhaustive benchmark tests have been performed, including numerical comparisons with similar program code developed by the Brown group at Oxford, achieving agreement out to machine precision. For further program development in other laboratories, sample eigenvalue output for a given set of effective Hamiltonian parameters will be made available upon request.

Following the microwave analysis of Hirota, the effective Hamiltonian used for simulation and fitting of the current near IR fine and hyperfine structure is given by

$$H = H_{ROT} + H_{SR} + H_F + H_{DD} + H_{eQ}, \qquad (2.1)$$

where H_{ROT} is the traditional Watson Hamiltonian for an asymmetric rotor and H_{SR}, H_F, H_{DD}, and H_{eQ} represent the fine (electron spin) and hyperfine (nuclear spin) coupling terms. The largest splittings in the CH_2F rovibrational spectra are dominated by rotational coupling between electron *spin* ***S*** and asymmetric top molecular *rotation* ***N***. The spin rotation fine structure coupling interaction, H_{SR}, is expressed as $H_{SR} = (1/2)\sum_{\alpha,\beta} \varepsilon_{\alpha\beta}(N_\alpha S_\beta + S_\beta N_\alpha)$, where $\varepsilon_{\alpha\beta}$ is the spin rotation tensor and α, β are labels for the a, b, c principal axes. For a species of orthorhombic symmetry (such as CH_2F), only the diagonal matrix elements (ε_{aa}, $\varepsilon_{bb,}$, $\varepsilon_{cc,}$) are nonzero and need to be considered. The dominant hyperfine terms are the isotropic Fermi contact interaction, $H_F = a_F I \cdot S$, the dipole-dipole interaction, $H_{DD} = S \cdot T_{dd} \cdot I$, and the nuclear electric quadrupole interaction, $H_{eQ} = S \cdot T_{eQ} \cdot I$, where T_{dd} and T_{eQ} each denote a second-rank traceless tensor with five independent components.

The total Hamiltonian is expanded in a Hund's case(b)$_{\beta J}$ basis set, $|N,K,S,J,I_1,F_1,I_2,F,M_F\rangle$, where the angular momenta are coupled via $\mathbf{J = N + S}$, $\mathbf{F_1 = J + I_1}$, $\mathbf{F = F_1 + I_2}$. I_1 and I_2 represent the F and H atom nuclear spins, respectively, where I_2=0 (or 1) for para (or ortho) coupling of the two identical H atoms. The explicit matrix element expressions are obtained from Hirota,[42] exploiting the extended expressions for hyperfine interactions caused by more than one nucleus. The Hamiltonian matrices for a given upper and lower N_{KaKc} state are diagonalized to generate eigenvalues, with care taken to ensure the basis set includes all possible F values to completely converge the fine and hyperfine patterns. Electric dipole transition strengths between all allowed transitions (ΔF = 0, +/-1) are then calculated from eigenvector sums over Stark matrix elements, convolved over a Doppler width (assumed constant for all transitions), and compared with experimentally observed line profiles via a least-squares fitting routine.

By way of example, sample fine and hyperfine data for the $2_{11} \leftarrow 2_{02}$ transition (I_H=1, ortho) in the asymmetric stretch band of CH_2F are shown sequentially in Figure 2.5. The top panel (a) illustrates the single ≈ 60 MHz Doppler line profile anticipated in the absence of any electron or nuclear spin interactions, with the results in panels below illustrating the additional splittings and broadenings that result from successive inclusion of fine structure (b) and hyperfine structure (c). Finally, the observed experimental line profile for this transition is given in panel (d), which is in good agreement with the least-squares fitted fine/hyperfine predictions. It is particularly noteworthy that both fine and hyperfine structure contribute to well-resolvable peaks in the predicted spectrum, although much of the structure is below

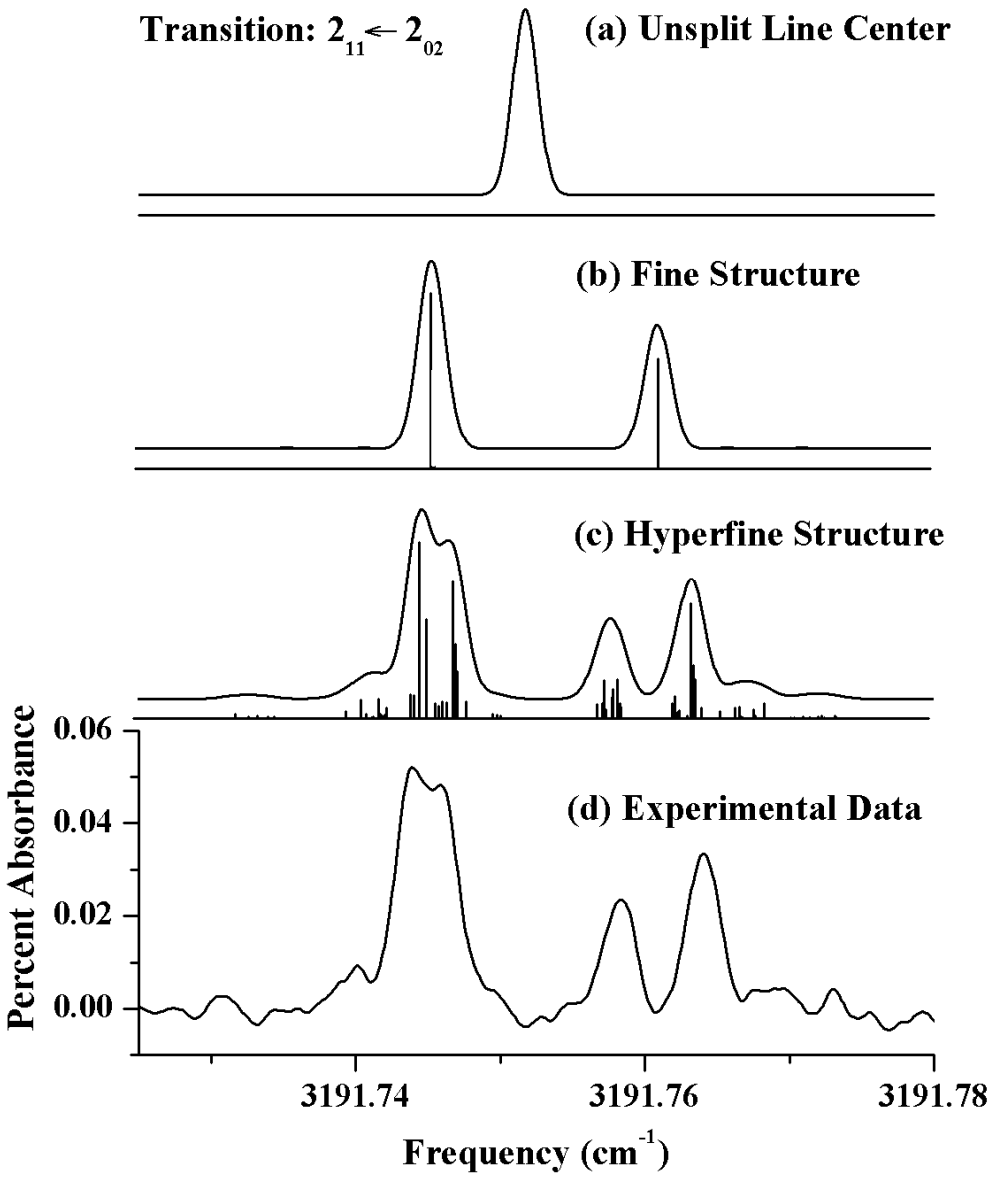

Figure 2.5 Sample data and contour predictions for the $2_{11} \leftarrow 2_{02}$ transition, systematically including fine and hyperfine terms in the Hamiltonian. a) Asymmetric top only. b) Asymmetric top plus spin rotation. c) Asymmetric top, spin rotation and hyperfine terms. d) Experimental data.

the sub-Doppler resolution limit. Analysis of fine/hyperfine information is more typically confined to studies in the millimeter or microwave regime; experimental access to this information in the near infrared is the result of sub-Doppler resolution due to transverse velocity collimation in the slit jet expansion. To minimize number of parameters in the least-squares fits, the ground state is fixed at previously determined restrict the fit to the spin-rotation constants (ε_{aa}, ε_{bb}, ε_{cc}) in the excited symmetric and antisymmetric stretch states, keeping the rotational, fine and hyperfine parameters fixed at ground state values.[31] A summary of the fitted fine structure results is summarized in Table 2.4, which indicates modest but statistically significant changes in all three spin rotation constants upon vibrational excitation.

Table 2.4: Least-squares results for spin rotation fine-structure constants obtained from simultaneous fit to symmetric and antisymmetric CH_2 stretch line contours, with 1σ uncertainties in parentheses. Ground state fine/hyperfine constants, as well as excited-state hyperfine constants are held fixed at values from microwave studies.{Endo, 1983}

Constants (cm^{-1})	Ground state	Symmetric Stretch	Antisymmetric Stretch
ε_{aa} (10^{-4})	-358.902[a]	-346(2)	-352(1)
ε_{bb} (10^{-4})	-61.966 [a]	-60.0(3)	-61.4(3)
ε_{cc} (10^{-4})	-0.471 [a]	-1.7(3)	-0.6(3)

[a] Parameters previously determined by Hirota et al.

2.4 Discussion

One of the key unresolved issues about CH_2F concerns its equilibrium geometric structure, which fundamentally reflects the competition between sp^2 versus

sp^3 hybridization of the central carbon atom as a function of electrophilic substitution. Theory predicts CH_2F to have a bent equilibrium structure with a shallow barrier to interconversion, suggesting a quasiplanar geometry with extensive large amplitude quantum sampling of nonplanar structures.[26] Previous microwave studies yielded rotational constants consistent with a near planar structure but could not rule out the presence of large amplitude vibrational sampling over this inversion coordinate.[31,32] Furthermore, these studies revealed no indication of tunneling structure, confirming any barrier at planarity to be smaller than the zero point energy in the inversion coordinate. More quantitatively, microwave satellite peaks due to transitions out of a thermally accessible state were ascribed to v_4=1 of the inversion mode, with a temperature dependence that suggested a bend vibrational frequency of 300(30) cm^{-1}.[31] This is two-fold smaller than the 600 cm^{-1} bend frequency experimentally measured for methyl radical,[43] despite simple harmonic expectations from a Wilson G matrix analysis of only a ≈ 3.4 % decrease due to a ≈ 6.9% increase in bending moment of inertia upon fluorination. At the very least, this suggests an even more highly nonharmonic bending potential than observed in methyl radical, with the likelihood of an appreciable barrier to planarity.

2.4.1 Boltzmann intensity analysis

The current high-resolution IR data for CH_2F provides several important clues to the issue of equilibrium structure, the first of which is the anomalous intensity ratio for the symmetric and antisymmetric CH_2 stretches. Boltzmann analysis of the line intensities yields both a rotational temperature for the radicals as well as the relative

intensities of the two bands. The experimental integrated line absorbances for a given rovibrational transition ($j \leftarrow i$) are given by

$$S_{\exp} = \int A(v)dv = N^i \cdot l \cdot S_0^{ji}, \tag{2.2}$$

where l is the absorption length (64 cm) and S_0^{ji} is the line strength per M_J state. The number density of molecules in the lower state, N^i, can be expressed as

$$N^i = N_0^{vib} \cdot \frac{g_{NS} \cdot g_J}{Q_{ROT}^{NS}} \cdot e^{-(E_i - E_0^{NS})/kT_{ROT}}, \tag{2.3}$$

where N_0^{vib} is the population in the specific vibrational state *vib*, g_{NS} is the nuclear spin weight, g_J is the rotational degeneracy, E_0^{NS} is the lowest energy level within the same nuclear spin symmetry, and Q_{ROT}^{NS} is the rotational partition function of a particular nuclear spin symmetry.

Data for both symmetric and antisymmetric band transitions for ΔJ=1 and ground-state K_a=0 are shown in Figure 2.6. The integrated line absorbances, S_{exp}, are scaled by calculated line strengths and nuclear spin weights and are plotted semilogarithmically against the ground-state rotational energy. Least-squares fits of these data to a single slope yield a common rotational temperature of 20.8(8) K. More relevant to the present discussion, these data also permit the relative symmetric stretch and antisymmetric stretch band intensities to be estimated by band strength integration for the two stretch manifolds, which for a single rotational temperature is determined by the difference in the Boltzmann plot intercepts. This procedure yields an intensity ratio of 1.8(2) between the symmetric and antisymmetric CH_2 stretches, respectively. This is substantially *larger* than would be expected from a simple bond-

dipole model for localized symmetric and antisymmetric stretch motion in an isolated HCH group, which for a 120° HCH bond angle would predict a sixfold smaller ratio of 1:3.

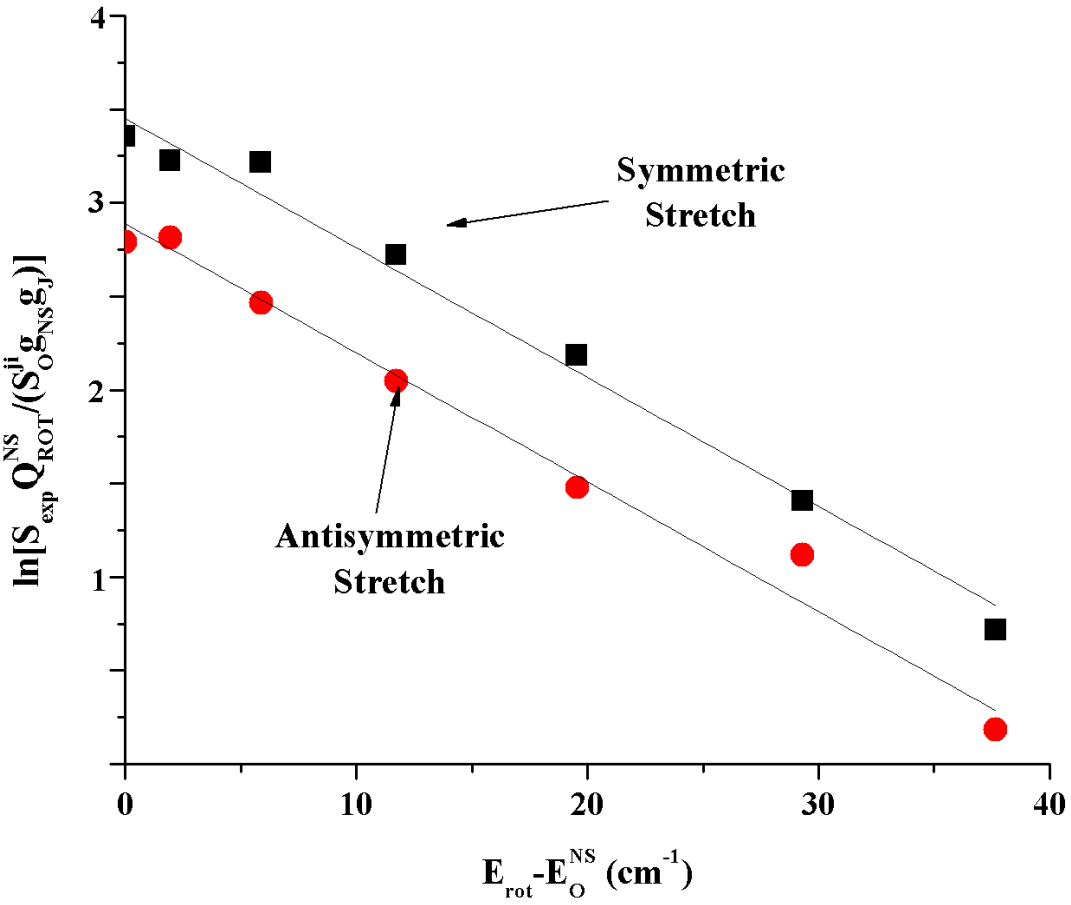

Figure 2.6 Boltzmann plot for ground state rotational populations monitored in symmetric and antisymmetric CH_2 stretch modes, verifying jet-cooled conditions [T_{rot} = 20.8(8) K] in the slit discharge and demonstrating a 1.8(2):1 ratio between the two bands.

To further explore this anomaly, we have pursued moderately high-level theoretical calculations utilizing density functional theory (B3LYP) with an aug-cc-pVTZ basis, first optimizing the geometry and then calculating vibrational

frequencies and intensities using a Gaussian 03 software package.[44] The DFT results confirm the observed behavior with a predicted ratio of $I_{sym}/I_{asym} \approx 2.1$; i.e., in essentially quantitative agreement with the experimental value of 1.8(2). Interestingly, however, the predicted infrared intensities for both bands (11.9 km/mol and 5.60 km/mol for symmetric and antisymmetric stretches, respectively) are both significantly larger than what would be expected for a simple bond dipole model of the CH_2 group. This prediction can be explicitly tested by performing similar DFT (B3LYP-aug-cc-PVTZ) frequency calculations for CH_2D radical, whereby mono-deutero substitution breaks the local mode degeneracy in CH_3, thereby localizing the CH_2 vibrations into symmetric and antisymmetric motions. The CH_2D results indicate symmetric and antisymmetric stretch intensities of 1.61 km/mol and 3.84 km/mol; i.e., both much lower than predicted for CH_2F and indeed more nearly consistent with a simple bond dipole CH intensity ratio of $I_{sym}/I_{asym} \approx 1:3$. This behavior indicates that fluorine substitution leads to a breakdown of the bond dipole model in describing CH stretch intensities in CH_2X radical.

Close inspection of the *ab initio* results reveals that this breakdown arises from larger (and in fact *opposing*) dipole derivatives due to *flow of atomic charge* densities under normal mode CH_2 stretch displacements. Based on a simple Mullikan charge description, the calculations (figuratively shown in Figure 2.7) indicate significant *decrease* ($-\delta q_H$) in H atom positive charge densities upon symmetric extension of the C-H bond. This decrease is accompanied by a corresponding *increase* ($+\delta q_C$ and $+\delta q_F$) in both carbon and fluorine charge densities (i.e., to *less negative* values). This "charge-sloshing" results in net flow of positive charge *away*

from the C-H bond displacement, yielding transition dipole moment contributions in the *opposite* direction from bond-dipole expectations. Indeed, detailed estimates for the CH_2 symmetric stretch in CH_2F shows that the magnitude of this "charge-sloshing" moment to be *in excess* of the conventional bond-dipole contribution, thus actually *reversing* the direction of the overall transition dipole.

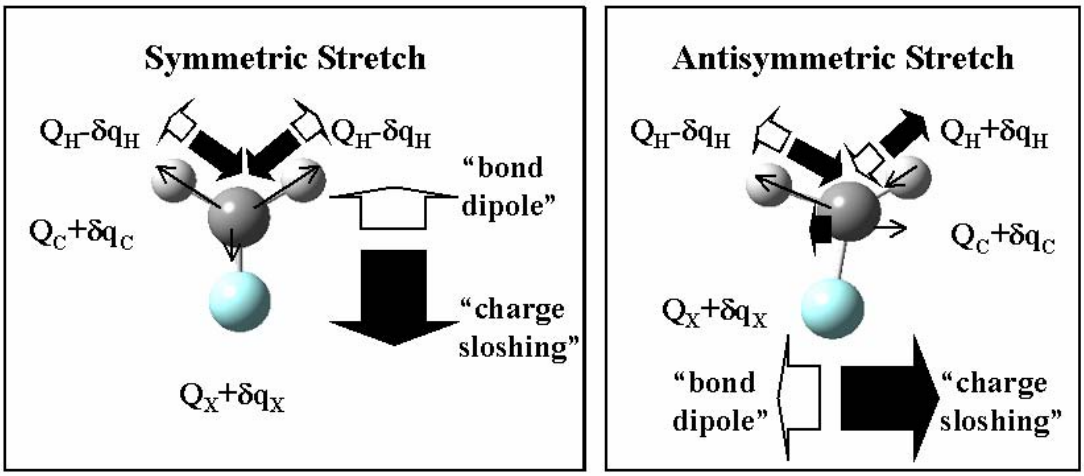

Figure 2.7 Cartoon illustrating the competition between "bond dipole" and "charge sloshing" contributions to symmetric and antisymmetric CH stretch intensities in CH_2F.

Similarly for the antisymmetric CH_2 stretch, the hydrogen atom charge densities *decrease* ($-\delta q_H$) and *increase* ($+\delta q_H$) upon extension and compression of the C-H bonds, respectively (see Figure 2.7). Both carbon and fluorine atom charge densities *increase* ($+\delta q_C$ and $+\delta q_F$) with antisymmetric CH extension, though the magnitudes of δq_C and δq_F are far smaller since the H atom charge redistributions are of opposing sign. Once again, the "charge-sloshing" component of the transition moment more than cancels that of the bond-dipole contribution and indeed *reverses* the sign of the overall transition dipole. Interestingly, since the net CH stretch

transition moment reflects a competition between these two contributions, one might anticipate a strong dependence of these vibrational band strengths on the nature of the halogen substitution. This picture is supported by parallel high-resolution IR studies of CH_2Cl, for which the antisymmetric CH_2 stretch band intensity is experimentally found to be more than 20-fold weaker than symmetric stretch excitation, as will be discussed elsewhere.[45] Stated simply, CH stretch vibrational intensity in these halomethyl radicals is influenced not only by motion of localized charges on the atoms, but in fact by charge flow throughout the entire molecule. Such dramatic failure of a bond dipole analysis clearly highlights the significant (and even predominant) contribution that a nominally "spectator" carbon-halogen bond can make to IR intensities in the CH stretch region of the spectrum. There appears to be steadily growing evidence for such "charge sloshing" intensity effects in other open shell and ionic systems as well. One system is cis-perp HOONO from the Lester group, for which the a-type overtone OH stretch dipole moment is dominated by charge flow along the OONO framework and is therefore nearly perpendicular to the ≈ c-type OH stretching motion. A second example is that of $Cl^-(H_2O)$, for which the *overtone* of the HOH bending mode is much stronger than the fundamental due to a vibrationally induced modulated polarization of the Cl^- anion along the a-axis.

2.4.2 Complete Basis Set (CBS) inversion potential for CH_2F

The DFT (B3LYP/aug-cc-pVTZ) calculations described above for CH_2F suggest (i) a significantly nonplanar equilibrium geometry ($\theta \approx$ 25-30 degrees) as well as (ii) a strong intensity dependence for both modes on the displacement from

planarity. This provides sufficient motivation to pursue a higher *ab initio* treatment of the inversion-bending potential at the CCSD(T) level, exploiting highly efficient quantum chemistry routines available from MOLPRO.[46] To eliminate residual errors resulting from finite basis set size, the optimized geometry and frequency calculations have also been performed for a series of Dunning basis sets (AVnZ) and extrapolated to the CBS limit.[47] Specifically, geometries for CH_2F are optimized at the CCSD(T) level as a function of the bending inversion angle θ (defined as the complement of the CF angle with respect to the bisector of the CH_2 plane) for an AVnZ basis set with n = 2, 3, and 4. Following the work of Peterson,[47] these angle-dependent energies as a function of n are extrapolated to the CBS limit by fitting to

$$E(n) = E_{CBS} + Be^{-(n-1)} + Ce^{-(n-1)^2} \qquad (2.3)$$

and solving for E_{CBS}. The level of convergence with respect to basis set size is quite good, with the final E_{AVQZ}-E_{CBS} energy shifts reduced by more than five-fold from the corresponding E_{AVDZ}-E_{AVTZ} differences.

To account for relatively minor vibrational energy corrections to the inversion potential due to adiabatic zero point excitation in the remaining 3N-7=5 vibrational coordinates, CCSD(T) frequency predictions have also been performed. In the current version of MOLPRO, these more computationally demanding calculations require numerical Hessians and therefore have only been performed at each inversion angle for the AVDZ basis set. However, single point frequency calculations for planar and equilibrium geometries have been obtained at the AVTZ and AVQZ level, which indicate a better than 99% level of convergence in zero point energies. The resulting sum of zero-point energy (ZPE) over all high frequency vibrations is found to be

nearly constant as a function of bend angle, and thus has a relatively minor qualitative impact on the potential curve topology.

The resulting CBS inversion-bending potential for CH_2F is shown in Figure 2.8 and indicates a clearly *bent* equilibrium geometry of $\theta \approx 29^\circ$ with a transition-state barrier ($E_{barrier} \approx 132$ cm^{-1}) to inversion at planarity. This equilibrium bend angle is essentially identical for the CBS potential ($\theta \approx 25^\circ$), though ZPE correction deepens the well by an additional ≈46 cm^{-1} (from 86 cm^{-1}) primarily because of a slight stiffening of the CH and CF stretching modes near the planar configuration.

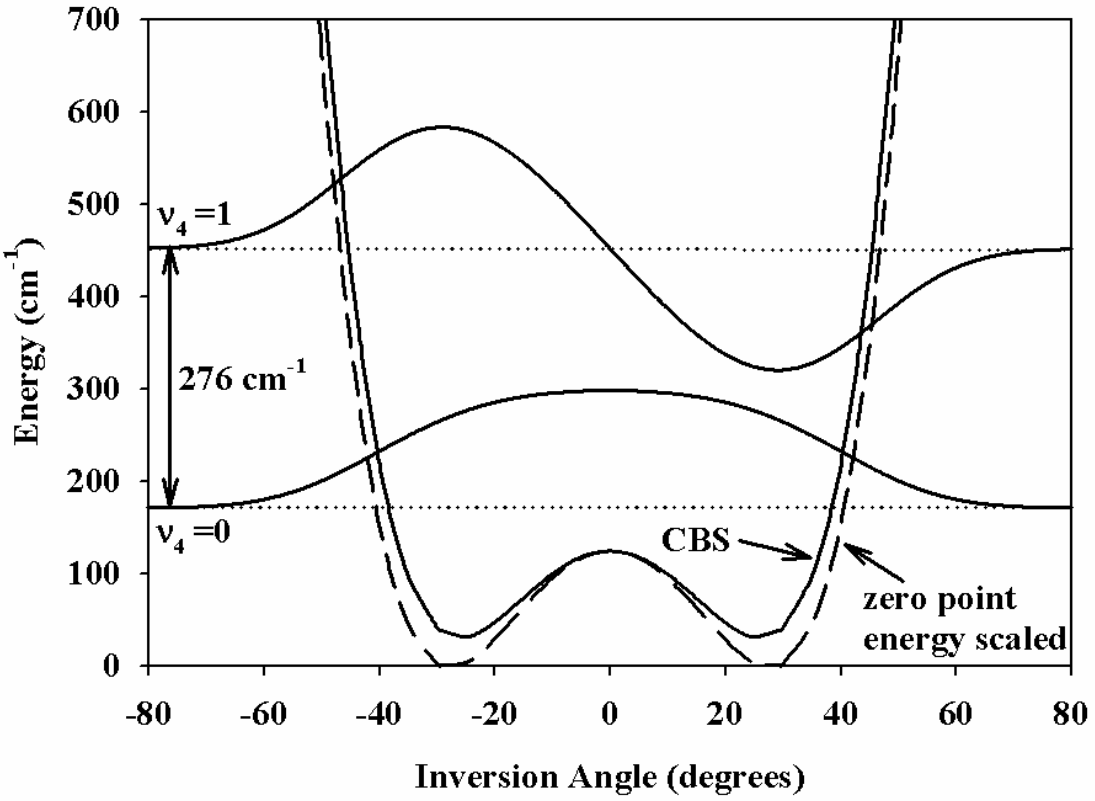

Figure 2.8 One-dimensional potential energy curve (solid line) obtained from CCSD(T) complete basis set (CBS) calculations (see text for details), with zero-point energies in all remaining coordinates included adiabatically (dashed line). Ground and excited state eigenvalues (dotted line) and eigenfunctions (solid line) from a multidimensional Rush-Wiberg analysis are also indicated, which predict the ν_4=1←0 anharmonic bending frequency to be 276 cm^{-1}.

This is also consistent with a geometry-dependent partial sp^3 hybridization for the central C atom, which becomes purely sp^2 (and therefore stiffer) at planarity. It is worth noting that the ZPE uncorrected predictions of $E_{barrier} \approx 86$ cm^{-1} and $\theta \approx 25^\circ$ are in reasonable agreement with earlier studies by Krylov and co-workers, who obtained $E_{barrier} \approx 109.9$ cm^{-1} and $\theta \approx 27^\circ$ using CCSD(T) methods but without extrapolation to the CBS limit.[26]

The spectroscopic impact of this 132 cm^{-1} barrier depends largely on its relative position with respect to the ground-state energy. Vibrational eigenstates and eigenenergies have therefore been obtained for this potential, exploiting the polyatomic 1D Schroedinger equation methods outlined by Rush and Wiberg.[48] These methods explicitly include coordinate-dependent changes in both the moments of inertia [$\mu(\theta)$] and the vibration-rotation G matrix of Laane [$\mathbf{G}(\theta)$] which, for large amplitude bending motion in CH_2F, can represent a significant contribution. Quickly summarized, the inverse $\mathbf{G}^{-1}(\theta)$ matrix is obtained at each bend angle coordinate by differentiation and numerically inverted to yield $\mu(\theta)$ and the determinant $|\mathbf{G}(\theta)|$. The relevant 1D Schroedinger equation for large amplitude polyatomic motion is obtained from the rigid bender studies of Hougen, Bunker, and Johns,[49] which yield a Hamiltonian for J=0 expressed as

$$\partial^2/\partial\,\theta^2\ \phi(\theta) = \{f(\theta) + 2\mu(\theta)/\mathrm{hbar}^2[V(\theta)-E]\}\phi(\theta), \qquad (2.4)$$

where the 1D vibrational wavefunction is

$$\Psi(\theta) = \mu(\theta)^{1/2}\ \phi(\theta), \qquad (2.5)$$

and

$$f(\theta) = |\mathbf{G}(\theta)|^{1/4}\ \mu(\theta)^{1/2}\{\partial^2/\partial\,\theta^2[|\mathbf{G}(\theta)|^{-1/4}\ \mu(\theta)^{-1/2}]\}, \qquad (2.6)$$

The angle-dependent quantities $V(\theta)$, $\mu(\theta)$ and $|\mathbf{G}(\theta)|^{-1/4}\,\mu(\theta)^{-1/2}$ are each fit to a high (n=12) order polynomial in θ, which then allows the energy eigenvalues and 1D eigenfunctions to be obtained via standard Numerov-Cooley methods. The resulting ground (E_0 = 174 cm^{-1}) and first excited state (E_1 = 450 cm^{-1}) energies and vibrational wave functions for CH_2F, calculated for the zero-point-corrected potential energy curve, are displayed in Figure 2.8. The ground-state energy lies substantially *above* the barrier to planarity, but the effect of such a highly nonharmonic well on the wave function is clearly evident. The $1\leftarrow0$ vibrational spacing can therefore be predicted to be $E_{1\leftarrow0}$ = 276 cm^{-1}, which is in good agreement with both previous experimental estimates of both Hudgens *et al.* (260 ± 30 cm^{-1}) and Endo *et al.* (300 ± 30 cm^{-1}). In the interest of facilitating direct spectroscopic observation of this inversion mode, we have also calculated higher vibrational states on this surface to be E_2 = 948 cm^{-1}, E_3 = 1510 cm^{-1}, and E_4 = 2134 cm^{-1}, yielding frequency differences of $E_{2\leftarrow1}$ = 498 cm^{-1}, $E_{3\leftarrow2}$ = 562 cm^{-1}, and $E_{4\leftarrow3}$ = 624 cm^{-1}. Note the strong *blue shifting* (i.e., negative anharmonicity) of this vibrational progression, characteristic of a more square well potential with a "flattened" or even "inverted" bottom due to a barrier at planarity.

2.4.3 Intensity-based evidence for a nonplanar equilibrium geometry

The traditional high resolution source of evidence for a planar versus nonplanar equilibrium structure comes from analysis of the rotational constants, which for a rigid planar geometry should yield a vanishing inertial defect ($\Delta = I_c - I_b - I_a$).[50] In the presence of large out-of-plane amplitude motion, this inertial defect averages in nonplanar contributions which make $\Delta < 0$,[50] though for CH_2F this

naturally occurs in competition with large amplitude *in-plane* vibrational motion, which tends to make $\Delta > 0$. Experimentally, the inertial defect derived from the rotational constants is negative (Δ = -0.0096 amu A^2) but, in fact, considerably smaller than predicted for a rigid structure at the equilibrium geometry (Δ = -0.174 amu A^2). This experimental result would be more consistent with the CH_2F radical sampling both wells of the potential function, resulting in a nearly zero inertial defect, but still bent on average. A more dramatic piece of structural evidence arises from a closer investigation of the anomalous ratio for the symmetric and antisymmetric CH_2 stretch band intensities. In particular, both the symmetric and antisymmetric stretch intensities depend on the inversion bend angle, but with the antisymmetric stretch intensity increasing considerably more rapidly with deviation from planarity. This can be explicitly reproduced by density functional theory (B3LYP) calculations in an aug-cc-pVTZ basis set for CH_2F frequencies and intensities, in which we freeze the inversion bend angle and optimize it with respect to all other coordinates. At the *planar* C_{2v} configuration, the symmetric and antisymmetric CH_2 stretch intensities are 9.1 and 2.1 km/mol, respectively, which translate into a ratio of $\approx$ 4.3:1; i.e., considerably larger than the experimentally observed value of 1.8(2). At the theoretically predicted equilibrium geometry of $\theta \approx 29^\circ$, however, these intensities increase to 11.8 and 5.5 km/mol, yielding a $\approx$ 2.1 ratio, now in much better agreement with experiment. This strong dependence of the intensity ratio can therefore in principle be utilized as an novel, albeit indirect, probe of the effective nonplanarity of CH_2F.

A plot of the symmetric to antisymmetric stretch intensity ratio, calculated at the B3LYP/aug-cc-pVTZ level, is shown in Figure 2.9 as a function of the inversion bend angle for CH_2F radical. This ratio varies by nearly 250% over the range of planar to equilibrium geometries. For comparison, results for CH_2D are also provided, which demonstrate the more "typical" intensity ratio of ≈ 0.4 with essentially negligible dependence on bending angle. Also indicated in the plot is the experimentally observed intensity ratio and its implication in this simple model for an effective non-planar bend angle ($\theta \approx 29^\circ$). The consistency between the experimental intensity ratio and the theoretically predicted equilibrium geometry is noteworthy, though clearly from the large amplitude 1D wave-bending functions shown in Figure 2.8, the experimental data quantum mechanically samples over a continuum of geometries between $\theta \approx \pm 50^\circ$. This large amplitude motion can be taken into account by averaging the *ab initio* values of I_{sym} and I_{asym} over the quantum probability as a function of the bend angle, $|\Psi(\theta)|^2$. This 1-D integration yields $\langle I_{sym} \rangle \approx 11.5$ km/mol, $\langle I_{asym} \rangle \approx 5.7$ km/mol, and a predicted intensity ratio of $I_{sym}/ I_{asym} \approx 2.0$. Given the simplicity of this model, this is in remarkably good agreement with the experimental result of $I_{sym}/ I_{asym} = 1.8(2)$ and provides independent support for the *ab initio* inversion potential in Fig 8. Of equal importance, the juxtaposition of this agreement with a nearly 2-fold discrepancy from planar intensity predictions provides strong and rather novel confirmation of a *nonplanar* CH_2F equilibrium geometry, based purely on infrared CH stretch intensities.

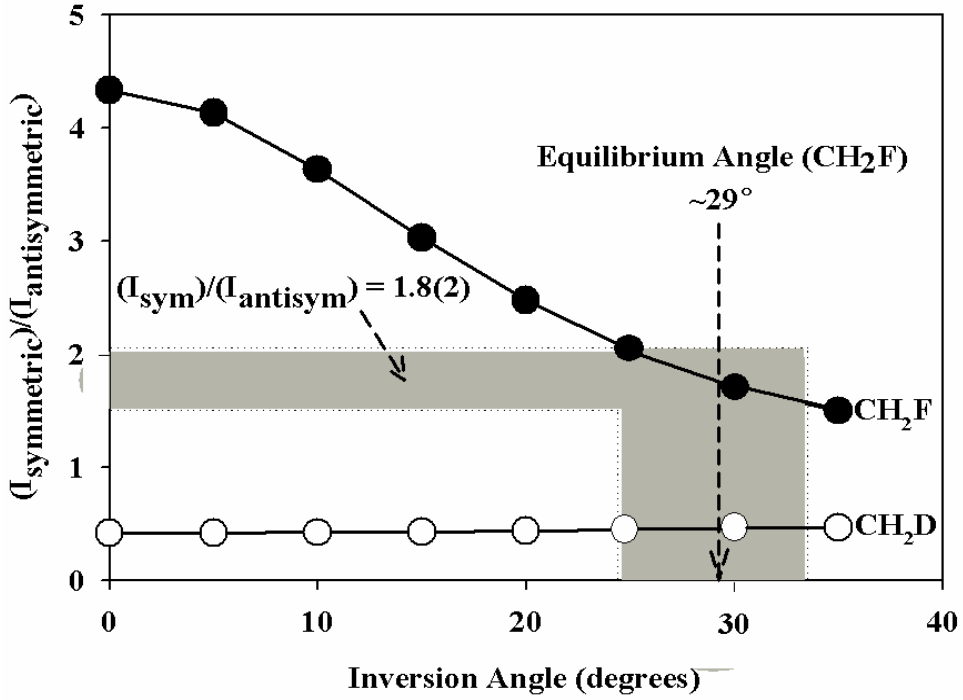

Figure 2.9 Calculated intensity ratios for symmetric and antisymmetric CH_2 stretches in CH_2F, highlighting a remarkably strong dependence on inversion angle. Note the essentially constant ratio predicted for CH_2D. Though large amplitude averaging is clearly important, the experimental intensity ratio of 1.8(2):1 for CH_2F is qualitatively consistent with the potential surface equilibrium angle of $\theta = 29^o$.

2.5 Summary and Conclusion

First high-resolution infrared spectra for jet-cooled CH_2F radicals have been obtained for the symmetric and antisymmetric CH_2 stretching modes. Subsequent spectral assignment has enabled the determination of refined lower- and upper-state rotational constants and fine-structure parameters from least-squares fits to the sub-Doppler line shapes for individual transitions. Band centers have been assigned for the symmetric and antisymmetric stretches at 3044.3850(2) cm^{-1} and 3183.8560(2) cm^{-1}, respectively. The symmetric stretch shows characteristically strong R and P branches with a weaker Q branch, along with a clear A-type band progression of K_a=

0←0, 1←1, and 2←2 transitions spaced by B + C = 1.96 cm^{-1}. In contrast, the antisymmetric stretch shows a strong Q branch characteristic of a B-type transition and with fully resolved fine and largely unresolved hyperfine structure.

Analysis of these data lends insight into the question of the CH_2F equilibrium geometric structure. These rotational constants, as well as experimental and theoretical findings by previous researchers, indicate the possibility of large amplitude vibrational averaging over a low-barrier double minimum inversion-bending potential, reflecting the competition between sp^2 and sp^3 hybridization of the center carbon atom as a function of electrophilic substitution. High-level CCSD(T) calculations extrapolated to the CBS limit confirm the existence of a nonplanar (θ = 29°) equilibrium structure, predicting a 120 cm^{-1} barrier to planarity and a vibrational bend frequency of 276 cm^{-1}. This bend frequency prediction is in excellent agreement with previous microwave studies of thermally excited hot bands by Hirota *et al.* (300(30) cm^{-1}) as well as REMPI measurements by Hudgens *et al*. (260(30) cm^{-1}). The ground state energy lies *above* the barrier to planarity, for which the delocalizing effect of such a highly nonharmonic well on the wave function is clearly evident. Higher vibrational energy levels (E_2, E_3, and E_4) have been predicted to help stimulate further experimental confirmation of this bend potential.

Particularly noteworthy is the ≈ 1.8(2):1 experimentally observed ratio of symmetric to antisymmetric CH_2 stretch intensities for CH_2F radical. This is much larger than simple geometric bond dipole predictions (≈ 1:3) and yet is much smaller than *ab initio* calculations for a *planar* configuration (≈ 4.3:1) Indeed, such *ab initio* calculations predict a surprisingly strong dependence of this intensity ratio on

bending angle, which has been exploited as a indirect source of evidence for a nonplanar equilibrium CH_2F geometry. Furthermore, analysis of these intensity calculations suggest the CH_2 symmetric and antisymmetric stretch band strengths to be dominated by vibrationally induced "charge sloshing" between the H, C and F atoms rather than the traditional "bond dipole" displacement of the charge centers. Indeed, these charge flow effects are sufficiently strong in halomethyl radicals to *reverse* the sign of the dipole transition moment from simple bond dipole predictions for both symmetric and asymmetric CH stretch modes. This novel *opposition* of intensity contributions, in conjunction with the strong dependence of atomic charges on electronegativity of the substituent, suggests interesting anomalies, such as near perfect cancellation of IR intensities for symmetric or antisymmetric modes, may be anticipated in other halomethyl radical systems. By way of support, high resolution IR laser spectra of chloromethyl radical reveal a > 30:1 ratio of symmetric to antisymmetric CH stretch band intensities. However, additional experimental and theoretical work will clearly be required to test this model further.

Acknowledgement

This work has been supported by funds from the National Science Foundation and the Air Force Office of Scientific Research. We would like to thank Prof. John Brown (Oxford) for his gracious help in benchmarking computer programs developed in each of our groups for doublet electron spin states in asymmetric tops with two non-zero nuclear spins.

References for Chapter 2

[1] M. E. Jacox, J. Phys. Chem. Ref. Data **32**, 1 (2003).

[2] S. Davis, Ph.D. Thesis, University of Colorado (1999).

[3] E. Hirota, Chem. Rev. **92**, 141 (1992).

[4] R. G. W. Norrish and G. Porter, Nature **164**, 658 (1949).

[5] G. Herzberg, *Molecular Spectra and Molecular Structure III. Electronic Spectra and Electronic Structure of Polyatomic Molecules*. (Van Nostrand, New York, 1966).

[6] A. M. Bass and H. P. Broida, *Formation and Trapping of Free Radicals*. (Academic Press, New York, 1960).

[7] B. C. Gilbert, M. J. Davies, and D. M. Murphy, *Electronic Paramagnetic Resonance*. (Royal Society of Chemistry, Cambridge, UK, 2002).

[8] J. S. Wells and K. M. Evenson, Rev. Sci. Instr. **41**, 226 (1970).

[9] K. M. Evenson, H. P. Broida, J. S. Wells, R. J. Mahler, and M. Mizushima, Phys. Rev. Lett. **21**, 1038 (1968).

[10] E. F. C. Byrd, D. Sherrill, and M. Head-Gordon, J. Phys. Chem. A **105**, 9736 (2001).

[11] J. S. Francisco and M. M. Maricq, in *Advances in Photochemistry* (Wiley, New York, 1995), Vol. 20, pp. 79.

[12] B. J. Finlayson-Pitts, *Chemistry of the Upper and Lower Atmosphere: Theory, Experiments, and Applications*. (Academic, New York, 1999).

[13] S. V. Levchenko and A. I. Krylov, J. Chem. Phys. **115**, 7485 (2001).

[14] M. Schwartz, L. R. Peebles, R. J. Berry, and P. Marshall, J. Chem. Phys. **118**, 557 (2003).

[15] M. J. Molina and L. T. Molina, Ann. Rev. Phys. Chem. **47**, 327 (1996).

[16] G. P. Brasseur, J. J. Orlando, and G. S. Tyndall, *Atmospheric Chemistry and Global Change*. (Oxford University Press, New York, 1999).

[17] T. Beiderhase, W. Hack, K. Hoyermann, and M. Olzmann, Z. Phys. Chem. **214**, 625 (2000).

[18] D. K. Maity, W. T. Duncan, and T. N. Truong, J. Phys. Chem. A **103**, 2152 (1999).

[19] J. S. Francisco, J. Phys. Chem. A **104**, 1499 (2000).

[20] Y. Chen and E. Tschuikow-Roux, J. Phys. Chem. **97**, 3742 (1993).

[21] R. W. Fessenden and R. H. Schuler, J. Chem. Phys. **39**, 2147 (1963).

[22] C. Yamada, E. Hirota, and K. Kawaguchi, J. Chem. Phys. **75**, 5256 (1981).

[23] D. E. Milligan and M. E. Jacox, J. Chem. Phys. **48**, 2265 (1968).

[24] R. W. Fessenden and R. H. Schuler, J. Chem. Phys. **43**, 2704 (1965).

[25] G. A. Carlson and G. C. Pimentel, J. Chem. Phys. **44**, 4053 (1966).

[26] S. V. Levchenko and A. I. Krylov, J. Phys. Chem. A **106**, 5169 (2002).

[27] J. Nolte and H. G. Wagner, Ber. Bunsenges. Phys. Chem. **101**, 1421 (1997).

[28] J. I. Raymond and L. Andrews, J. Phys. Chem. **75**, 3235 (1971).

[29] M. E. Jacox and D. E. Milligan, J. Chem. Phys. **50**, 3252 (1969).

[30] J. A. Mucha, D. A. Jennings, K. M. Evenson, and J. T. Hougen, J. Mol. Spec. **68**, 122 (1977).

[31] Y. Endo, C. Hamada, S. Saito, and E. Hirota, J. Chem. Phys. **79**, 1605 (1983).

[32] C. Yamada and E. Hirota, J. Mol. Spec. **116**, 101 (1986).

[33] J. W. Hudgens, C. S. Dulcey, G. R. Long, and D. J. Bogan, J. Chem. Phys. **87**, 4546 (1987).

[34] E. Riedle, S. H. Ashworth, J. T. Farrell, Jr., and D. J. Nesbitt, Rev. Sci. Instr. **65**, 42 (1994).

[35] J. T. Farrell, Jr., S. Davis, and D. J. Nesbitt, J. Chem. Phys. **103**, 2395 (1995).

[36] C. M. Lovejoy and D. J. Nesbitt, Rev. Sci. Instr. **68**, 807 (1987).

[37] F. Dong, D. Uy, S. Davis, M. Child, and D. J. Nesbitt, J. Chem. Phys. **122**, 224301 (2005).

[38] A. S. Pine, J. Opt. Soc. Am. **64**, 1683 (1974).

[39] A. S. Pine, J. Opt. Soc. Am. **66**, 97 (1976).

[40] F. Dong, personal communication (2005).

[41] J. K. G. Watson, in *Vibrational Spectra and Structure. A series of advances.*, edited by J. R. Durig (University of Southampton, Southampton, England), Vol. 6.

[42] E. Hirota, *High-Resolution Spectroscopy of Transient Molecules*. (Springer-Verlag, Berlin, 1985).

[43] C. Yamada, E. Hirota, and K. Kawaguchi, J. Chem. Phys. **75**, 5256 (1981).

[44] M. J. Frisch, G. W. Trucks, H. B. Schlegel, G. E. Scuseria, M. A. Robb, J. R. Cheeseman, J. A. Montgomery, T. Vreven, K. N. Kudin, J. C. Burant, J. M. Millam, S. S. Iyengar, J. Tomasi, V. Barone, B. Mennucci, M. Cossi, G. Scalmani, N. Rega, G. A. Petersson, H. Nakatsuji, M. Hada, M. Ehara, K. Toyota, R. Fukuda, J. Hasegawa, M. Ishida, T. Nakajima, Y. Honda, O. Kitao, H. Nakai, M. Klene, X. Li, J. E. Knox, H. P. Hratchian, J. B. Cross, V. Bakken, C. Adamo, J. Jaramillo, R. Gomperts, R. E. Stratmann, O. Yazyev, A. J. Austin, R. Cammi, C. Pomelli, J. W. Ochterski, P. Y. Ayala, K. Morokuma, G. A. Voth, P. Salvador, J. J. Dannenberg, V. G. Zakrzewski, S. Dapprich, A. D. Daniels, M. C. Strain, O. Farkas, D. K. Malick, A. D. Rabuck, K. Raghavachari, J. B. Foresman, J. V. Ortiz, Q. Cui, A. G. Baboul, S. Clifford, J. Cioslowski, B. B. Stefanov, G. Liu, A. Liashenko, P. Piskorz, I. Komaromi, R. L. Martin, D. J. Fox, T. Keith, M. A. Al-Laham, C. Y. Peng, A. Nanayakkara, M. Challacombe, P. M. W. Gill, B. Johnson, W. Chen, M. W. Wong, C. Gonzalez, and J. A. Pople, Gaussian 03 (Gaussian, Inc., Wallington, CT, 2004).

[45] E. S. Whitney, T. Haeber, M. D. Schuder, A. C. Blair, and D. J. Nesbitt, (in preparation).

[46] H.-J. Werner, P. J. Knowles, M. Schutz, R. Lindh, P. Celani, T. Korona, G. Rauhut, F. R. Manby, R. D. Amos, A. Bernhardsson, A. Berning, D. L. Cooper, M. J. O. Deegan, A. J. Dobbyn, F. Eckert, C. Hampel, G. Hetzer, A. W. Lloyd, S. J. McNicholas, W. Meyer, M. E. Mura, A. Nicklab, P. Palmieri, R. Pitzer, U. Schumann, H. Stoll, A. J. Stone, R. Tarroni, and T. Thorsteinsoon, MOLPRO: a package of ab initio programs (2003).

[47] K. A. Peterson, D. E. Woon, and T. H. Dunning, Jr., J. Chem. Phys. **100**, 7410 (1994).

[48] D. J. Rush and K. B. Wiberg, J. Phys. Chem. A **101**, 3143 (1997).

[49] J. T. Hougen, P. R. Bunker, and J. W. C. Johns, J. Mol. Spec. **34**, 136 (1970).

[50] T. Oka, J. Mol. Struct. **352/353**, 225 (1995).

CHAPTER 3

HIGH-RESOLUTION INFRARED STUDIES IN SLIT-JET DISCHARGES: SYMMETRIC CH_2 STRETCH EXCITATION OF JET-COOLED CH_2Cl RADICAL

3.1 Introduction

Over the last several decades, partially halogenated chlorofluorocarbons (HCFCs) have been used to replace their fully halogenated analogs (CFCs) as the principal components of refrigerants, fire suppressants, ground-based pesticides, and chemical vapor deposition processes, among others.[1-4] As a result, HCFCs currently represent one of the important sources of halogen atoms in the atmosphere.[5,6] The key motivation for use of HCFCs is the extreme stability of CFCs with respect to tropospheric oxidation and photolysis processes, which permit transport of the perhalogenated species into the stratosphere.[7] At stratospheric altitudes, halocarbon bonds in the CFCs can be photolyzed by solar UV radiation, yielding free halogen radicals that aggressively participate in catalytic depletion of the ozone layer.[8]

By way of comparison, HCFCs are much more kinetically susceptible to attack by tropospheric oxidants such as OH and HO_2, forming short-lived hydrohalocarbon radicals that can be further photolytically degraded by the longer solar wavelengths that reach into the troposphere.[5,6] This increased reactivity has naturally led to heightened interest in both the kinetic and spectroscopic properties of such open-shell hydrohalocarbon species in order to facilitate better monitoring and more accurate prediction of their long term impacts on the atmosphere. However, the transient nature of these radicals also presents significant experimental challenges, limiting ability to characterize structures, vibrational frequencies, and intramolecular potentials for such chemically reactive species. Nevertheless, recent years have witnessed substantial progress in laboratory detection and spectroscopic study of small polyatomic radicals, further complemented by high level *ab initio* computational efforts.[3,4,9-17]

Building upon these advances, this chapter presents the first high-resolution infrared spectra for jet-cooled CH_2Cl radicals in the symmetric (ν_1) CH_2 stretching mode. This open shell species is part of an atmospheric series of halosubstituted methyl derivatives, emerging from the early studies of the CH_3 radical itself. First identified by Fessenden and Schuler using Electron Spin Resonance (ESR), methyl radical is thought to have an effectively planar structure,[18] with later infrared spectroscopic studies in the inversion bend coordinate indicating a *negatively* anharmonic progression of vibrational levels. By way of a simple chemical picture, this anomalous vibrational anharmonicity arises from a competition between sp^3 (pyramidal) and sp^2 (planar) contributions to the C atom hybridization. These

competing structural influences result in an unusually "flat" potential for out-of-plane bending and therefore a more quadratic (i.e. "particle-in-a box" like) increase in vibrational eigenenergies. Indeed, the methyl radical is still a subject of controversy; the true equilibrium structure is probably nonplanar, though zero point energies above the barrier result in a vibrationally averaged planar geometry. The presence of large amplitude bending dynamics in CH_3 has stimulated considerable interest in the dependence of the bend potential and vibrationally averaged geometries upon halogen substitution, which can in principle be elucidated via high-resolution spectroscopic methods.

Early spectroscopic investigations of chloromethyl using low-temperature matrix isolation methods[19-22] enabled characterization of the symmetric C-Cl stretch (~ 830 cm^{-1}), the symmetric H-C-H bend (~ 1400 cm^{-1}), and the out-of-plane hydrogen bend (~ 400 cm^{-1}) at low resolution. Michaut *et al.* also recorded ESR spectra of the CH_2Cl radical in a low-temperature single crystal of CH_3Cl, deriving the magnetic hyperfine coupling constant for the Cl nucleus.[23] An important step into the gas phase was made by Hirota and co-workers, who recorded the first pure rotational spectrum of chloromethyl radical using microwave absorption methods, in which A-type transitions were observed with nearly fully resolved fine and hyperfine components for both the ^{35}Cl and ^{37}Cl isotopic species in the ground vibrational state.[24] More recently, Reisler and co-workers have probed the photodissociation dynamics of the gas-phase chloromethyl radical using ion imaging techniques, [25-27] with accompanying theoretical studies by Levchenko and Krylov.[27] Self-association rate constants for $CH_2Cl + CH_2Cl$ have been established,[28] and combined

experimental/theoretical investigations have probed the radical-radical reaction dynamics for $O(^3P) + CH_2Cl$.[29-31]

In their microwave studies of chloromethyl radical, Hirota and co-workers calculated a small positive inertial defect, $\Delta_0 = 0.0333$ amu A^2, from the rotational constants. This value suggests that chloromethyl radical is effectively planar (at least in a vibrationally averaged sense), which would also be consistent with a π radical $^2B_1$ ground electronic state. High-resolution studies of bromomethyl radical yield a similarly small and positive inertial defect, $\Delta_0 = 0.0320$ amu A^2, again suggesting a nearly planar structure.[32] This determination contrasts with the small but *negative* inertial defect calculated for the fluoromethyl radicalby Hirota,[33] $\Delta_0 = -0.0090$ amu A^2, also confirmed in recent studies from our group using high-resolution infrared absorption methods.[9] One suggestion has been that the less electronegative Cl and Br atoms, relative to F, contribute to a more planar geometry by limiting electron withdrawal from the central carbon atom toward the halogen substituent.[24]

The influence of halogen substituent on the inversion potential also has major impact on experimentally observed bending frequencies. For example, the ~ 400 cm^{-1} out-of-plane bending mode for CH_2Cl estimated from early matrix studies[19,20] is *higher* than the ~300 cm^{-1} vibrational frequency inferred from temperature-dependent microwave satellite bands for CH_2F radical,[9,24] despite the opposite trend anticipated from simple reduced mass considerations. Furthermore, theoretical attempts to replicate these frequencies, along with experimentally determined structures of these halogenated methyl radicals, have yielded significant discrepancies at the harmonic level. Specifically, the calculated *harmonic* out-of-plane bending frequency in CH_2Cl,

using both CCSD(T) and DFT methods, is 2-fold *smaller* than observed experimentally,[19,20] whereas the calculated *harmonic* frequency for the same mode in CH_2F is 2-fold *larger* than the experimental value.[33,34] Levchenko and Krylov have nicely reconciled these differences as the result of zero-point vibrational averaging over a shallow double minimum potential, which would also rationalize the large negative anharmonicity in the out-of-plane vibrational mode.[35]

In light of such a strong influence of halogenation on the bending potential, high-resolution infrared studies of these halomethyl radical species represent a particularly interesting target for investigation. The focus of the current study is on infrared spectroscopy in the CH_2 stretch manifold in chloromethyl radical, characterizing both ground and excited vibrational-state rotational constants, as well as fine structure parameters. The simple but quite versatile approach exploits dissociative attachment formation of the radical species in a high pressure pulsed slit discharge, followed by downstream direct infrared laser absorption in the resulting supersonic jet expansion. This allows these species to supersonically cool and therefore concentrate into their lowest accessible rotational levels, resulting in higher density per quantum state, dramatic simplification of the spectroscopic assignment process, and sub-Doppler spectral resolution due to velocity collimation in the slit jet. The net result is a powerfully general method for high-resolution IR spectroscopic study of reactive polyatomic radicals at low temperatures.

The organization of this chapter is as follows. The experimental setup and approach for infrared detection of CH_2Cl radicals is briefly summarized in Section 3.2. This is followed in Section 3.3 by spectroscopic results and analysis of the CH_2

symmetric stretch at rovibrational resolution and least-squares fits of the spectra to a Watson asymmetric top Hamiltonian. By virtue of sub-Doppler resolution in the slit-jet expansion, the results of the spin-rotation and hyperfine interactions are also presented and analyzed. Finally, Section 3.4 tackles a number of topics, comprising the development of a one-dimensional (1D) complete basis set (CBS) potential energy curve and associated wave functions by Numerov-Cooley methods, the extraction of vibrationally averaged structural information, and a comparison of the DFT calculation with experimentally observed vibrational band intensities. Section 3.5 summarizes and concludes the chapter.

3.2 Experiment

The experimental methods describing the slit supersonic discharge expansion have been outlined in detail elsewhere.[9,36-39] Briefly, the output of a tunable cw-ring dye laser is combined with the output of a single frequency argon ion laser inside a periodically poled lithium niobate (PPLN) crystal to generate tunable infrared light.[40] After exiting the PPLN crystal, the infrared light is split into two beams, one of which travels to a reference detector, while the other portion enters the vacuum chamber in which the radicals are produced. Once inside the chamber, the signal beam is multipassed 16 times through a Herriot cell, which is centered underneath the slit supersonic discharge expansion. The slit, 4 cm long and 300 microns wide, is arranged so that the long axis lies along the path of the signal beam. The pulsed valve is operated at a repetition rate of 19 Hz and a duty cycle of 50, generating gas pulses of ≈ 1ms. The electric discharge is achieved by applying – 0.6 kV to both sides of the

jaws and grounding the body of the pulsed valve so electrons flow from the jaws of the discharge upwards. In this manner, radicals are generated within the body of the pulsed valve and then allowed to supersonically cool. Common mode noise is eliminated by servo loop-controlled electronic subtraction between signal and reference InSb detectors.

Concentration modulation and phase sensitive detection at 50 kHz is additionally used to reduce the appearance of precursor absorptions. Generation of organic radicals is typically achieved by homolytic cleavage of a C-X bond (X = I, Br, Cl, F) to form a radical and a halogen atom. For chloromethyl radical, typical precursor mixtures of 0.11% bromochloromethane in Neon-70 were exposed to discharge currents of 0.6-0.9 A to generate radicals. Under these conditions, absorptions of 0.15-0.30% are observed, giving peak signal-to-noise ratios of ≈ 20:1. Stabilization of the argon ion laser to ≤ 1-2 MHz is achieved by stabilization on a 30 cm Fabry-Perot marker cavity, which in turn is actively locked over multiple days to a polarization-stabilized HeNe laser. The dye laser is locked onto a stabilized Fabry-Perot etalon and typically scanned in 6.5 MHz steps, which proves adequate to fully resolve fine structure due to spin-rotation interactions, with residual linewidths due to hyperfine structure and suppressed Doppler broadening. Relative frequency differences (< 10 MHz day-to-day reproducibility) are obtained by recording dye laser fringes on the marker cavity, with absolute infrared frequencies referenced to R(3), R(2), and R(1) lines of methane.[41]

3.3 Results and Analysis

3.3.1 *Symmetric CH_2 stretch line center assignments*

Since this study reflects the first infrared detection and spectral assignment for chloromethyl radical, high quality vibrational predictions prove extremely useful to minimize the search region to be scanned at high resolution. In previous work, DFT calculations [B3LYP/6-311++G (3df, 3dp)] have been used to predict harmonic hydride stretching vibrational frequencies (CH, OH, NH) in multiple radicals and molecular ions, and to benchmark these against spectroscopic band centers observed experimentally.[42] This analysis revealed a high correlation between theory and experiment, suggesting that hydride stretching vibrations in unknown radicals can be predicted to within a sufficiently small window of ± 5-10 cm^{-1}. Based on such frequency correlations, the symmetric and antisymmetric CH_2 stretch vibrations in chloromethyl are predicted at approximately 3055 cm^{-1} and 3201 cm^{-1}, respectively. Furthermore, these DFT frequency calculations also predict the ν_1 symmetric stretch band intensity to be relatively strong (6.15 km/mol), whereas the antisymmetric stretch intensity is quite anomalously weak (0.14 km/mol). This unusual ratio of band intensities (I_{sym}/I_{asym} nearly 45:1) is inconsistent with the more typical intensity behavior (I_{sym}/I_{asym} = 0.5) for the CH_2 group, as can be seen by comparing with the corresponding symmetric (1.61 km/mol) and antisymmetric stretch (3.84 km/mol) vibrations in CH_2D. Interestingly, these predictions indicate that chloro-substitution in methyl radical results in a substantial *increase* in symmetric stretch intensity, and

yet *virtual elimination* of the antisymmetric stretch mode intensity. We will return to this point in the discussion section.

Trial scans for the symmetric stretch quickly reveal strong progressions of jet-cooled $CH_2{}^{35}Cl$ and $CH_2{}^{37}Cl$ absorption lines between 3050 and 3060 cm^{-1}, in close agreement with the scaled DFT predictions above. After optimization of the precursor gas mixture and scanning conditions, continuous single-mode spectra from 3040 to 3070 cm^{-1} are then obtained for chloromethyl radical, yielding strong P and R branch progressions characteristic of an A-type band (consistent with expectations for the symmetric stretch) and with what appears to be relatively weak Q-branch structure in the vicinity of 3055 cm^{-1}. Due to the presence of ^{35}Cl and ^{37}Cl, the two isotopomer rotational progressions are strongly overlapped, requiring closer examination to unambiguously confirm assignment of the respective band origins.

A sample region of the P-branch rotational progression in the symmetric stretch vibration of chloromethyl radical is shown in Figure 3.1, highlighting contributions from both $CH_2{}^{35}Cl$ and $CH_2{}^{37}Cl$. A-type transitions from the $K_a = 0$ and $K_a = 1$ manifolds are observed for both isotopes of chlorine, with clear evidence of partially resolved structure on each peak due to intramolecular fine (electron spin-rotation) and hyperfine (nuclear dipole-dipole, quadrupole and fermi contact) interactions. Furthermore, an approximately ≈ 3:1 intensity ratio is observed between transitions out of the two $K_a = 0$: $K_a = 1$ manifolds, which is consistent with a partially filled "π-radical" center on the central carbon atom and cooling down into the lowest (3:1 for ortho:para) nuclear spin statistics for the two identical H atoms.

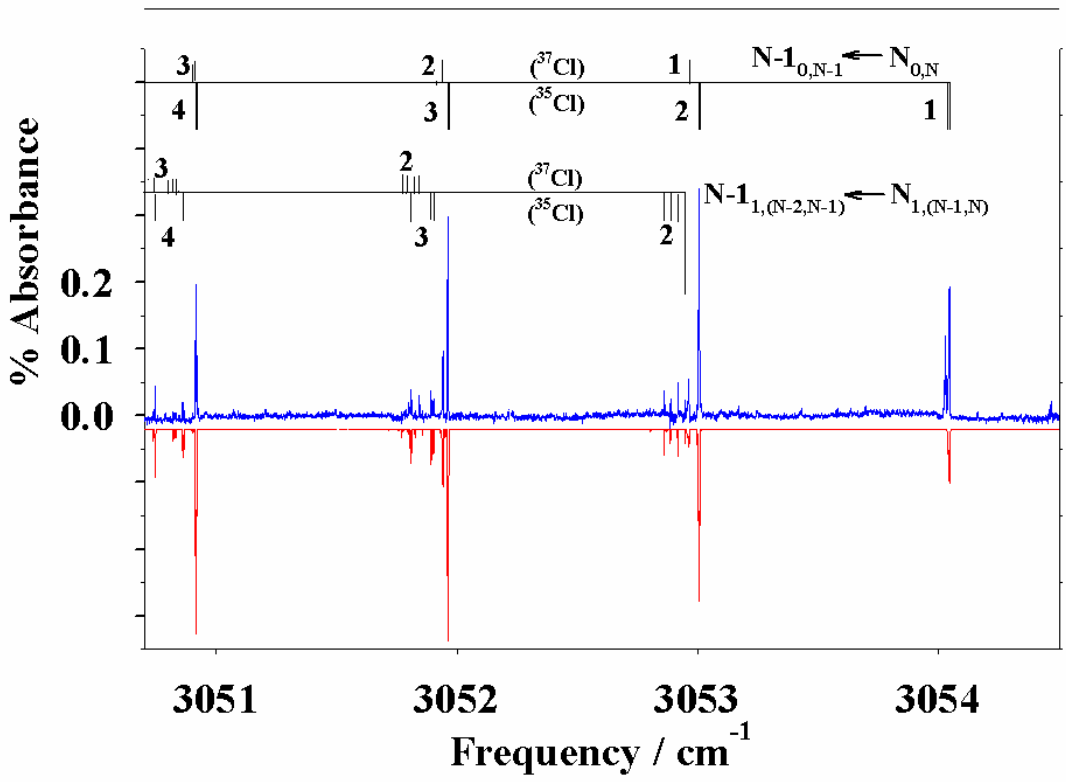

Figure 3.1 Sample spectral data (a) for selected P-branch transitions in the CH_2 symmetric stretch band of CH_2Cl, compared with a calculated spectrum from the full least squares fit.

As expected from the previous microwave work of Hirota and co-workers,[24] a ~ $2B \approx 1.02$ cm^{-1} separation between P-branch transitions for each of the isotopomer bands is observed, but with strong interleaving between the two isotopomers due to a vibrational band shift accidentally commensurate with 2B. Specifically, the band center of the $CH_2{}^{37}Cl$ symmetric stretch is shifted ≈1.10 cm^{-1} (i.e., also ≈ 2B) to the red of the $CH_2{}^{35}Cl$ band, due to increased reduced mass for the ^{37}Cl isotopomer. This can be readily rationalized by G matrix analysis, which for a simple model of a rigid CCl bond would yield an effective symmetric stretch mass of

$$\mu_{eff} = (1/\mu_{H\text{-}CCl} + \cos(\theta_{HCH})/2M_{Cl})^{-1}, \qquad (3.1)$$

For a 120° HCH bond angle, this translates in the perturbative limit into a fractional change in vibrational frequencies of

$$\Delta\nu/\nu \approx 3/8[M_H/m_{C35Cl} - M_H/m_{C37Cl}], \qquad (3.2)$$

This expression predicts a roughly 0.99 cm^{-1} isotopic shift for a 3055 cm^{-1} symmetric stretch vibration, which, given the simplicity of the model, is in good agreement with the 1.10 cm^{-1} value observed experimentally.

Identification of the isotopomer vibrational band origins can be readily made from ground-state combination difference estimates based on the strongest P, R branch transitions, with further assignment proceeding rapidly by comparing experimental data with rigid asymmetric top spectra predicted from microwave constants. Quantitative confirmation of these assignments with four-line (and ground-state two-line) combination differences are complicated by the extensive fine and hyperfine structure superimposed on each $N_{KaKc} \leftarrow N_{KaKc}$ transition. This structure results in asymmetric contour shift and splittings of up to several GHz, i.e., greatly in excess of the putative experimental precision (< 10 MHz). As discussed elsewhere, a more sophisticated simulation program has been developed that includes the standard Watson asymmetric top Hamiltonian, plus all fine (spin rotation) and hyperfine (Fermi contact, dipole-dipole and electric quadrupole) coupling terms utilized in the microwave analysis for a spin ½ electron and two nuclei with non-zero spin. This complete Hamiltonian is used for a full least-squares analysis of all line profiles, as discussed later in this section.

For initial assignments, however, we focus exclusively on the rovibrational information by predicting fine/hyperfine line profiles for a given $N_{KaKc} \leftarrow N_{KaKc}$

transition (estimated from Hirota's ground-state constants) and convoluted over the ~ 60 MHz sub-Doppler linewidth in the slit jet. By shifting these predicted profiles with respect to the high-resolution data, the pure asymmetric top (i.e., "fine and hyperfine free") transition frequencies can be determined to much less than the reported uncertainty. In this fashion, 41 fine/hyperfine free line centers have been identified in the $CH_2{}^{35}Cl$ symmetric stretch and 26 for $CH_2{}^{37}Cl$. These line centers comprise transitions from states up to N = 8 and 9 in the $CH_2{}^{35}Cl$ R and P branches (see Table 3.1), respectively, and up to N = 8 and 7 in the $CH_2{}^{37}Cl$ R and P branches (see Table 3.2), respectively. By way of initial analysis, these fine/hyperfine-free transition frequencies are least-squares fit to a Watson asymmetric top Hamiltonian for the ground and symmetric stretch excited states. Within experimental uncertainty, the fitted ground-state rotational constants are completely consistent with previous results of Hirota and co-workers, yielding standard residuals of 9 MHz and 11 MHz for the ^{35}Cl and ^{37}Cl isotopomers, respectively. The upper state rotational constants extracted from the fit are summarized in Table 3.3.

Table 3.1: Transition frequencies and least-squares fit for the $CH_2{}^{35}Cl$ symmetric stretch

J'	K_a'	K_c'	*J"*	K_a"	K_c"	*Obs. (cm^{-1})*	*Obs. – calc. (10^{-4} cm^{-1})*
9	0	9	8	0	8	3064.17536	-0.6
8	0	8	7	0	7	3063.18267	1.9
7	0	7	6	0	6	3062.18573	-12.
7	1	7	6	1	6	3061.96625	1.4
6	0	6	5	0	5	3061.18363	0.9
6	1	5	5	1	4	3061.16849	3.6
6	1	6	5	1	5	3060.98041	2.1
5	0	5	4	0	4	3060.17729	0.1
5	1	4	4	1	3	3060.14554	2.8
5	1	5	4	1	4	3059.98951	-3.0
4	0	4	3	0	3	3059.16687	4.7
4	1	3	3	1	2	3059.11869	4.8
4	1	4	3	1	3	3058.99515	3.5
3	0	3	2	0	2	3058.15108	2.5
3	1	2	2	1	1	3058.08722	3.2
3	1	3	2	1	2	3057.99539	3.6
2	0	2	1	0	1	3057.13074	1.8
2	1	1	1	1	0	3057.05171	5.2
2	1	2	1	1	1	3056.99123	8.1
1	0	1	0	0	0	3056.10592	3.2
1	1	0	1	1	1	3054.99189	1.7
1	1	1	1	1	0	3054.93168	-2.1
0	0	0	1	0	1	3054.04157	-2.0
1	0	1	2	0	2	3053.00279	-2.6
1	1	1	2	1	2	3052.92237	-5.3
1	1	0	2	1	1	3052.86383	-1.9
2	0	2	3	0	3	3051.95964	-3.2
2	1	2	3	1	3	3051.89377	-0.7
2	1	1	3	1	2	3051.80602	-2.2
3	0	3	4	0	4	3050.91258	-0.6
3	1	3	4	1	4	3050.86007	0.1

Table 3.1 (continued): Transition frequencies and least-squares fit for the $CH_2{}^{35}Cl$ symmetric stretch

J'	K_a'	K_c'	*J"*	K_a"	K_c"	*Obs. (cm^{-1})*	*Obs. – calc. (10^{-4} cm^{-1})*
3	1	2	4	1	3	3050.74390	-3.3
4	0	4	5	0	5	3049.86107	-2.2
4	1	4	5	1	5	3049.82131	-3.9
4	1	3	5	1	4	3049.67771	-3.9
5	0	5	6	0	6	3048.80589	-2.2
5	1	5	6	1	6	3048.77842	-4.8
5	1	4	6	1	5	3048.60714	-9.0
6	0	6	7	0	7	3047.74721	-1.1
7	0	7	8	0	8	3046.68486	-3.4
8	0	8	9	0	9	3045.61979	-2.5

Table 3.2: Transition frequencies and least-squares fit for the $CH_2{}^{37}Cl$ symmetric stretch

J'	K_a'	K_c'	*J"*	K_a"	K_c"	*Obs. (cm^{-1})*	*Obs. – calc. (10^{-4} cm^{-1})*
9	0	9	8	0	8	3063.05405	0.2
8	0	8	7	0	7	3062.05490	0.4
7	0	7	6	0	6	3061.05324	0.3
6	0	6	5	0	5	3060.04933	1.8
5	0	5	4	0	4	3059.04312	3.9
5	1	4	4	1	3	3058.98241	2.2
5	1	5	4	1	4	3058.83301	-1.2
4	0	4	3	0	3	3058.03430	2.6
4	1	3	3	1	2	3057.95777	0.3
4	1	4	3	1	3	3057.83908	-0.9
3	0	3	2	0	2	3057.02346	3.2
3	1	2	2	1	1	3056.93170	2.1
3	1	3	2	1	2	3056.84360	5.4
2	0	2	1	0	1	3056.01035	2.2
2	1	1	1	1	0	3055.90351	0.5
1	0	1	0	0	0	3054.99506	-0.1
1	1	1	1	1	0	3053.81074	-5.0
0	0	0	1	0	1	3052.95915	-0.2
1	0	1	2	0	2	3051.93858	0.7
2	0	2	3	0	3	3050.91574	-4.2
3	0	3	4	0	4	3049.89208	1.3
3	1	2	4	1	3	3049.69873	-4.5
4	0	4	5	0	5	3048.86658	-1.9
5	0	5	6	0	6	3047.83953	-4.0
5	1	4	6	1	5	3047.61799	-3.3
6	0	6	7	0	7	3046.81140	-4.0

Table 3.3: Least-squares fitting results for the symmetric CH_2 stretch line centers in $CH_2{}^{35}Cl$ and $CH_2{}^{37}Cl$. The uncertainties in parenthesis represent one standard deviation from the least-squares fit to the Watson asymmetric top Hamiltonian.

Constants (cm^{-1})	$CH_2{}^{35}Cl$ Excited State	$CH_2{}^{37}Cl$ Excited State
A	9.04055(20)	9.01341(25)
B	0.52991(1)	0.52310(1)
C	0.49971(1)	0.49391(1)
Δ_N ($\times 10^{-5}$)	-0.06(1)	0.05(1)
Δ_{NK} ($\times 10^{-5}$)	6.3(8)	2.(1)
Δ_K ($\times 10^{-5}$)	76.[a]	76.[a]
υ_0	3055.0760(2)	3053.9781(1)

[a] Parameters previously determined by Hirota *et al.* Ground-state parameters were also set to Hirota's values.

3.3.2 *Fine and hyperfine structure and analysis*

As mentioned above, the experimental spectra show clear fine structure splittings, resulting predominantly from coupling of electron spin angular momentum (**S**) with overall molecular rotation (**N**).[9,43] There is also additional line broadening evident from extensive hyperfine interactions due to three nuclei with non-zero spins. In the interest of completeness, analysis of these features in both the $CH_2{}^{35}Cl$ and $CH_2{}^{37}Cl$ manifolds is based on a full least-squares fit to the explicit actual absorption line contours, utilizing the complete asymmetric top, fine, and hyperfine Hamiltonian. This simulation program has been developed for spin rotation, Fermi contact, dipole-dipole, and electric quadrupole terms in an asymmetric top with multiple non-zero spin nuclei, utilizing coupling matrix elements from Hirota[44] and extensively tested in collaborative comparison with program development by the Brown group in Oxford.

By way of example, sample data scans over the $3_{13} \leftarrow 2_{12}$ transition ($I_H = 0$, para) in the symmetric stretch band of $CH_2{}^{35}Cl$ are shown sequentially in Figure 3.2. The top panel (a) illustrates the single ~60 MHz Doppler line profile anticipated in the absence of any electron or nuclear spin interactions, with the results in panels below illustrating the additional splittings and broadenings that result from successive inclusion of (b) electron spin-rotation fine structure and (c) nuclear spin Fermi contact, dipole-dipole, and electric quadrupole hyperfine structure. The observed experimental line profile for this transition is given in panel (d) and is in qood agreement with the least-squares fitted fine/hyperfine predictions. The electron spin fine structure clearly contributes to well-resolvable peaks in the predicted spectrum, although the nuclear hyperfine contribution is below the resolution limit. Experimental access to such high resolution information in the near infrared is noteworthy, observable as a result of the sub-Doppler velocity collimation in the slit-jet.

In final fits to the high resolution profiles, all ground-state constants are fixed at previously determined microwave values,[24] floating the rotational and spin-rotation constants in the vibrationally excited state. The absorption contours do exhibit partial sensitivity to hyperfine constants, however, much less than observed previously in IR studies of CH_2F radical. To further minimize parameter correlation, the hyperfine interaction is held fixed at ground-state values. A summary of the fitted results is reported in Table 3.4; the results indicate only modest (albeit statistically significant) changes in the three spin rotation constants upon vibrational excitation.

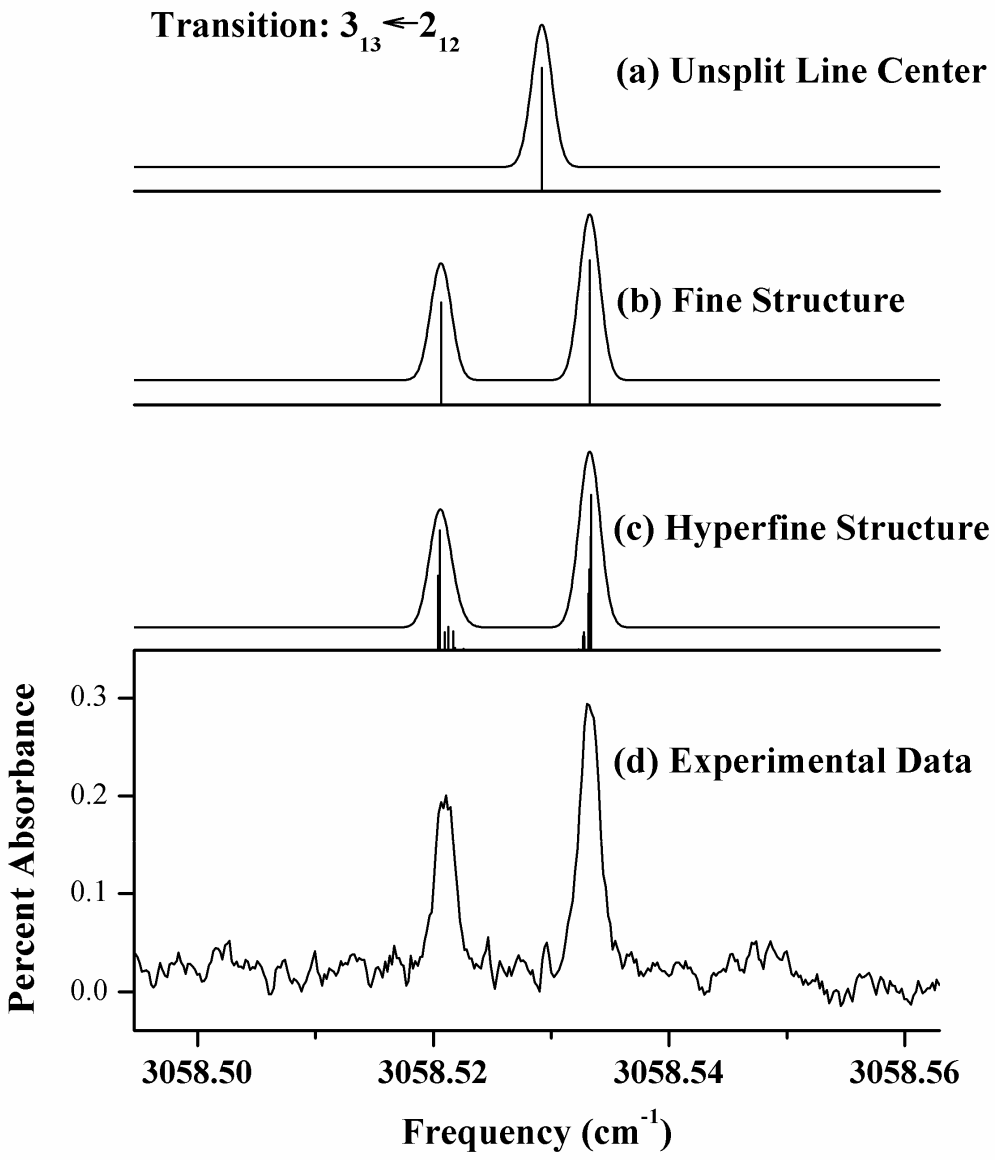

Figure 3.2 Comparison between high resolution predictions (a-c) and experiment (d) for a sample symmetric stretch rovibrational transition ($3_{13} \leftarrow 2_{12}$) of CH_2Cl. The simulations begin with a pure asymmetric top transition (i.e. $S = I_{Cl} = I_H = 0$) (a), successively including fine (b) and hyperfine (c) interaction terms in the Hamiltonian.

Table 3.4: Least-squares fitting results for the CH_2 symmetric stretch fine-structure constants. The uncertainties in parentheses represent one standard deviation from the least-squares fit to the effective Hamiltonian detailed in the text.

Constants (MHz)	$CH_2{}^{35}Cl$ Ground State	$CH_2{}^{35}Cl$ Excited State	$CH_2{}^{37}Cl$ Ground State	$CH_2{}^{37}Cl$ Excited State
ε_{aa}	-3149.45(36)[a]	-3047.(4)	-3149.58(24)[a]	-3103.(28)
ε_{bb}	-237.623(114)[a]	-236.3(8)	-234.080(118)[a]	-231.(4)
ε_{cc}	11.814(100)[a]	10.6(8)	11.699(100)[a]	10.(4)

[a] Parameters previously determined by Hirota *et al.*

3.4 Discussion

3.4.1 *CCSD(T) Complete Basis Set (CBS) bending potential*

As previously introduced in a companion high-resolution IR study of the CH_2F radical, the planar versus bent equilibrium geometric structure of CH_2Cl remains an intriguing question, indirectly sampling the competition between sp^2 versus sp^3 hybridization of the central carbon atom. At the simplest level, one can consider the inertial defect, $\Delta = I_c - I_b - I_a$, which for CH_2Cl is quite small in the ground ($\Delta \approx 0.033$ amu A^2) state. Purely from analysis of the rotational constants, both the microwave and infrared data are consistent with a nearly planar equilibrium structure. However, this is not sufficient to rule out large amplitude motion in the bending coordinate which, if energetically above any barrier at planarity, can lead to substantial delocalization of the wave function. Indeed, CH_2F also exhibits inertial defects close to zero in the ground (-0.0096 amu A^2) state, despite the fact that the actual bending potential is decidedly nonplanar, with a minimum at $\theta \approx 29^\circ$ and a nearly 132 cm^{-1} barrier to planarity. Inertial defects close to zero can also arise from

dynamical competition between large amplitude in-plane and out-of-plane motions, which tend to raise or lower the inertial defect, respectively. Such large amplitude averaging effects have made it difficult historically to establish the presence of barriers based on rotational constants alone. Indeed, CH_3 is an example where the barrier to planarity is thought to be quite small or possibly even zero and, in any event, negligible with respect to the zero point energy. In light of the nearly zero and non-zero barriers for CH_3 and CH_2F, respectively, the question of a barrier height in CH_2Cl naturally occurs, or, alternatively stated, the degree of sp^2 versus sp^3 hybridization in methyl radical as a function of electronegative substitution is of great interest.

Krylov and co-workers have performed CCSD(T) calculations for CH_2Cl using a 6-311G++(3df,2pd) basis set, predicting a planar equilibrium structure with a large negative anharmonic potential for the out-of-plane bending vibrational mode.[45] From an approximate 1D analysis, the anharmonic frequency for this transition was estimated to be 422 cm^{-1}. As a measure of the nonharmonic nature of the potentials, this value is more than *twice* the harmonic frequency of 168 cm^{-1}, though still in reasonable agreement with the experimentally determined matrix values of 402 cm^{-1}.[19,20] Interestingly, this out of plane CH_2Cl prediction is ~30% *smaller* than the corresponding bend frequency for methyl radical of 600 cm^{-1}, but nevertheless ~30% *larger* than experimentally inferred for CH_2F (~300 cm^{-1}).[33] This discrepancy is clearly not due to simple reduced mass G-matrix effects, which are dominated by the hydrogen atoms and in fact predict only a < 5 % decrease in bend frequencies for chlorine substitution.

This provides sufficient motivation to revisit this issue with a complete basis set (CBS) *ab initio* treatment of the inversion bending potential. Calculational details closely parallel that described elsewhere in our experimental high-resolution study of CH_2F radical; the essential features can be briefly summarized. CCSD(T) geometry optimizations have been performed as a function of inversion bending angle, θ (defined as 180° minus the angle between the CCl bond and the CH_2 plane) in an AVnZ Dunning basis set, exploiting efficient quantum chemistry routines available from MOLPRO.[46] To correct for finite basis set effects, the CCSD(T) energies for n = 2, 3, 4 are extrapolated to the CBS limit, using the methods of Dunning and Peterson.[47] This 1D CBS bending potential is then corrected for zero point vibrational energy in the remaining 3N-7 = 5 coordinates, resulting in the adiabatic potential curve for CH_2Cl shown in Figure 3.3. In sharp contrast with the predictions for CH_2F, the equilibrium geometry of CH_2Cl at the CBS limit is essentially planar, though the potential is quite visibly flat rather than harmonic.

Calculation of adiabatic bending eigenenergies and wave functions on this 1D potential is modeled on the work of Rush and Wiberg,[48] which, in turn, is based on the large-amplitude rigid-bender effective Hamiltonian analysis of Hougen, Bunker and Johns.[49] Note that these polyatomic methods explicitly take the angular dependence of the inertial moments into account, which is necessary to obtain true anharmonic vibrational predictions correctly independent of the arbitrary choice of 1D bending coordinate. The resulting ground (E_0 = 178 cm^{-1}) and first excited state (E_1 = 571 cm^{-1}) energies and vibrational wave functions for CH_2Cl, calculated for the zero-point corrected potential energy curve, are displayed in Figure 3.3.

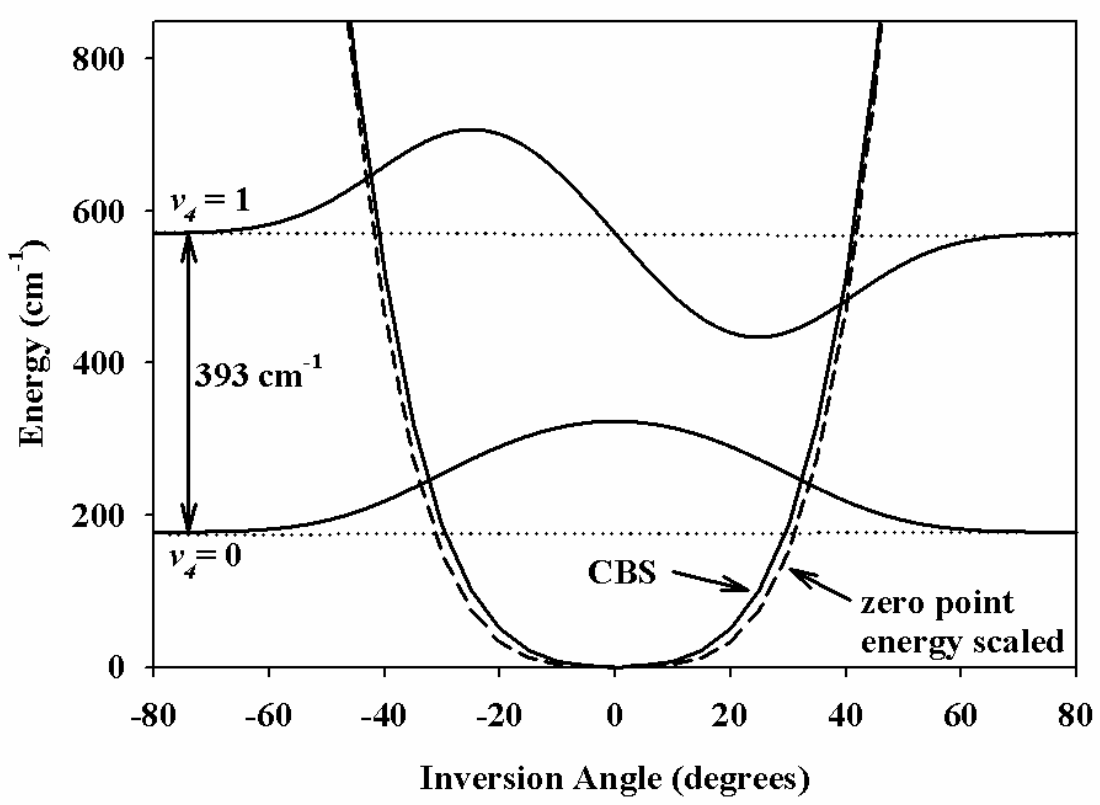

Figure 3.3 One dimensional potential energy curve from CCSD(T)/AVnZ/CBS calculations, adiabatically corrected for zero point energy in all remaining non-bend coordinates. Also shown are ground and first excited vibrational state (v_4) eigenfunctions and eigenenergies, calculated via methods of Rush and Wiberg and explicitly including G matrix element dependence on the bend angle (see text for details).

The predicted anharmonic 1←0 vibrational bend frequency on this CBS potential is $E_{1\leftarrow0}$ = 393 cm^{-1}, consistent with previous theoretical estimates and in agreement with experimental matrix studies (400 cm^{-1}). In the interest of facilitating direct spectroscopic observation of this inversion mode, we also calculate higher vibrational states on this surface to be E_2 = 1083 cm^{-1}, E_3 = 1654 cm^{-1}, and E_4 = 2268 cm^{-1}. This predicts a series of hot band origins with $\Delta E_{2\leftarrow1}$ = 512 cm^{-1}, $\Delta E_{3\leftarrow2}$ = 571 cm^{-1}, and $\Delta E_{4\leftarrow3}$ = 614 cm^{-1}, potentially observable with current diode laser technology in the ≈

600 cm^{-1} region. Particularly noteworthy is the *negatively* anharmonic (i.e., *blue* shifted) progression of adjacent level spacings, which converges toward more harmonic behavior with increasing number of vibrational quanta. This is entirely consistent with competing sp^3 contributions to a nominally sp^2 bending potential, resulting in an anomalously flat topography near planarity.

The calculations and experimental data elucidate a striking qualitative difference between chloro- and fluoro-substituted methyl radicals, suggesting a strong dependence to the barrier contribution on the electronegativity of the substituent. To complete this picture, we have also calculated a 1D CCSD(T) potential surface for the methyl radical itself at the same level of CBS treatment. The result for all three potentials in this CH_2X (X = H, Cl, F) series is shown in Figure 3.4. This figure illustrates the unambiguous progression from a relatively harmonic potential for methyl radical, to a much flatter potential for chloromethyl radical, and finally, to the distinctly double-minimum potential for fluoromethyl. The difference between the strongly bent equilibrium geometry for CH_2F radical and the successively more confined planar equilibrium structures of CH_2Cl and CH_3 is striking, and nicely underscores an increasing propensity toward sp^3 hybridization with greater electron withdrawal from the central C atom.

3.4.2 *Vibrational band intensities*

Boltzmann analysis is used to compare the intensities of the $CH_2{}^{35}Cl$ and $CH_2{}^{37}Cl$ symmetric stretch bands. Boltzmann analysis yields both a rotational temperature of the radicals as well as the relative intensities of the two bands.

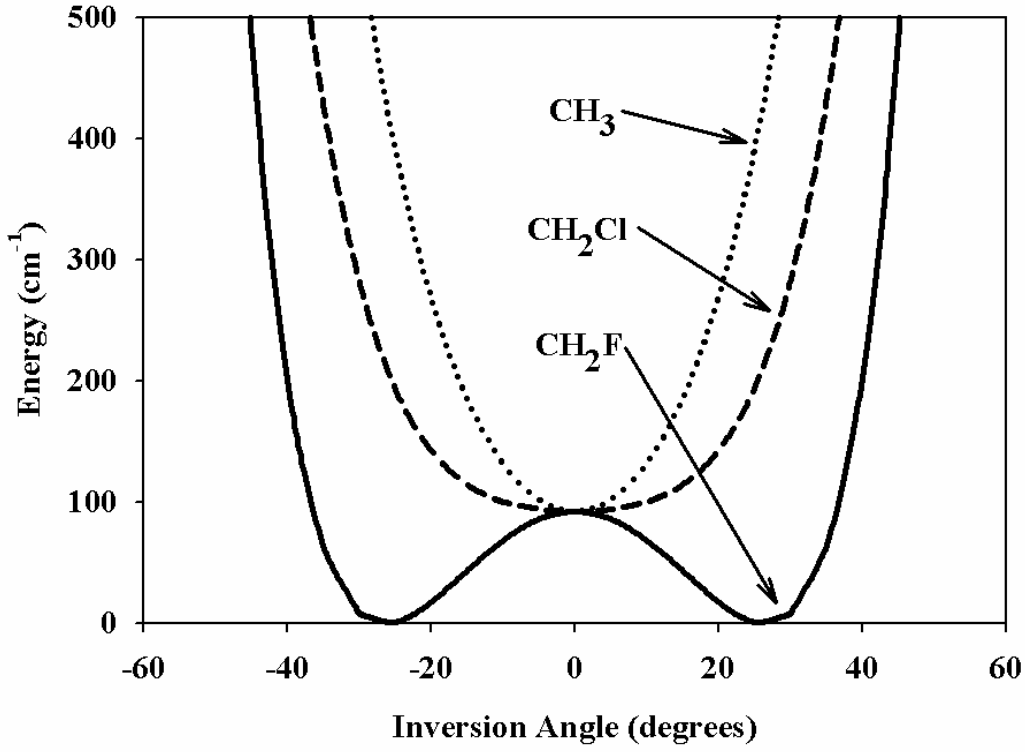

Figure 3.4 Comparison of one dimensional potential energy curves from CCSD(T)/AVnZ/CBS calculations, for CH_3, CH_2Cl, and CH_2F. Note the clear progression toward a non-planar equilibrium geometry, due to increasing sp^3 vs sp^2 hybridization of the carbon atom with increasing electronegativity of the halogen substituent.

Following calculations described previously,[39] the experimentally measured integrated line absorbance for a rotational transition from a lower state *i* to an upper state *j* is expressed as

$$S_{\text{exp}} = \int A(v)dv = N^i \cdot l \cdot S_0^{ji}, \tag{3.3}$$

where N^i is the number density of molecules in the lower state *i*, *l* is the absorption length (64 cm), and S_0^{ji} is the line strength per M_J state. The number density of molecules in the lower state, N^i, can be expanded in the following expression,

$$N^i = N_0^{vib} \cdot \frac{g_{NS} \cdot g_J}{Q_{ROT}^{NS}} \cdot e^{-(E_i - E_0^{NS})/kT_{ROT}}, \qquad (3.4)$$

where N_0^{vib} is the population in the specific vibrational state *vib*, g_{NS} is the nuclear spin weight, g_J is the rotational degeneracy, E_0^{NS} is the lowest energy level within the same nuclear spin symmetry, and Q_{ROT}^{NS} is the rotational partition function of a particular nuclear spin symmetry.

Data for $CH_2{}^{35}Cl$ symmetric band transitions for $\Delta J = 1$ and ground-state $K_a = 0$ are shown in Figure 3.5. For each transition, the integrated line absorbance, S_{exp}, is scaled by the calculated line strength factor, including nuclear spin statistics weighting and is plotted semilogarithmically against the ground-state rotational energy. A linear least squares fit shows a corresponding temperature of 18.2(5) K. Integration of band strengths for both $CH_2{}^{35}Cl$ and $CH_2{}^{37}Cl$ yield an intensity ratio of 2.6(2), which is also in rough agreement with the 3:1 ratio of their natural abundances.

With the symmetric CH_2 stretch band observed with high signal to noise (≈ 20:1), experimental conditions maximized for most efficient formation of CH_2Cl, and high confidence in vibrational band origin predictions, a scan for the antisymmetric CH_2 stretch has been attempted. No CH_2Cl radical transitions are observed for either isotopomer that, based on a ≈ 20:1 signal to noise in the corresponding symmetric stretch region, permits us to safely conclude that the band intensity is *at least* tenfold weaker. This is consistent with the theoretical intensity predictions of a 45-fold difference between the symmetric and antisymmetric stretch band strengths.

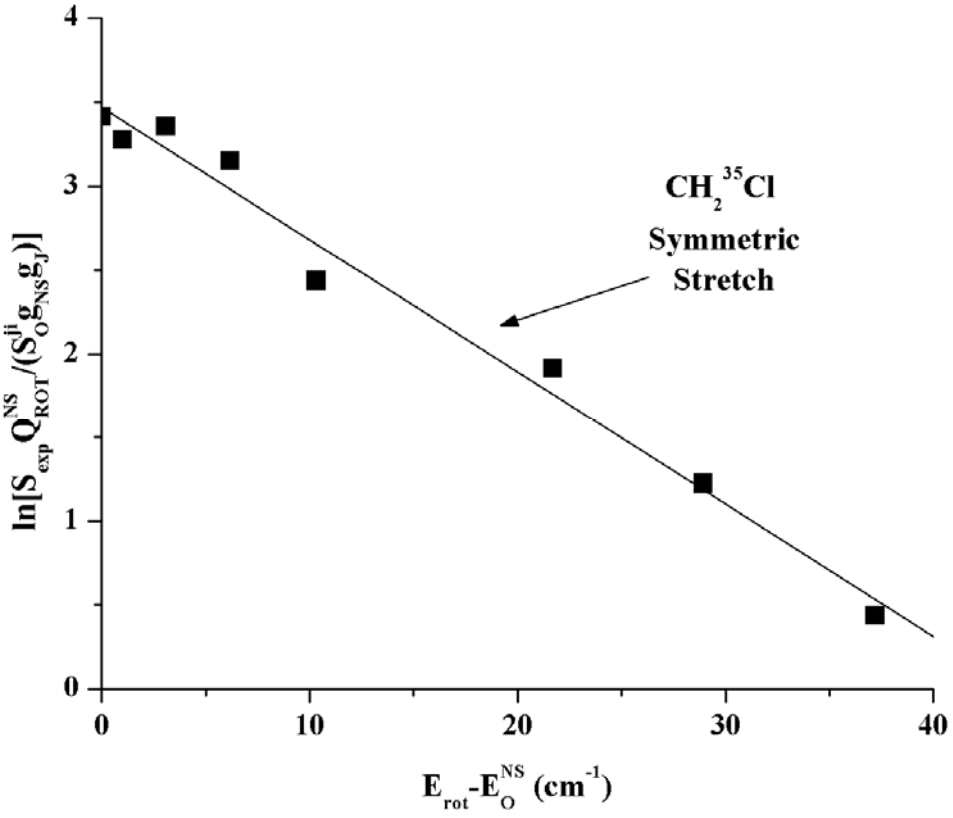

Figure 3.5 Boltzmann temperature analysis of the $CH_2{}^{35}Cl$ symmetric stretch band verifying rotational equilibration to $T_{rot} \approx 15$ K in the slit jet.

This experimental confirmation of such dramatic weakening of the antisymmetric CH_2 stretch with chloro vs. fluoro substitution represents one of the more intriguing results of this study and deserves closer investigation. It is important to note that *both* symmetric and antisymmetric stretch bands are experimentally observed for CH_2F in a 1.8(2):1 ratio, in quantitative agreement with *ab initio* theoretical predictions of 2.1:1. A simple bond-dipole model predicts an intensity ratio of the symmetric vs. antisymmetric stretches of 1:3, where the antisymmetric stretch intensity is *larger* than that of the symmetric stretch. This is confirmed in theoretical calculations for CH_2D, reaffirming confidence in the general paradigm for

CH_2 stretch intensities. However, this prediction is incorrect by approximately sixfold for CH_2F and *at least* by 60-fold for CH_2Cl. Furthermore, from comparison with CH_2D, this is not simply due to a *decrease* in asymmetric stretch intensity, but rather must also result in part from an *increase* in symmetric stretch intensity.

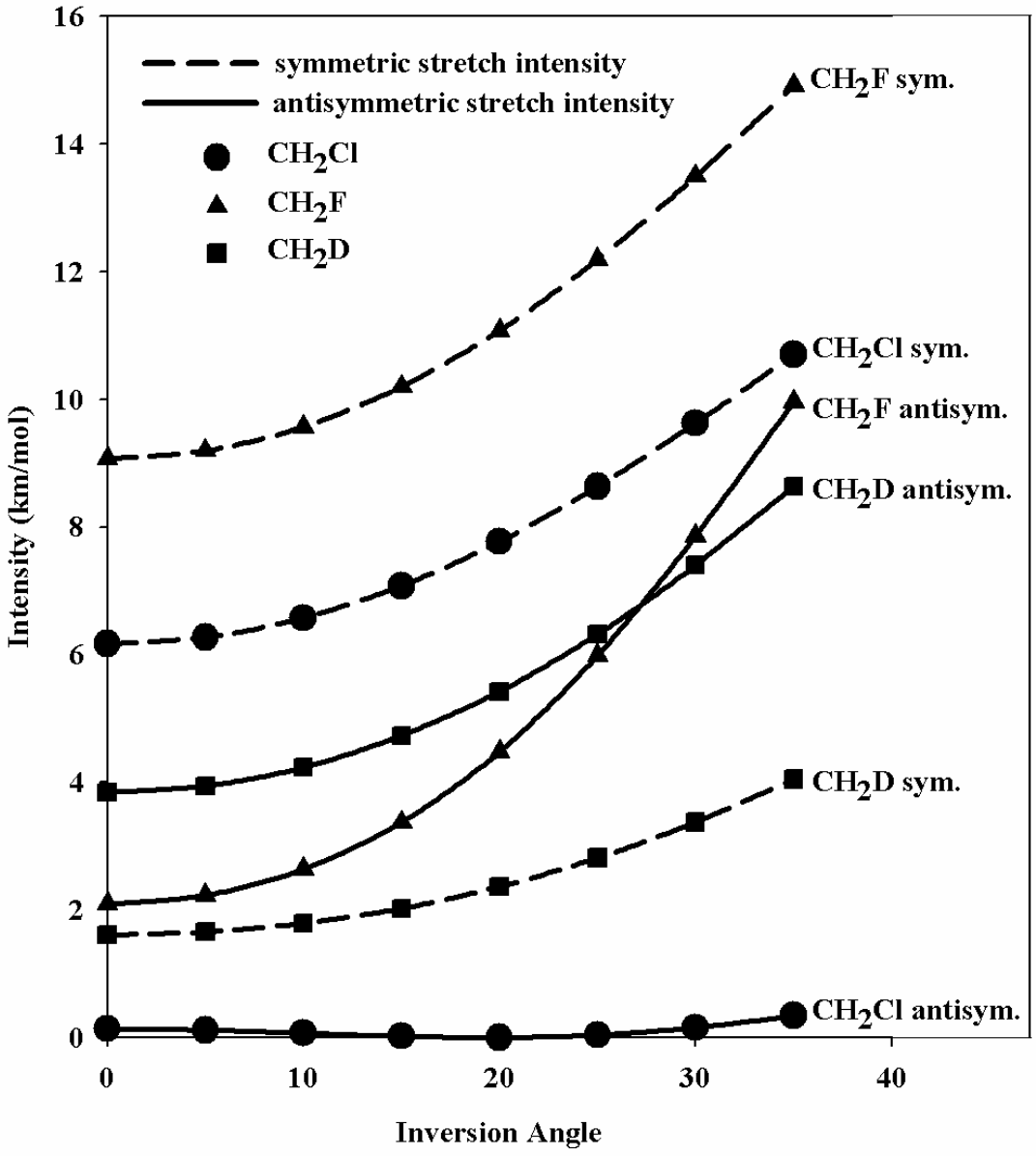

Figure 3.6 Predicted band intensities of CH_2 symmetric and antisymmetric stretch vibrations for CH_2Cl, CH_2F, and CH_2D as a function of inversion angle. .

This trend is illustrated in Figure 3.6, which shows a comparison between the calculated symmetric and antisymmetric CH_2 stretch intensities for CH_2F, CH_2Cl, and CH_2D as a function of out of plane bend angle. Clearly, halogen substitution of methyl radical has a profound impact on the origin of vibrational intensities.

This dramatic variation in CH_2 stretch intensities between CH_2D, CH_2F, and CH_2Cl, warrants closer investigation. The significant increase in symmetric stretch excitation with halogenation seems at first glance consistent with a simple bond dipole model, whereby a larger μ_{CX} results in a larger dipole moment derivative. However, inspection of the normal mode displacements indicates these effects contribute in the wrong direction – specifically the CX bond length *decreases* slightly with symmetric extension of the CH bonds. Furthermore, the center of mass displacement of halide atom for asymmetric stretch excitation is relatively small, whereas the dynamic range in intensity changes for this mode is by far the largest and most puzzling to explain. Additional investigation into the source of these vibrational intensities indicates that the conventional bond dipole picture is in fact overshadowed by surprisingly large changes in atomic charges upon symmetric and antisymmetric CH_2 stretch motion.

Specifically, from a usual first order Taylor series expansion of $\langle v'|\boldsymbol{\mu}(Q)|v''\rangle$, the $v' \leftarrow v''$ vibrational transition moment associated with normal mode Q and dipole moment operator $\boldsymbol{\mu}(Q) = \Sigma_l\, q_l\, \mathbf{r}_l$ can be readily shown to be

$$\langle v'|(\partial\boldsymbol{\mu}/\,\partial Q)|v''\rangle = \langle v'|\Sigma_l\,[\,q_l\,(\partial\mathbf{r}_l/\partial Q) + \mathbf{r}_l\,(\partial q_l/\partial Q)]|v''\rangle. \qquad (3.5)$$

The first term in parenthesis represents normal mode vector displacement of charge distributions on the atoms, i.e., the standard bond-dipole model. The second term

represents changes in the net molecular dipole due to vibrationally induced charge flow in/out of each atom, which we refer to as “charge sloshing”. Gaussian calculation results indicate that the hydrogen atom’s positive charge densities *decrease* upon the characteristic extension of the C-H bond in the CH_2 symmetric stretch. These decreases are accompanied by an *increase* in the carbon and halogen atom’s positive charge densities, from more negative to less negative values. This “charge-sloshing effect” results in net electron density flowing *synchronously with* the extension of the C-H bonds, leading to a transition dipole moment in the *opposite* direction from that of bond-dipole expectations. Indeed, for CH_2Cl, the magnitude of the transition dipole resulting from these “charge-sloshing” contributions is more than twice that of the regular bond-dipole contribution, thereby canceling and actually *reversing* the direction of the overall transition dipole.

For the antisymmetric CH_2 stretch, the two hydrogen atom charge densities *decrease and /increase* upon the C-H bond *stretch and compression*, respectively, with the carbon and halogen atom’s charge densities following the same trends as seen in the symmetric stretch. Once again, this “charge-sloshing” contribution is commensurate to that of the bond-dipole contribution and reverses the expected sign of the overall transition moment. However, whereas this reversal in CH_2F leaves sufficient intensity in the asymmetric stretch mode to permit observation in the slit jet, the behavior for CH_2Cl indicates a near perfect cancellation between bond dipole and “charge-sloshing” contributions and therefore an experimental reduction in asymmetric stretch intensity by > 20 fold. The important role of this competition is further confirmed by the out of plane dependence of these *ab initio* intensities, which

vanish identically in CH_2Cl near $\theta \approx 20$ degrees, in clear contrast with the systematic and more nearly uniform increase with θ noted for symmetric stretches in CH_2D and CH_2F. Interestingly, there are also indications of bond-dipole vs "charge sloshing" competition in the CH_2F asymmetric stretch mode, which from Figure 3.6 starts out weak at the planar configuration, growing much more rapidly with bending angle than any of the symmetric stretch bands as well as either symmetric or asymmetric stretch band of CH_2D. Indeed, this strong dependence of asymmetric stretch intensity on out of plane bend angle was used to confirm the existence of a non-planar equilibrium geometry in CH_2F, but with large amplitude bending motion and a zero point energy above the isomerization barrier.

By way of final confirmation of these charge sloshing effects in CH_2Cl and CH_2F radicals we have also performed similar *ab initio* calculations for the CH_2 symmetric and antisymmetric stretch intensity for bromomethyl radical, CH_2Br. These calculations are summarized in Figure 3.7 for CH_2D, CH_2Br, CH_2Cl, and CH_2F, i.e., in order of increase electron withdrawing nature of the substituent. As expected, the results indicate a rapid monotonic *increase* in symmetric stretch intensities with substituent electronegativity, but with a near vanishing of the asymmetric stretch intensities localized around CH_2Cl. This clear non-monotonic behavior provides additional support for a competition between bond-dipole and charge-sloshing effects in this radical series, as well as strongly suggests a sign change in the CH_2X asymmetric stretch vibrational transition moments between X = D, Br and X = F, with nearly perfect cancellation for X = Cl. While this physical

picture is presented as a possible simple explanation for our results, further theoretical and experimental work will clearly be needed to fully develop these concepts.

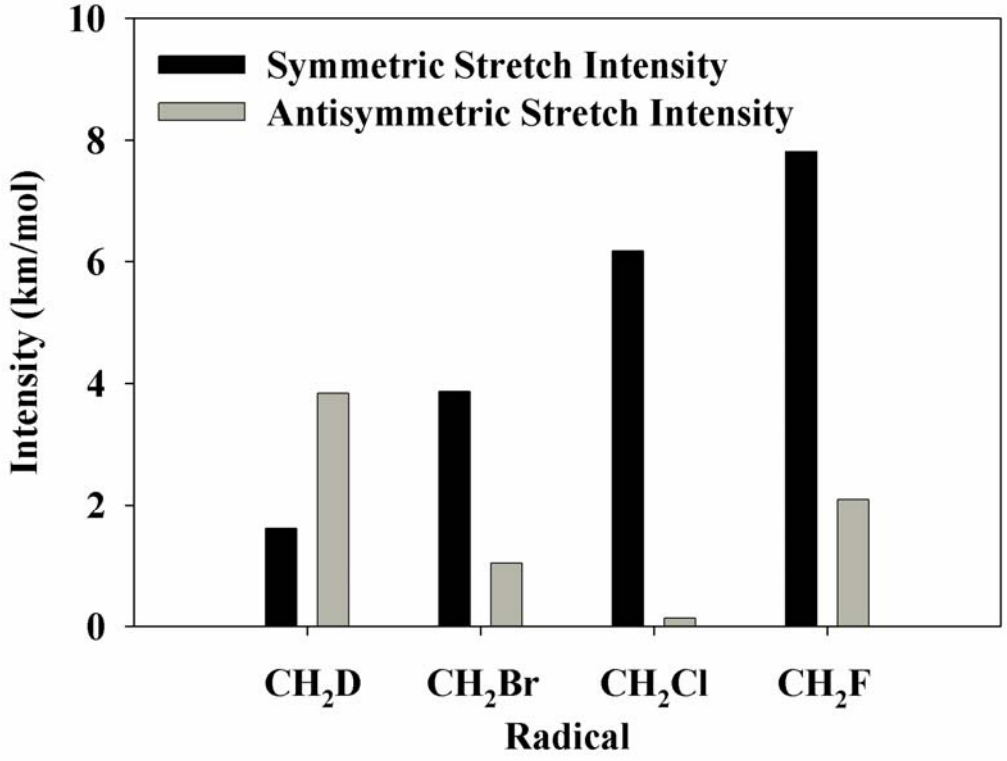

Figure 3.7 Comparison of symmetric (I_{sym}) and asymmetric (I_{asym}) stretch band intensities for CH_2D, CH_2Br, CH_2Cl, and CH_2F. Note the dramatic minimum in I_{asym} for CH_2Cl due to near cancellation of bond-dipole and "charge-sloshing" contributions, which becomes nonzero for either greater (CH_2F) or weaker (CH_2Br) electron withdrawing nature of the halogen substituent.

3.5 Summary and Conclusion

First high-resolution infrared spectra for jet-cooled $CH_2{}^{35}Cl$ and $CH_2{}^{37}Cl$ radicals have been obtained for the symmetric CH_2 stretching mode. Subsequent spectral assignment has enabled the determination of refined lower and upper state rotational constants, as well as fine structure parameters, from least-squares fits to the

sub-Doppler line shapes for individual transitions. Band centers for the $CH_2{}^{35}Cl$ and $CH_2{}^{37}Cl$ symmetric stretches are 3055.0760(2) and 3053.9781(1) cm^{-1}, respectively.

The spectral progressions for both isotopomers show characteristically strong R and P branches with a weaker Q branch, along with clear A-type band progressions from the $K_a = 0$ and $K_a = 1$ manifolds. There is also evidence of partially resolved structure on each peak due to intramolecular fine and hyperfine interactions. Integration of the band strengths for both isotopomers yields an intensity ratio of 2.6(2) that is also in rough agreement with the 3:1 ratio of their natural abundances. The rotational constants are consistent with a nearly planar structure but do not exclude substantial large-amplitude bending motion over a small barrier to planarity readily accessed with zero-point excitation. High level CCSD(T) calculations, extrapolated to a CBS limit, predict a slightly nonplanar structure ($\theta \approx 11^\circ$), with a vibrationally adiabatic 1D treatment of the bend coordinate yielding a fundamental anharmonic frequency (393 cm^{-1}), in excellent agreement with previous matrix studies ($\nu_{bend} \approx 400$ cm^{-1}) as well as theoretical predictions. We have also calculated higher vibrational energy levels (E_2, E_3, and E_4) to help stimulate further experimental confirmation of this bend potential.

The antisymmetric CH_2 stretch band is not observed for either isotopomer of CH_2Cl, despite high signal to noise on the corresponding symmetric stretch band. This concurs with theoretical calculations that indicate surprisingly weak intensities for the CH_2Cl antisymmetric stretch ($S_0 \approx 0.14$ km/mol) relative to the symmetric stretch ($S_0 \approx 6.15$ km/mol). These predictions contrast with predicted CH_2F symmetric and antisymmetric stretch intensities of $S_0 \approx 12$ km/mol and $S_0 \approx 6$ km/mol,

respectively, for which both bands were experimentally detected in previous studies. Both sets of results are in fundamental disagreement with simple bond dipole predictions of an $I_{sym}/I_{asym} \approx 1{:}3$ ratio for CH_2D, suggesting a significant impact of halogenation on the CH stretch intensity dynamics. These differences among intensities for CH_2Cl, CH_2F, and CH_2D suggest a simple physical model based on the competing and often dominant role of vibrationally mediated charge flow (i.e.,"charge-sloshing") between atoms. This analysis indicates that "charge-sloshing" contributions in CH_2F and CH_2Cl halomethyl radicals actually *reverse* the sign of the symmetric stretch transition moment away from conventional bond-dipole predictions. Furthermore, this competition is responsible for the cancellation of the asymmetric CH_2 stretch dipole moment in CH_2Cl, in good agreement with experiment. Finally, *ab initio* calculations for the series of CH_2D, CH_2Br, CH_2Cl and CH_2F radicals indicate an emerging and self consistent picture for "charge-sloshing" vs bond dipole contributions to symmetric and asymmetric stretch intensities as a function of substituent electronegativity.

Acknowledgment

This work has been supported by grants from the National Science Foundation, as well as from the Air Force Office of Scientific Research. T.H. would like to acknowledge postdoctoral support from the Alexander von Humboldt Foundation. M.D.S expresses his appreciation for partial sabbatical support from the National Science Foundation. We would also like to acknowledge many helpful discussions with Prof. Anne B. McCoy about IR vibrational band intensities.

References for Chapter 3

[1] M. Schwartz, L. R. Peebles, R. J. Berry, and P. Marshall, J. Chem. Phys. **118**, 557 (2003).

[2] M. J. Molina and L. T. Molina, Ann. Rev. Phys. Chem. **47**, 327 (1996).

[3] S. Davis, Ph.D. Thesis, University of Colorado (1999).

[4] M. E. Jacox, J. Phys. Chem. Ref. Data **32**, 1 (2003).

[5] J. S. Francisco and M. M. Maricq, in *Advances in Photochemistry* (Wiley, New York, 1995), Vol. 20, pp. 79.

[6] B. J. Finlayson-Pitts, *Chemistry of the Upper and Lower Atmosphere: Theory, Experiments, and Applications*. (Academic, New York, 1999).

[7] G. P. Brasseur, J. J. Orlando, and G. S. Tyndall, *Atmospheric Chemistry and Global Change*. (Oxford University Press, New York, 1999).

[8] J. G. Anderson, Ann. Rev. Phys. Chem. **38**, 489 (1987).

[9] E. S. Whitney, F. Dong, and D. J. Nesbitt, J. Chem. Phys. (in press).

[10] E. Hirota, Chem. Rev. **92**, 141 (1992).

[11] R. G. W. Norrish and G. Porter, Nature **164**, 658 (1949).

[12] G. Herzberg, *Molecular Spectra and Molecular Structure III. Electronic Spectra and Electronic Structure of Polyatomic Molecules*. (Van Nostrand, New York, 1966).

[13] A. M. Bass and H. P. Broida, *Formation and Trapping of Free Radicals*. (Academic Press, New York, 1960).

[14] B. C. Gilbert, M. J. Davies, and D. M. Murphy, *Electronic Paramagnetic Resonance*. (Royal Society of Chemistry, Cambridge, UK, 2002).

[15] J. S. Wells and K. M. Evenson, Rev. Sci. Instr. **41**, 226 (1970).

[16] K. M. Evenson, H. P. Broida, J. S. Wells, R. J. Mahler, and M. Mizushima, Phys. Rev. Lett. **21**, 1038 (1968).

[17] E. F. C. Byrd, D. Sherrill, and M. Head-Gordon, J. Phys. Chem. A **105**, 9736 (2001).

[18] R. W. Fessenden and R. H. Schuler, J. Chem. Phys. **39**, 2147 (1963).

[19] M. E. Jacox and D. E. Milligan, J. Chem. Phys. **53**, 2688 (1970).

[20] L. Andrews and D. W. Smith, J. Chem. Phys. **53**, 2956 (1970).

[21] D. Smith and L. Andrews, J. Chem. Phys. **55**, 5295 (1971).

[22] D. Smith and L. Andrews, J. Chem. Phys. **58**, 5222 (1973).

[23] J. P. Michaut and J. Roncin, Chem. Phys. Lett. **12**, 95 (1971).

[24] Y. Endo, S. Saito, and E. Hirota, Can. J. Phys. **62**, 1347 (1984).

[25] A. B. Potter, V. L. Dribinski, A. V. Demyanenko, and H. Reisler, Chem. Phys. Lett. **349**, 257 (2001).

[26] V. L. Dribinski, A. B. Potter, A. V. Demyanenko, and H. Reisler, J. Chem. Phys. **115**, 7474 (2001).

[27] S. V. Levchenko, A. V. Demyanenko, V. L. Dribinski, A. B. Potter, H. Reisler, and A. I. Krylov, J. Chem. Phys. **118**, 9233 (2003).

[28] P. B. Roussel, P. D. Lightfoot, F. Caralp, V. Catoire, R. Lesclaux, and W. Forst, J. Chem. Soc. Faraday Trans. **87**, 2367 (1991).

[29] Z. Zhou, L. Guo, C. Li, and H. Gao, J. Molec. Struct. **579**, 21 (2002).

[30] B. Wang, H. Hou, and Y. Gu, J. Phys. Chem. **103**, 2060 (1999).

[31] J. A. Seetula and I. R. Slagle, Chem. Phys. Lett. **277**, 381 (1997).

[32] S. Bailleux, P. Drean, M. Godon, Z. Zelinger, and C. Duan, Phys. Chem. Chem. Phys. **6**, 3049 (2004).

[33] Y. Endo, C. Hamada, S. Saito, and E. Hirota, J. Chem. Phys. **79**, 1605 (1983).

[34] J. W. Hudgens, C. S. Dulcey, G. R. Long, and D. J. Bogan, J. Chem. Phys. **87**, 4546 (1987).

[35] S. V. Levchenko and A. I. Krylov, J. Phys. Chem. A **106**, 5169 (2002).

[36] C. M. Lovejoy and D. J. Nesbitt, Rev. Sci. Instr. **68**, 807 (1987).

[37] E. Riedle, S. H. Ashworth, J. T. Farrell, Jr., and D. J. Nesbitt, Rev. Sci. Instr. **65**, 42 (1994).

[38] J. T. Farrell, Jr., S. Davis, and D. J. Nesbitt, J. Chem. Phys. **103**, 2395 (1995).

[39] F. Dong, D. Uy, S. Davis, M. Child, and D. J. Nesbitt, J. Chem. Phys. **122**, 224301 (2005).

[40] A. S. Pine, J. Opt. Soc. Am. **64**, 1683 (1974).

[41] A. S. Pine, J. Opt. Soc. Am. **66**, 97 (1976).

[42] F. Dong, personal communication (2005).

[43] J. K. G. Watson, in *Vibrational Spectra and Structure. A series of advances.*, edited by J. R. Durig (University of Southampton, Southampton, England), Vol. 6.

[44] E. Hirota, *High-Resolution Spectroscopy of Transient Molecules*. (Springer-Verlag, Berlin, 1985).

[45] S. V. Levchenko and A. I. Krylov, J. Phys. Chem. A **106**, 5169 (2002).

[46] H.-J. Werner, P. J. Knowles, M. Schutz, R. Lindh, P. Celani, T. Korona, G. Rauhut, F. R. Manby, R. D. Amos, A. Bernhardsson, A. Berning, D. L. Cooper, M. J. O. Deegan, A. J. Dobbyn, F. Eckert, C. Hampel, G. Hetzer, A. W. Lloyd, S. J. McNicholas, W. Meyer, M. E. Mura, A. Nicklab, P. Palmieri, R. Pitzer, U. Schumann, H. Stoll, A. J. Stone, R. Tarroni, and T. Thorsteinsoon, MOLPRO: a package of ab initio programs (2003).

[47] K. A. Peterson, D. E. Woon, and T. H. Dunning, Jr., J. Chem. Phys. **100**, 7410 (1994).

[48] D. J. Rush and K. B. Wiberg, J. Phys. Chem. A **101**, 3143 (1997).

[49] J. T. Hougen, P. R. Bunker, and J. W. C. Johns, J. Mol. Spec. **34**, 136 (1970).

CHAPTER 4

REACTIVE SCATTERING DYNAMICS IN ATOM + POLYATOM SYSTEMS: $F + C_2H_6 \rightarrow HF(v,J) + C_2H_5$

4.1 Introduction

The fundamental dynamics of chemical transformation reflect simple bond breaking and bond formation, the detailed understanding of which has been a long-standing, albeit elusive, target for the chemical physics community ever since Arrhenius' first development of a reaction-rate theory in 1889.[1] However, from a more modern chemical physics perspective, the rate constant does not always provide a sufficiently detailed molecular picture since it represents an average of microscopic reactant to product rate coefficients over all possible encounters, characterized by different relative velocities, orientations, vibrational and rotational quantum states, and impact parameters. An ongoing dual challenge of fundamental reaction dynamics has therefore been (i) to understand in detail how energy is distributed among nascent

rotational, translational, and vibrational degrees of freedom in product molecules as well as (ii) to provide simple physical pictures of the essential dynamics necessary to predict these distributions successfully. This latter issue is particularly important as the systems grow in complexity and degrees of freedom, from "atom + diatom" reactions to *polyatomic* reaction dynamics.

There have been several pioneering experimental and theoretical efforts to address these needs. The development of Fourier transform infrared spectroscopy (FTIR) "arrested-relaxation" chemiluminescence methods by Polanyi and coworkers proved ground breaking in providing first data on rovibrational excitation of products for a number of prototypical "A + BC" exothermic chemical reactions.[2-4] This work resulted in valuable theoretical concepts such as early/late barriers, which, in conjunction with detailed balance arguments, provided a relatively simple framework (i.e., "Polanyi rules")[5] for predicting nascent distributions as well as reagent vibrational vs. translational promotion over a chemical reaction barrier. Over a similar period, Herschbach,[6] Lee,[7] and coworkers evolved crossed-molecular beam methods into an even more powerful tool for study of reaction dynamics under rigorous single-collision conditions.[8] Although product fragment detection via time-of-flight energy loss[9] provides more limited resolution of internal quantum states than spectroscopic methods, the greater control of collision energy and access to differential-scattering information have clearly facilitated the most comprehensive tests of fundamental reaction dynamics.

This has been particularly true for elementary atom + diatom systems such as $H + H_2$,[10-14] $F + H_2$,[9,15-21] $Cl + H_2$,[22-25] and $O + H_2$[26-28] (and isotopic variants thereof),

which, augmented by sensitive laser-based laser-induced fluorescence (LIF),[29] resonance enhanced multiphoton ionization (REMPI)[30] or Rydberg detection of products,[26] have received an enormous amount of attention. The justification for a focus on three-atom systems is absolutely clear: these systems represent reactions for which it is possible to develop accurate *ab initio* potential energy surfaces[31] as well as perform full quantum mechanical scattering calculations.[32,33] In many cases, the calculations can be done without any dynamical approximations and sometimes with the inclusion of nonadiabatic dynamics on multiple electronic surfaces.[34] Although there are some outstanding questions yet to be resolved, particularly relating to issues of nonadiabatic reaction dynamics,[22,23,34] these synergistic experimental and theoretical treatments of three-atom dynamics have been remarkably productive and represent a major intellectual achievement of the chemical physics community.

Similarly detailed levels of comparisons between experiment and theory in more complicated systems such as atom + polyatom reactions have proven challenging. Much of the difficulty arises from theory, both at the *ab initio* level (i.e., reliable generation of potential energy surfaces) and dynamics level (i.e., converged methods for quantum reactive scattering) in high dimensionality. Indeed, the only numerically converged quantum-dynamics-scattering calculations for a system with more than three particles has been OH + H_2 by Zhang *et al*., a heroic achievement but nevertheless still a system with only one heavy (nonhydrogenic) atom.[35,36] Significant challenges are also present for crossed beam studies, for which conventional time-of-flight methods are typically unable to resolve internal state distributions of the products. This has provided further incentive for atom + polyatom crossed beam

studies with *spectroscopic-based* detection of products, as explored by Liu, Zare, Suits, Valentini and others.[37-41]

Counterbalancing these challenges, however, is the substantially richer world of reaction dynamics that opens up at the atom + polyatom level. Consider, for example, a simple atom abstraction in a highly exothermic atom + polyatom system. If the bond breaking event occurs on time scales *comparable* to intramolecular vibrational redistribution (IVR), one might anticipate substantial deposition of exothermicity into the polyatomic fragment, with less energy available for the diatomic product-state rovibrational distributions.[42] On the other hand, if IVR were *slow* compared to the reactive encounter, one might anticipate an essentially "sudden" Franck-Condon like process, with relatively little influence due to the potentially dense vibrational structure of the polyatomic fragment. Furthermore, kinetic energy release at the transition state might result in dynamical constraints that link translational, rotational, and vibrational degrees of freedom. More generally stated, one might therefore look for *bimolecular* reaction dynamics to reveal *dynamical correlations* at the quantum-state-resolved level, analogous to what has been elegantly demonstrated in the *unimolecular* photolysis literature.[43]

In this study, we use high-resolution infrared absorption spectroscopy to examine state-to-state reaction dynamics of an *atom + polyatom* system, the $F + C_2H_6 \rightarrow HF(v,J) + C_2H_5$ reaction, under single collision conditions in a crossed jet apparatus. This work builds upon previous crossed-beam–reactive-scattering studies of $F + CH_4/CD_4$ by Liu, Harper and others,[44-46] REMPI studies of Cl + alkanes of Zare, Orr-Ewing, Kitsopolous,[38,39,47,48] as well as extensive studies of $O(^3P)$ +

methane and nonmethane hydrocarbons by Suits, McKendrick and others.[29,41,49,50] The work also builds on early FTIR studies of the F + C_2H_6 system by Setser and coworkers, who report relative HF (v=1,2,3) vibrational energy distributions,[51] although under incompletely "arrested" rotational relaxation conditions.

The advantage of a high-resolution single-mode infrared laser source for studying reaction dynamics is twofold. First, the narrow ($\Delta\nu_{laser} \approx 0.0001$ cm^{-1}) linewidths translate into HF(v,J) product state detection with full rovibrational quantum state resolution, yet with peak sensitivities that permit operation at sufficiently low densities to maintain single collision conditions. Second, HF product velocity resolution is adequate to observe Doppler-broadened line shapes due to translational energy of the HF(v,J) product and thereby elucidate correlations between internal quantum state (i.e., rotation and vibration) and recoil away from the transition state. Most importantly, the availability of such quantum-state-resolved Dopplerimetry results hopefully provides the necessary stimulus for further *ab initio* development of high-quality potentials as well as novel dynamical pictures for atom + polyatom reactive scattering.

The remainder of this chapter is organized as follows. In Section 4.2, the experimental setup is briefly described. Section 4.3 describes the extraction of column integrated densities for nascent HF(v,J) distributions. Section 4.4 presents Doppler analysis of the experimental HF(v,J) absorption profiles, which reveal a striking linear correlation between translational energy release and rovibrational excitation of the ethyl radical fragment. This trend is interpreted in the context of a simple impulsive model, based on conservation of linear and angular momentum, that

nearly quantitatively reproduces the observed behavior and permits nascent HF(v,J) fluxes to be inferred via a simple model of the density-to-flux transformation. Concluding comments are summarized in Section 4.5.

4.2 Experiment

The infrared laser and crossed jet apparatus used for this experiment have been described previously.[52,53] Thus only details relevant to the current study will be briefly summarized. Single collision reaction dynamics are investigated in a 216 L vacuum chamber (60 cm × 60 cm × 60 cm), at the intersection region 5 cm downstream of two unskimmed, pulsed supersonic valves oriented at right angles. The reagent pulsed jet delivers a 10% ethane gas mixture in He diluent through a 500 μm pinhole orifice driven with a piezoelectric valve, with typical backing pressures of 200 Torr and 500 μs pulse duration. Fluorine radicals are efficiently formed from dissociative electron attachment in a F_2/He mixture though a modified solenoid valve body with a 5 mm × 0.3 mm slit orifice, with a pulse duration of ≈ 2 ms. The F atoms are formed in the F_2/He stagnation region by a fast discharge (600 volts, 100 mA peak current), timed to occur only at the center slice (500 μs) of the gas pulse. The discharge is confined upstream of the expansion orifice via bias polarity and interacts with the supersonic gas for ≈ 1 μs. The ethane and F atom jet speeds can be measured directly (in real time) by translating a small microphone inside the chamber and are found to be $1.38(6) \times 10^5$ cm/s and $5.49(37) \times 10^4$ cm/s, respectively. This is in good agreement with supersonic jet predictions based on the relevant gas mixtures and heat capacity ratios.[54]

The chamber is pumped with a 10-inch oil diffusion pump (5000 L/s) and backed by a 300 L/s roots-blower/mechanical-pump combination. With both pulses operating, the average pressure in the chamber is $< 1 \times 10^{-5}$ Torr, which translates into mean free collision paths of 300 cm, i.e., greatly in excess of the chamber dimensions. Peak densities in the intersection region are 1.0×10^{13} molecules/cm^3, corresponding to net reaction probabilities for F atom abstraction of < 1%, and sufficiently small to make the probability of rovibrationally inelastic collisions negligible on the transit time scale through the reaction zone. By way of supporting evidence, the nascent HF(v,J) populations are detected with *superthermal* velocity distributions, despite the expectation of collision cross sections for translational equilibration considerably larger than for rovibrational relaxation events. Indeed, high-resolution Doppler analysis of these nascent velocity distributions proves useful in characterizing translational energy-release dynamics of the reaction event, as will be discussed in Section 4.4.

The nascent HF(v,J) distributions are probed by direct absorption of a high-resolution color-center infrared laser source, pumped by the 647 nm red line of an actively amplitude-stabilized krypton ion laser. The infrared laser output is attenuated to <100 μW to avoid optical saturation of the nascent HF transitions and split into probe and reference beams. The probe beam is then multipassed (16 times) through the jet intersection region in a Herriott cell configuration to increase absorption sensitivity. Both probe and reference beams are focused onto matched InSb photovoltaic detectors (0.5 mm × 0.5 mm) with 1MHz transimpedance amplifiers. The resulting photocurrents monitored in dual beam subtraction mode with fast (10

MHz) active servo-loop electronics for reducing common-mode technical-amplitude noise to near shot-noise levels. Typical rms absorbance noise is ~1×10^{-4} absorbance units in a 10 kHz bandwidth, corresponding to a detection limit of $< 1.0 \times 10^{9}$ HF molecules/cm^3/quantum state.

These time-dependent nascent HF absorbance signals for a given absorption frequency rovibrational transition are captured with a transient digitizer on a pulse-by-pulse basis. Residual noncommon mode noise in the probe beam is further filtered by 100 μs gating and baseline subtraction before/after the pulse, yielding Doppler-resolved absorption signals as a function of laser frequency in ≈ 4 MHz increments. Column-integrated populations are obtained by directly integrating over these Doppler profiles and converting with known HF transition moments.[53,55] Relative frequency calibration is provided by simultaneously recording etalon transmission fringes [free spectral range (FSR) ≈ 150 MHz]. Absolute IR frequencies are determined with a traveling Michelson interferometer which facilitates tuning to a specific HF transition.[56]

4.3 Results and Analysis

4.3.1 *Data collection*

The energetics of the F + ethane reaction are summarized in Fig. 4.1. The reaction exothermicity is 37.8 (±1.0) kcal/mol,[57,58] which, in addition to an experimental collision energy of E_{com} = 3.2(6) kcal/mol, translates into a total energy release of 41(1) kcal/mol. The uncertainty in the collision energy is due primarily to angular divergence in the unskimmed jet geometry, but represents less than 2% of the

total energy release for such an exothermic reaction. Also indicated in Fig. 4.1 are the energetically allowed HF rovibrational states, which range up to HF(v = 3,J = 8) for stationery reactants and HF(v = 3,J≈12) for E_{com} = 3.2(6). Note that the HF(v = 4, J = 0) manifold is not accessible; thus any v = 4 ← 3 transitions must arise purely due to absorption from the lower state.

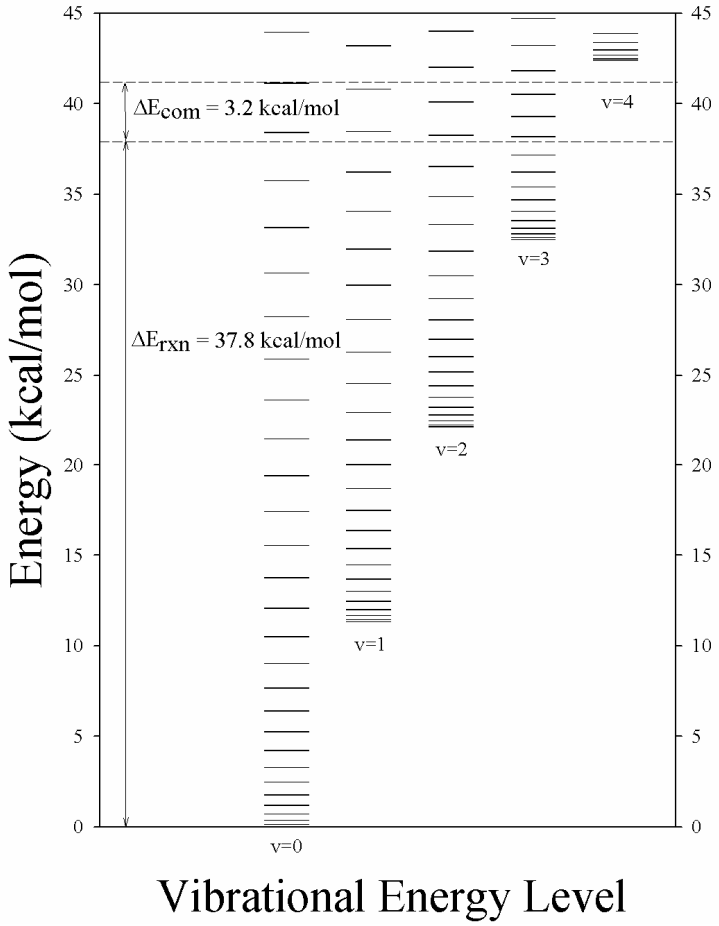

Figure 4.1 Energetics for the F + C_2H_6 reaction. The sum of reaction exothermicity (ΔH≈37.8) and center-of-mass collision energy (E_{com}≈3.2) yields 41(1) kcal/mol, allowing energetic access to product states as high as HF(v=3,J≈13).

High-resolution infrared-absorption Doppler profiles have been recorded for all product HF rovibrational transitions accessible within the 2.5 – 3.1 μm tuning range of the color-center laser. Each profile is scanned over a ≈ 0.1 cm^{-1} (3000 MHz) frequency interval with 3 MHz step size, yielding ≈1000 data points per profile. This scan range is 3–10 times larger than a typical HF product absorption at full-width half-maximum (FWHM) of 0.01 – 0.03 cm^{-1}. Data collection comprises approximately 75 *R* and *P* transitions from HF in v = 0, 1, 2, and 3 manifolds. Each transition is scanned multiple times (typically ≈ 6 – 9 fold) to improve statistics. Probing on both P and R branches provides a two-fold redundancy for transitions out of the same lower state, substantially overdetermining column-integrated populations inferred from subsequent least-squares analysis. The massive size of this data set requires acquisition over several months of experimentation; thus, all absorption intensities are measured with respect to a reference transition [HF(v = 4 ← 3) *R*(3)] to calibrate for long-term drift and day-to-day variations in the F-atom discharge efficiency. Additionally, for transitions from the lowest HF(v = 0) vibrational manifold, Doppler profiles are scanned with and without the ethane reagent pulse, to correct for trace background absorbance due to jet cooled HF (v = 0) impurities from the F atom source.

4.3.2 *Nascent column-integrated densities*

The data are treated in several ways. First of all, each Doppler profile is numerically integrated over all frequency steps to obtain quantum-state-resolved–column-integrated absorbances in absolute units, increasing typical signal-to-noise

ratio (S/N) of the raw profiles by a factor of 10. These integrated absorbances are then converted to column-integrated densities by the following expression[55]

$$\int A(v)dv = \frac{8\pi^3 v_0 |m|\mu^2}{3hc}\left[\frac{\int [HF(v'', J'')]dl}{(2J''+1)} - \frac{\int [HF(v', J')]dl}{(2J'+1)}\right], \qquad (4.1)$$

where μ is the v',J' $\leftarrow$ v,J transition dipole moment obtained from studies by Setser and Swalley,[55,59] m = -J, J + 1 for P and R branches, respectively, and v_0 is the rest transition frequency. As in any direct absorption measurement, these column-integrated densities reflect the *difference* between upper and lower state concentrations. Therefore, individual state populations are obtained by least-squares fitting the data set, with populations in energetically inaccessible states HF(v = 4 and higher) constrained to zero. This process involves sequential fitting of higher v states to obtain populations in lower states; thus uncertainty in the fitted values increases with decreasing v. Nevertheless, the high statistical quality of the data set permits unambiguous determination of nascent populations even in v = 0, which would be unobservable in conventional IR fluorescence measurements. The results for nascent quantum-state-resolved populations are summarized in Fig. 4.2. We will return to these populations later in Section 4.4 to correct for density to flux transformation and to interpret the resulting nascent fluxes.

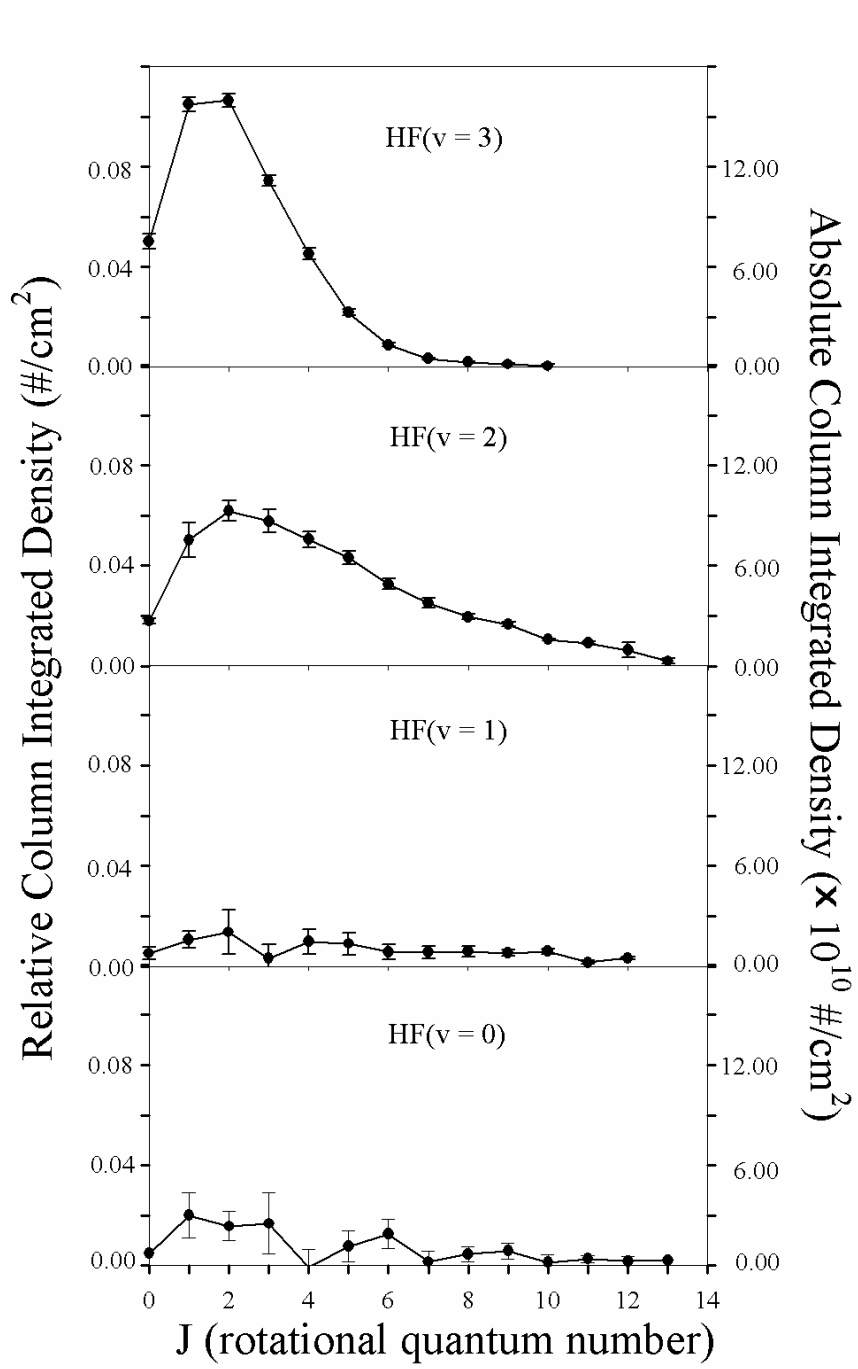

Figure 4.2 Nascent column-integrated densities for formation of HF(v,J) in specific rovibrational states from single collision F + C_2H_6 reactive events at E_{com} = 3.2(6) kcal/mol. Note the extraction of *absolute* densities that are feasible in direct IR laser studies due to measurement of *absolute* absorbances.

4.3.3 High-resolution infrared dopplerimetry

The high-resolution Doppler profiles themselves contain important additional information on the reaction dynamics. At a cursory level, inspection of the sample Doppler profiles in Fig. 4.3 reveals transitions with both absorption/stimulated emission character. All $v = 4 \leftarrow 3$ profiles reflect pure absorption signals, since the $v = 4$ vibrational manifold is energetically inaccessible. By way of contrast, all of the $v = 2 \leftarrow 1$ transitions are dominated by stimulated emission, reflecting a strongly inverted population with increasing vibrational quantum states. However, what occurs more often are *mixed*-stimulated-emission and "stimulated-absorption" Doppler profiles, as exemplified by the HF($v = 3 \leftarrow 2$) R(2) line in Fig. 4.3 and indicating a *velocity-dependent population inversion*. This inversion naturally arises from conservation of energy and reflects the smaller range of translational recoil speeds energetically accessible for the upper vs. lower probe states. It is worth noting that with the exception of the highest energy HF($v = 3$,J) levels, all these Doppler profiles are translationally "hot," which under non-single collisions would be rapidly thermalized by postreactive collision events. This observation provides additional confirmation for single collision conditions in the intersection region.

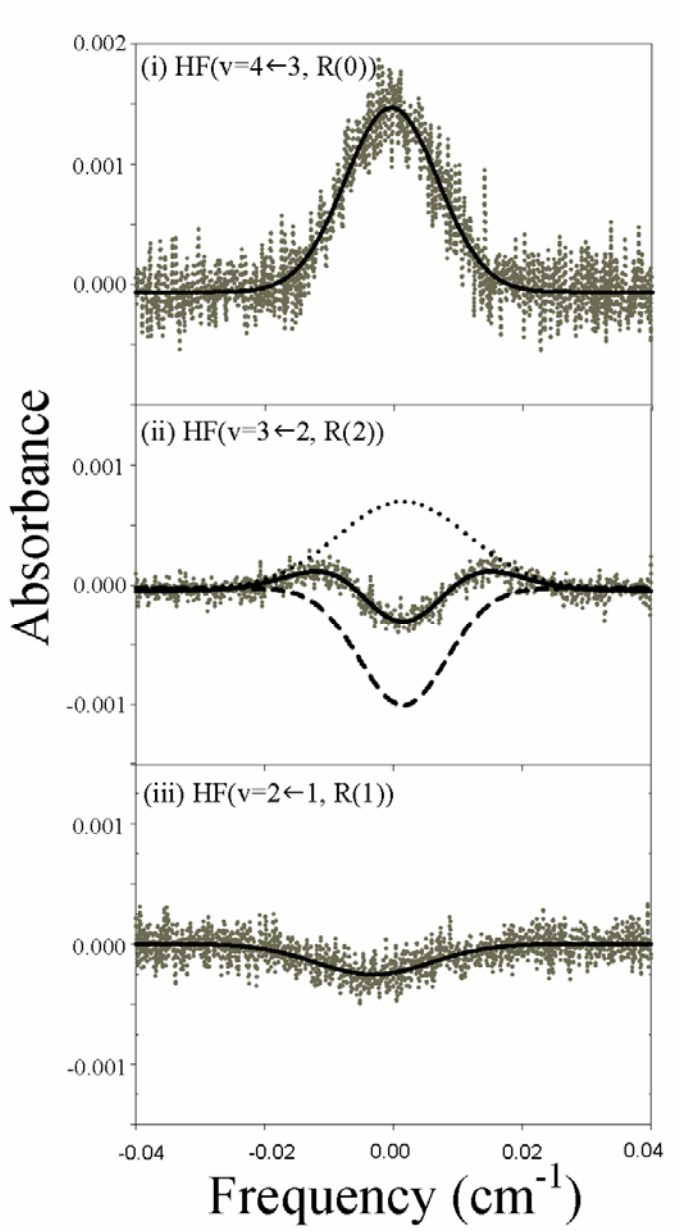

Figure 4.3 Sample high resolution profiles of HF(v,J) nascent product states from the F + C_2H_6 reaction, indicating strongly competing Doppler structures due to (i) stimulated absorption [HF($v = 4 \leftarrow 3$),$R(0)$], (ii) competition between stimulated emission and stimulated absorption [HF($v = 3 \leftarrow 2$),$R(2)$], and (iii) stimulated emission [HF($v = 2 \leftarrow 1$),$R(1)$]. Solid lines are least-squares fits to Gaussian line-shape functions, revealing velocity-dependent population-inversion effects dependent on upper- and lower-state translational energies.

Although the intrinsic probe laser resolution ($\Delta\nu \approx 0.0001$ cm^{-1}) translates into a velocity resolution along the laser axis of ≈10 m/s, detailed structure in this

distribution is effectively averaged due to finite aperture effects in an unskimmed beam. To extract average HF(v,J) product-recoil speeds and translational-energy components along the laser axis, therefore, each absorption or emission Doppler profile is fit to a Gaussian curve using nonlinear least-squares fitting methods. Parameter correlation restricts the transitions that can be least-squares fitted to predominantly pure absorption or emission profiles. Doppler widths from least-squares fits to the pure absorption and/or stimulated emission profiles are converted into expectation values of $\langle E_z \rangle = \langle p_z^2/2M \rangle$ along the laser axis (i.e., perpendicular to the plane of the reactant jets) via the standard Doppler expression[45]

$$< E_z > = \left\langle \frac{p_z^{\,2}}{2M} \right\rangle = \left(\frac{\Delta \nu_D c}{\nu_0} \right)^2 \frac{M}{16 \ln 2} \ , \qquad (4.2)$$

where $\Delta\nu_D$ is the Doppler width, ν_0 is the transition frequency, c is the speed of light, and M is the molecular mass. In essence, Eq. (4.2) represents the second moment of the HF momentum distribution projected along the laser probe z-axis.

These Doppler-width data reveal a remarkable trend (see Fig. 4.4). The total energy available to both HF and ethyl product fragments is $E_{total} = E_{com} + E_{rxn} \approx 41(1)$ kcal/mol. Since the internal rovibrational energy ($E^{HF}_{internal}$) of a given HF quantum state is known spectroscopically, the remaining energy available (E_{avail}) for either (i) translational recoil or (ii) rotation/vibration of the ethyl radical can be predicted from $E_{avail} = E_{total} - E^{HF}_{internal}$. The energies associated with the experimentally measured HF z-axis recoil distributions [i.e., Eq. (4.2)] are plotted in Fig. 4.4 as a function of E_{avail}. Despite the large number of degrees of freedom and potential complexity in such a reaction, the data reveal a surprisingly simple *linear* correlation between $\langle E_z \rangle =$

$\langle p_z^2/2M_{HF} \rangle$ and the available energy, with a slope of m ≈ 0.12(1). Given the size of this system, such an unambiguous correlation between HF internal and recoil energies strongly suggests the presence of dynamical constraints guiding the reaction dynamics. The origin of these constraints is further investigated in the context of a simple impulsive model described in the following section.

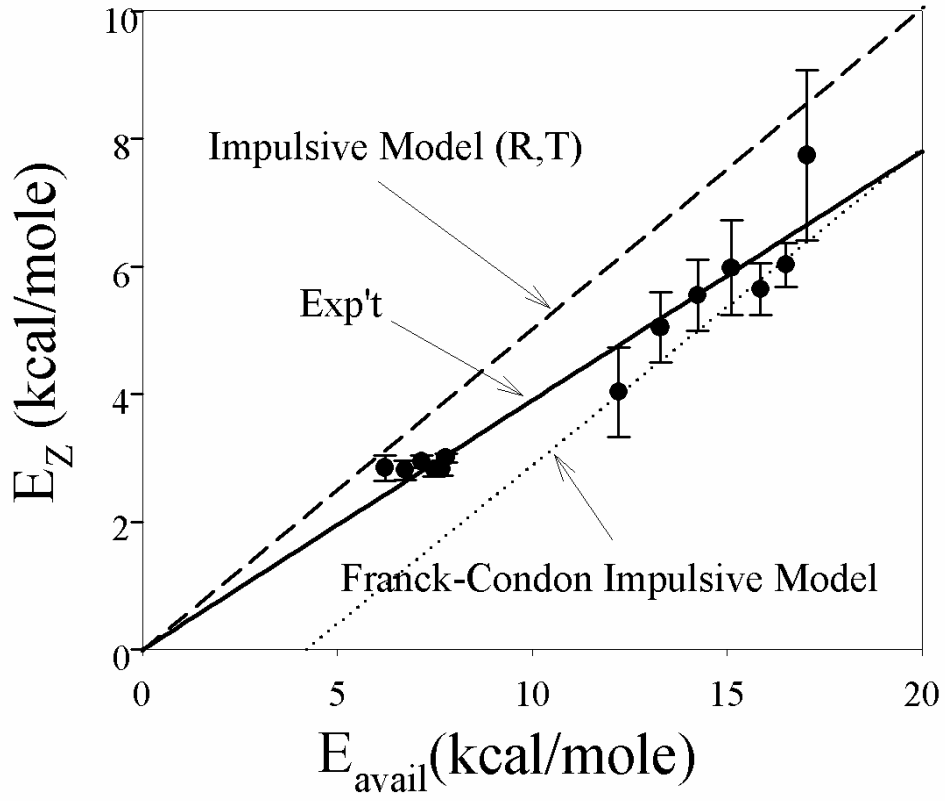

Figure 4.4 Recoil energy plots from high-resolution Dopplerimetry of single HF(v,J) quantum states. The data indicate a clear linear dependence between (i) $\langle E_{HF}(\text{trans}) \rangle \approx 3\langle E_z \rangle$ and (ii) $E_{avail} = E_{tot} - E_{HF}(v,J)$, i.e., the remaining energy available for both HF/ethyl translation and vibration/rotation/translational excitation of the ethyl radical. Note the excellent qualitative agreement with simple impulsive model predictions.

4.4 Discussion

4.4.1 *Impulsive model (rotation/translation)*

For any atom + diatom reaction system, energy flowing into the nascent diatomic product comes at the expense of translational recoil (neglecting electronic excitation of the atom). Thus, conservation of energy and momentum generates a natural *anticorrelation* between *internal* and *recoil* energy of the nascent diatomic product. However, it is not clear how such dynamical behavior might be altered in atom + polyatomic systems, specifically by additional rovibrational degrees of freedom in the nascent polyatomic fragment. Indeed, there have been several interesting models proposed for A + BC reactive scattering, with various forms of energy release and repulsive interaction between the recoiling fragments.[4,60] What makes the F + ethane case particularly intriguing is the presence of such a large lever arm in the ethyl fragment, which can significantly shift the dynamics of energy release from atom + diatom treatments. This poses an interesting and open question, toward which the linear correlation in Fig. 4.4 provides important initial clues.

As a limiting case, we consider a simple impulsive model for the energy partitioning in the F + C_2H_6 reaction, based purely on conservation of angular/linear momentum and total energy. In this model (illustrated in Fig. 4.5), the product ethyl fragment is treated as a rigid object with moment of inertia, I, that is rotationally excited by momentum recoil from the departing HF product. The final HF(v,J) state is well characterized by detection with the high-resolution IR laser. Thus, the total amount of available energy, E_{avail}, for distribution into translation (of ethyl and HF) and rovibration (of ethyl) is fixed by energy conservation:

$$E_{avail} = E_{trans}(HF) + E_{trans}(ethyl) + E_{rot}(ethyl) + E_{vib}(ethyl)\ . \qquad (4.3)$$

The fractional amount of energy that flows into ethyl vibrations is not immediately obvious. For a long lived reaction intermediate, as in an IVR model, one might anticipate a statistical sharing of the reaction exothermicity (ΔH) among all degrees of freedom. From a simple Franck-Condon picture, on the other hand, one would expect relatively modest excitation of the methylene CH_2 bending motion, with internal vibrational energies much less than ΔH. As will become clear below, the data are consistent with only relatively modest vibrational excitation of the polyatomic fragment. We will return to this issue later, but for now, temporarily neglect internal vibrational excitation of the ethyl radical, $E_{vib}(ethyl) \approx 0$.

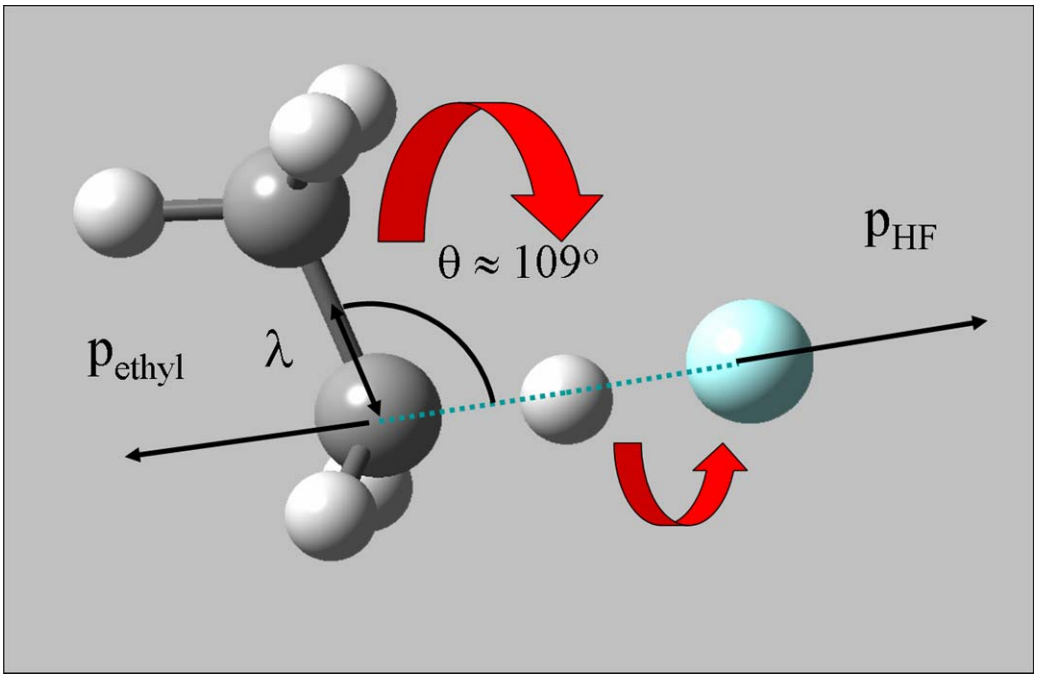

Figure 4.5 Cartoon depiction of the rotation/translation impulsive model, based purely on the conservation of linear and angular momentum. The angle (θ) and moment arm (λ) for delivering torque are calculated from CCSD(T) *ab initio* calculations of the transition state (see Table 4.1).

In the center-of-mass frame, the HF and ethyl recoil speeds are constrained by conservation of linear momentum, i.e.,

$$E_{trans}(HF)/E_{trans}(ethyl) = M_{ethyl}/M_{HF} . \quad (4.4)$$

For a known transition state geometry (specifically the angle θ between the newly breaking C-H bond and the principal A axis), we can therefore estimate the rotational excitation of the ethyl fragment to be

$$E_{rot}(ethyl) \approx L^2/2I \approx M_{ethyl}\, \lambda^2 \sin^2(\theta) E_{trans}(ethyl)/I , \quad (4.5)$$

where λ is the distance from the methylenic C atom and the ethyl radical center of mass. This provides a dynamical constraint between E_{rot} (ethyl) and E_{trans}(ethyl), yielding

$$E_{avail} \approx E_{trans}(HF)\, [1+M_{HF}/M_{ethyl} + M_{HF}\, \lambda^2 \sin^2(\theta)/I] \quad . \quad (4.6)$$

These Doppler profiles are recorded along the lab frame z-axis. However, the angular divergence in the crossed jet geometry already averages over a substantial range of incident/recoil angles in the center-of-mass frame. If we make the simplifying assumption that these momentum-recoil distributions are approximately equivalent along each of the three axes, $\langle E_x \rangle \approx \langle E_y \rangle \approx \langle E_z \rangle$, one obtains:

$$\langle E_z \rangle \approx E_{avail}/\{3(1+ M_{HF}/M_{ethyl} + M_{HF}\, \lambda^2 \sin^2(\theta)/I)\} . \quad (4.7)$$

Thus, the impulsive model predicts a simple linear correlation between $\langle E_z \rangle$ and E_{avail}, as experimentally observed.

We can test this prediction further by calculating the H-C-C bond angle θ, moment of inertia I, and distance to center of mass λ at the transition state geometry. This has been performed at a series of *ab initio* levels up to CCSD(T)/6-31G*,[61] yielding θ = 109.8, l = 0.825 Å, and I = 22.70 amu Å^2. These results predict $\langle E_z \rangle$ as a

function of E_{avail} in Eq. (4.7) to have a slope of $m \approx 0.15$. Given the simplicity of the model, this value is already respectably close to the experimental value of 0.12(1). We will explore reasons for the residual differences in Section 4.5 but stress here the key point that elementary conservation of linear and angular momentum (i) correctly predicts a *linear scaling* of HF recoil energy with E_{avail}, and (ii) accounts for ≈ 80% of the observed correlation. Given the potential for dynamical complexity that one might anticipate in such atom + polyatom systems, this is a remarkably simple and encouraging result.

4.4.2 *Density-to-flux transformation*

The analysis in Section 4.3.2 yields column-integrated *densities* for product formation into a given nascent HF(v,J) quantum state, whereas cross sections are defined in terms of product *fluxes*. To explicitly convert these densities into fluxes requires information on product velocities to account for distribution of quantum-state-resolved residence times in the laser probe region. Indeed, this is true for any nonflux-based detection method, e.g., direct absorption, LIF, REMPI, or IR chemiluminescence. For the $F + C_2H_6$ system, no quantum-state-resolved differential scattering information is available from previous work. Furthermore, although these IR methods do provide complete resolution of HF(v,J) product quantum states, the velocity distributions are sampled only along the laser multipass z-axis.

However, the preceding section indicates the presence of dynamical constraints that may help simplify such a density-to-flux analysis, specifically, the linear correlation between mean HF recoil in the lab frame and the available energy.

In the spirit of this impulsive model, therefore, we first make the simplest assumption consistent with the data and use it with the best-fit line to experiment (Fig. 4.4) to predict lab frame recoil-velocity distributions as a function of HF quantum state. This distribution is then used in conjunction with detailed Monte Carlo simulations of the crossed jet intersection geometry to predict quantum-state-resolved-averaged residence times, τ_{res}, and thus relative detection sensitivity $S(v,J) \propto \langle\tau_{res}\rangle$ for this state in the IR laser probe region.[20] One can then repeat this process with *different* assumed angular distributions and thereby explore the sensitivity of these results for a series of possible angular distributions.

4.4.3 *Nascent HF (v,J) populations*

The results of the Monte Carlo simulations, residence times, and density-to-flux transformation permit the conversion of experimental column-integrated densities (Fig. 4.2) into nascent quantum state populations. The results, normalized to unity by summing over all states, are reported in Fig. 4.6. Comparison of the three different scattering models (i.e., isotropic [$I(\theta) \propto$ constant], forward-backward [$I(\theta) \propto \sin^2(\theta)$], and side scattering [$I(\theta) \propto \cos^2(\theta)$]) shows only rather modest variations in the inferred populations. This insensitivity to assumed cross section reflects the fact that the translational recoil speeds substantially exceed the initial lab frame velocity, as well as additional blurring due to angular divergence in the crossed jet geometry. Indeed, the only significant differences are observed to occur in $v = 3$, reflecting the small amount of recoil energy remaining for the HF product in the highest vibrational manifold. This weak sensitivity to differential cross section suggests that the density-

to-flux transformation is quantitatively reliable. However, we note that the fundamental experimental measurements are the column-integrated densities in Fig. 4.2, for which error bars are reported.

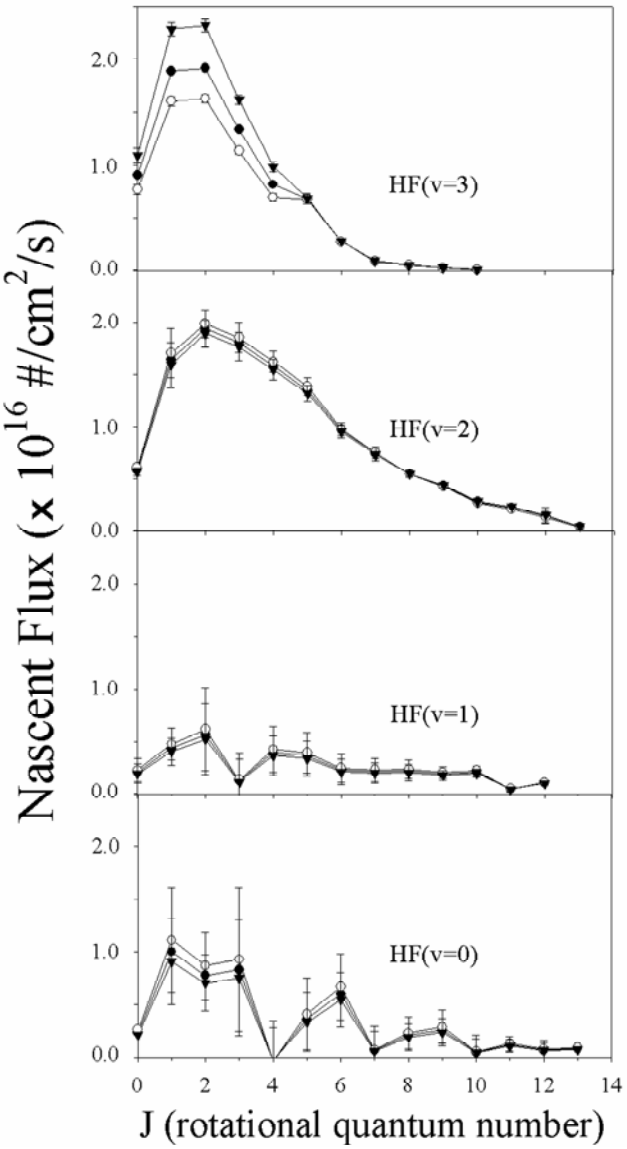

Figure 4.6 Nascent product-state fluxes (in relative units) based on Monte Carlo modeling of the density-to-flux transformation. Note the modest sensitivity of these fluxes to modeling of the differential cross sections.

The data illustrate several interesting points. First, when summed over J states, the relative vibrational populations are 0.28 to 0.43 to 0.12 to 0.16 for v = (3:2:1:0). This indicates a strong predominance of population funneling into the highest vibrational levels, consistent with the Polanyi rules[5] for maximal deposition of energy into the newly formed H-F bond. Interestingly, there also appears to be a small, but substantial, nascent population in the v = 0 manifold, which would have previously been invisible to IR chemiluminescence methods. Second, the rotational populations in all vibrational manifolds extend to rather high values of J. This is qualitatively consistent with a noncollinear transition-state geometry, as is indeed obtained from CCSD(T) transition-state calculations used in the impulsive model. Third, though quite hot, the rotational populations are relatively thermal in nature. Indeed, the most populated HF(v = 2) and HF(v = 3) manifolds are reasonably well fit to a Boltzmann distribution, with rotational "temperatures" of T_{rot} = 1307 K and 496 K, respectively. This reflects a considerably cooler distribution for the more vibrationally populated level, which is qualitatively consistent with less energy available for rotational excitation. Of dynamical interest, however, these rotational distributions drop to zero considerably *below* the energetically accessible limits in the v = 2 and v = 3 manifolds of HF. This differs qualitatively from previous studies of F + H_2 and F + HD reaction dynamics and signals the presence of additional energy-loss pathways into the polyatomic ethyl radical.[20,53] This interpretation is consistent with the presence of additional dynamical constraints in addition to conservation of energy, specifically recoil *rotational excitation* of the ethyl fragment.

Previous work by Bogan and Setser on the F + C_2H_6 system employed "arrested relaxation" FTIR chemiluminescence measurements in a continuous flow reactor with much higher densities and residence times in the detection region.[51] Although this earlier work focused only on nascent *vibrational* populations as sufficiently "arrested," the basic trends in the rotational distributions are in fact similar to what we find. This comparison is highlighted in Fig. 4.7 for the maximally populated HF(v = 2) manifold; there is very good qualitative agreement with the collision-free results, though clearly somewhat cooler due to partially unarrested rotational relaxation prior to the detection event. Similar partial relaxation has also been noted in comparisons between crossed-jet and arrested-relaxation studies of F + CH_4, presumably also caused by collisional effects in the flow reactor.[44,45,62] The more appropriate comparison, however, is obtained by summing over these rotational distributions to yield nascent vibrational-population ratios of 0.338(4) : 0.520(12) : 0.142(1) for v_{HF} = 3:2:1. These vibrational ratios are in excellent agreement with the Bogan and Setser values of 0.33 : 0.53 : 0.14, confirming that vibrational relaxation was indeed arrested in the early flow-reactor studies.

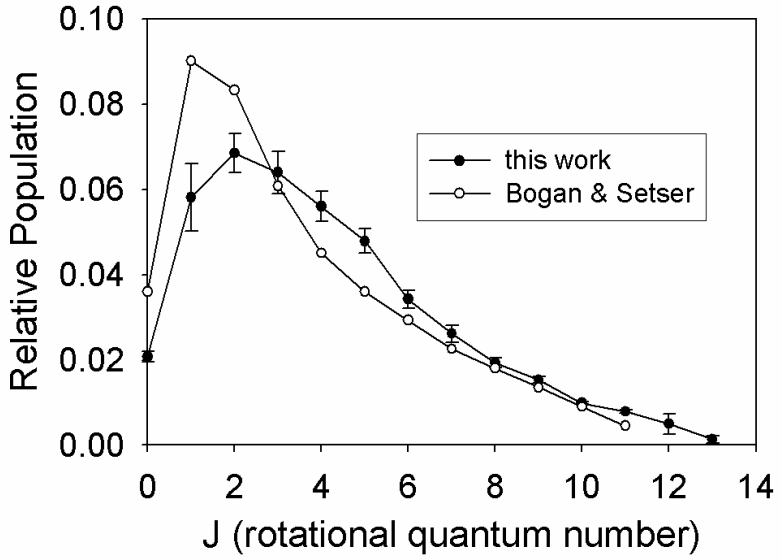

Figure 4.7 Comparison of current HF($v = 2,J$) nascent fluxes with previous vibrational "arrested relaxation" studies of Bogan and Setser. Agreement is generally quite good, though evidence for partial rotational relaxation is present. However, the nascent vibrational populations from these previous studies, summed over final rotational states, are in excellent agreement with the current collision-free results.

An important advantage of direct absorption IR laser methods is that it permits detection of *all* rovibrational levels, including the nonemitting HF(v=0) manifold. If we include v=0 populations in the normalization, the nascent vibrational ratios become 0.283(4) : 0.434(12) : 0.119(1) : 0.165(36). It is worth noting the substantially *non-zero* nascent population in the $v_{HF} = 0$ manifold, indeed, appreciably *more* (40%) than is formed in HF(v = 1). This is dynamically interesting, since populations in the lowest HF(v = 0) manifolds have been inaccessible in the pioneering chemiluminescence studies of Polanyi, Sloan, Setser and others,[51,63] but were inferred to be nearly zero by surprisal-plot analysis and extrapolation from the higher-vibrational manifolds. In fact, the present data on F + C_2H_6 indicate that this is

not always a valid assumption. Furthermore, the nonmonotonic behavior at low v_{HF} may suggest the presence of "bimodal" reaction dynamics. Specifically, the increase of HF(v) product with low vibrational excitation may be signaling reactive events that occur on time scales long enough to permit vibrational energy flow from the F-H-C transition-state region into the "bath" manifold of vibrational levels supported by the ethyl fragment. If so, this would indicate an intriguing duality of dynamical processes, primarily dominated by (i) impulsive energy release localized in the transition-state region, but nevertheless augmented by (ii) *IVR energy flow out* of the highly energized F-H-C moiety and into the polyatomic fragment, on a time scale that is slow with respect to the bond-breaking and bond-making events.

4.4.4 *Dynamic Franck-Condon impulsive model*

As a final comment, we return to the impulsive model and offer some refinements. Based on rigid translational/rotational excitation of ethyl radical, this model successfully accounts for the observed linear correlation between E_{trans}(HF) and E_{avail} as well as most (≈ 80%), but not all, of the Doppler recoil energy. In principle, the residual (≈ 20%) deviations could be due to strongly anisotropic differential scattering of the HF product in the forward/backward direction, and thus a systematic undersampling of the lab frame recoil kinetic energies. However, based on the range of collision angles sampled in the crossed jet geometry and the modest dependence of detection sensitivity on scattering distributions (see Fig. 4.6), this does not appear likely to account for all of the residual deviations. A simpler explanation

could be that they are due to vibrational excitation successfully imparted to the ethyl radical, which was explicitly neglected in our zeroth order treatment.

A plausible correction to the impulsive model would be to assume that the bond-breaking event occurs much more rapidly than the methylene group can vibrationally relax to its equilibrium geometry. This would result in a Franck-Condon excitation of the CH_2 group and, from the simplest perspective, predict a constant energy offset due to sequestering of this relaxation energy in the methylene moiety. Indeed, such a model has been successfully invoked by Suits *et al*. in studies of O atom abstraction of H atoms from hydrocarbons.[41] An alternative picture would also allow for additional excitation of the torsional modes of ethyl radical, though this would seem unlikely based on the C_s symmetry of the translational state geometry. In any event, the relevant relaxation energy can be predicted from high level *ab initio* calculations performed at the F--H--CH_2CH_3 transition state, abruptly removing the HF to infinity and then using gradient-following methods to relax the ethyl radical to its global minimum. *Ab initio* results obtained at a series of method/basis set sizes are summarized in Table 4.1, with CCSD(T)/6-31G* representing the highest level of treatment. The calculations indicate an increasing trend in relaxation energies, with the highest level predictions of ≈ 4.24 kcal/mol. This is appreciably larger than comparable relaxation values (≈ 2.45 kcal/mol) obtained for the F-H-CH_3 system, presumably due to a softer CH_2 bending coordinate in the resulting methyl vs. ethyl radical.

Table 4.1. *Ab initio* results for H-C-C bond angle θ, moment of inertia I, and distance to center-of-mass λ at transition state geometry.

Method	Basis Set	λ (Å)	θ (degrees)	I (amu Å^2)	E $_{relax}$ (kcal/mole)
CCD	6-31G*	0.8222	109.142	23.931	3.815
CCSD	6-31G*	0.8233	109.501	23.935	4.086
CCSD(T)	6-31G*	0.8253	109.827	23.997	4.242

The effect of Franck-Condon "sequestering" of energy in CH_2 would be to limit the energy available for vibration/rotation, and thereby shift simple impulsive model predictions to a higher energy by ≈ 4.24 kcal/mol. Such an additional plot is shown with a dashed line in Fig. 4.4, which proves to be in reasonable agreement with experiment, particularly at the higher values of E_{avail}. Larger discrepancies exist for the *lowest* E_{avail} [i.e., *highest* HF(v,J) states], which could reflect the finite angular spread of lab frame collision velocities for the crossed jet configuration. However, the descrepancies could also indicate a transition back to a less "sudden" picture of CH bond breaking, with adiabatic relaxation of the CH_2 group made possible in the limit of slow HF recoil. Further confirmation of this elementary treatment and the physical origin of excess population in the HF(v = 0) manifold would be extremely interesting to explore with *ab initio* direct-dynamics calculations, which are currently underway.[64] In any event, the current state-resolved F + ethane data already provide strong support for a simple "impulsive model" based on (i) recoil coupling of rotation/translation fragment energies, suitably modified by (ii) Franck-Condon vibrational excitation in the relaxing moiety.

4.6 Summary and Conclusion

State-to-state scattering dynamics of $F + C_2H_6 \rightarrow HF(v,J) + C_2H_5$ under single collision conditions have been studied via detection of nascent rovibrationally resolved HF(v,J) product states with high-resolution IR laser-absorption methods. Doppler absorption profiles have been observed for HF(v,J) transitions in all energetically accessible vibrational manifolds and analyzed to yield nascent column-integrated densities as a function of rovibrational quantum state. Corrected for the density-to-flux transformation, the trends in these data indicate a high-efficiency vibrational excitation accompanied by relatively modest rotational excitation of the newly formed bond. This is consistent with Polanyi rules[5] for early-barrier dynamics in atom + diatom systems and in good agreement with high-level *ab initio* calculations of a slightly noncollinear F-H-C transition state. Vibrational[51,65] populations summed over rotational levels are in excellent agreement with early FTIR flow-cell reactor studies, though elimination of rotational relaxation is evident under single-collision conditions in the crossed jet. Additionally, the IR laser experiment exploits the unique ability of direct absorption methods to determine nascent populations in the *non-emitting* HF(v = 0) manifold, which for the $F + C_2H_6$ system prove to be substantially more populated than predicted from surprisal analysis trends in the previously studied HF(v = 1,2,3) manifolds.[44] Indeed, the significant population of vibrationally cold HF (v = 0) might signal the presence of a (minor) parallel dynamical pathway involving IVR energy flow from HF into the ethyl fragment on the time scale of the chemical reaction. The prospects for such intermolecular

dynamics might be further investigated with analytical models for IVR mode coupling from a F-H-C transition state down along the alkane chain as well as from *ab initio* direct dynamics calculations.[64]

Of special dynamical interest, analysis of the high-resolution Doppler profiles reveals a striking correlation between (i) HF recoil velocities and (ii) the remaining energy for distribution into translation and rovibrational degrees of freedom for the ethyl fragment. This correlation motivates analysis via a simple "impulsive model" based on sudden energy release from a transition-state geometry and invoking conservation of energy, linear momentum, and angular momentum. This model successfully predicts the experimentally observed correlation between HF recoil and excess energy, and accounts for the majority (≈ 80%) of the ethyl fragment excitation in the form of translational recoil and end-over-end tumbling perpendicular to the C-C bond. The remaining ethyl internal energy predicted from this experimental correlation is consistent with a Franck-Condon-like excitation of the CH_2 moiety, due to a ≈ 4.5 kcal/mol relaxation of the spectator methyl group into a sp^2-hybridized methylene radical center. More work, both experimental and theoretical, will clearly be required to test if such a simple model will prove generally applicable in exothermic atom + polyatom reaction systems. However, this would appear a promising zeroth order paradigm with which to approach the potential complexity of reaction dynamics beyond A + BC.

References for Chapter 4

[1] S. A. Arrhenius, Z. Phys. Chem. **4**, 226 (1889).

[2] D. H. Maylotte, J. C. Polanyi, and K. B. Woodall, J. Chem. Phys. **57**, 1547 (1972).

[3] P. D. Pacey and J. C. Polanyi, J. Appl. Opt. **10**, 1725 (1971).

[4] J. C. Polanyi, Faraday Discuss. **55**, 389 (1973).

[5] J. C. Polanyi and W. H. Wong, J. Chem. Phys. **51**, 1439 (1969).

[6] D. R. Herschbach, Angew. Chem. Int. Engl. Ed. **26**, 1223 (1987).

[7] Y. T. Lee, Angew. Chem. Int. Engl. Ed. **26**, 939 (1987).

[8] J. C. Polanyi, Science **236**, 680 (1987).

[9] M. Faubel, S. Schlemmer, F. Sondermann, and J. P. Toennies, J. Chem. Phys. **94**, 4676 (1991).

[10] E. Wrede, L. Schneider, K. H. Welge, F. J. Aoiz, L. Banares, J. F. Castillo, B. Martinez-Haya, and V. J. Herrero, J. Chem. Phys. **110**, 9971 (1999).

[11] I. Last, M. Gilibert, and M. Baer, J. Chem. Phys. **107**, 1451 (1997).

[12] S. D. Chao and R. T. Skodje, Chem. Phys. Lett. **336**, 364 (2001).

[13] F. Fernandez-Alonso, B. D. Bean, J. D. Ayers, A. E. Pomerantz, R. N. Zare, L. Banares, and F. J. Aoiz, Angew. Chem. Int. Eng. Ed. **39**, 2748 (2000).

[14] D. G. Truhlar and R. E. Wyatt, Ann. Rev. Phys. Chem. **27**, 1 (1976).

[15] D. M. Neumark, A. M. Wodtke, G. N. Robinson, C. C. Hayden, and Y. T. Lee, J. Chem. Phys. **82**, 3045 (1985).

[16] D. M. Neumark, A. M. Wodtke, G. N. Robinson, C. C. Hayden, K. Shobatake, R. K. Sparks, T. P. Schafer, and Y. T. Lee, J. Chem. Phys. **82**, 3067 (1985).

[17] K. Stark and H.-J. Werner, J. Chem. Phys. **104**, 6515 (1996).

[18] D. E. Manolopoulos, J. Chem. Soc., Faraday Trans. **93**, 673 (1997).

[19] F. Dong, S.-H. Lee, and K. Liu, J. Chem. Phys. **113**, 3633 (2000).

[20] W. W. Harper, S. A. Nizkorodov, and D. J. Nesbitt, J. Chem. Phys. **116**, 5622 (2002).

[21] S.-H. Lee, F. Dong, and K. P. Liu, J. Chem. Phys. **116**, 7839 (2002).

[22] S.-H. Lee, L.-H. Lai, K. Liu, and H. Chang, J. Chem. Phys. **110**, 8229 (1999).

[23] S.-H. Lee and K. Liu, J. Chem. Phys. **111**, 6253 (1999).

[24] M. Alagia, N. Balucani, L. Cartechini, P. Casavecchia, E. H. vanKleef, G. G. Volpi, F. J. Aoiz, L. Banares, D. W. Schwenke, T. C. Allison, S. L. Mielke, and D. G. Truhlar, Science **273**, 1519 (1996).

[25] S. A. Kandel, A. J. Alexander, Z. H. Kim, R. N. Zare, F. J. Aoiz, L. Banares, J. F. Castillo, and V. S. Rabanos, J. Chem. Phys. **112**, 670 (2000).

[26] X. Liu, J. J. Lin, S. Harich, G. C. Schatz, and X. Yang, Science **289**, 1536 (2000).

[27] G. C. Light, J. Chem. Phys. **68**, 2831 (1978).

[28] D. C. Robie, S. Arepalli, N. Presser, T. Kitsopoulos, and R. J. Gordon, Chem. Phys. Lett. **134**, 579 (1987).

[29] G. M. Sweeney, A. Watson, and K. G. McKendrick, J. Chem. Phys. **106**, 9172 (1997).

[30] D. A. V. Kliner, D. E. Adelman, and R. N. Zare, J. Chem. Phys. **94**, 1069 (1991).

[31] F. J. Aoiz, L. Banares, B. Martinez-Haya, J. F. Castillo, D. E. Manolopoulos, K. Stark, and H.-J. Werner, J. Phys. Chem. **101**, 6403 (1997).

[32] M. H. Alexander, D. E. Manolopoulos, and H.-J. Werner, J. Chem. Phys. **113**, 11084 (2000).

[33] S. D. Chao, S. A. Harich, D. X. Dai, C. W. Chia, X. Yang, and R. T. Skodje, J. Chem. Phys. **117**, 8341 (2002).

[34] M. H. Alexander, G. Capecchi, and H.-J. Werner, Science **296**, 715 (2002).

[35] D. H. Zhang and S. Y. Lee, J. Chem. Phys. **110**, 4435 (1999).

[36] D. H. Zhang and J. Z. H. Zhang, J. Chem. Phys. **101**, 1146 (1994).

[37] K. Liu, Ann. Rev. Phys. Chem. **52**, 139 (2001).

[38] W. R. Simpson, A. J. Orr-Ewing, and R. N. Zare, Chem. Phys. Lett. **212**, 163 (1993).

[39] W. R. Simpson, T. P. Rakitzis, S. A. Kandel, T. Lev-On, and R. N. Zare, J. Phys. Chem. **100**, 7938 (1996).

[40] J. J. Valentini, Ann. Rev. Phys. Chem. **52**, 15 (2001).

[41] X. Liu, R. L. Gross, G. E. Hall, J. T. Muckerman, and A. G. Suits, J. Chem. Phys. **117**, 7947 (2002).

[42] D. J. Nesbitt and R. W. Field, J. Phys. Chem. **100**, 12735 (1996).

[43] G. G. Balint-Kurti, J. Chem. Phys. **84**, 4443 (1986).

[44] W. W. Harper, S. A. Nizkorodov, and D. J. Nesbitt, J. Chem. Phys. **113**, 3670 (2000).

[45] W. W. Harper, S. A. Nizkorodov, and D. J. Nesbitt, Chem. Phys. Lett. **335**, 381 (2001).

[46] J. J. Lin, J. Zhou, W. Shiu, and K. Liu, Science **300**, 966 (2003).

[47] S. A. Kandel, T. P. Rakitzis, T. Lev-On, and R. N. Zare, J. Phys. Chem. **102** (1998).

[48] M. J. Bass, M. Brouard, C. Vallance, T. N. Kitsopoulos, P. C. Samartzis, and R. L. Toomes, J. Chem. Phys. **119**, 7168 (2003).

[49] J. J. Lin, J. Shu, Y. T. Lee, and X. Yang, J. Chem. Phys. **113**, 5287 (2000).

[50] J. Shu, J. J. Lin, Y. T. Lee, and X. Yang, J. Chem. Phys. **115**, 849 (2001).

[51] D. J. Bogan and D. W. Setser, J. Chem. Phys. **64**, 586 (1976).

[52] A. Schiffman, W. B. Chapman, and D. J. Nesbitt, J. Phys. Chem. **100**, 3402 (1996).

[53] W. B. Chapman, B. W. Blackmon, S. Nizkorodov, and D. J. Nesbitt, J. Chem. Phys. **109**, 9306 (1998).

[54] D. R. Miller, in *Atomic and Molecular Beam Methods*, edited by G. Scoles (Oxford University Press, Inc., New York, 1988), Vol. 1.

[55] E. Arunan, D. W. Setser, and J. F. Ogilvie, J. Chem. Phys. **97**, 1734 (1992).

[56] J. L. Hall, Appl. Phys. Lett. **29**, 367 (1976).

[57] K. P. Hubert and G. Herzberg, *Molecular Spectra and Molecular Structure Constants of Diatomic Molecules*. (Van Nostrand Reinhold, New York, 1979).

[58] R. R. Baldwin, G. R. Drewery, and R. W. Walker, J. Chem. Soc., Faraday Trans. **80**, 2827 (1984).

[59] W. T. Zemke, W. C. Swalley, S. R. Langhoff, G. L. Valderrama, and M. J. Berry, J. Chem. Phys. **95**, 7846 (1991).

[60] P. J. Kuntz, Mak, M. H., and Polanyi, J. C., J. Chem. Phys. **50**, 4623 (1969).

[61] M. J. Frisch, G. W. Trucks, and H. B. Schlegel, Computer Program Gaussian98 (Gaussian, Inc., Pittsburgh, 1999).

[62] M. Maneshkarimi and H. Heydtmann, Chem. Phys. Lett. **234**, 182 (1995).

[63] R. D. H. Brown, D. J. Douglas, and J. C. Polanyi, J. Chem. Soc., Faraday Trans. **75**, 422 (1979).

[64] A. B. McCoy and D. J. Nesbitt, (in progress).

[65] D. J. Smith, D. W. Setser, K. C. Kim, and D. J. Bogan, J. Phys. Chem. **81**, 898 (1977).

BIBLIOGRAPHY

M. Alagia, N. Balucani, L. Cartechini, P. Casavecchia, E. H. vanKleef, G. G. Volpi, F. J. Aoiz, L. Banares, D. W. Schwenke, T. C. Allison, S. L. Mielke, and D. G. Truhlar, Science **273**, 1519 (1996).

M. H. Alexander, D. E. Manolopoulos, and H.-J. Werner, J. Chem. Phys. **113**, 11084 (2000).

M. H. Alexander, G. Capecchi, and H.-J. Werner, Science **296**, 715 (2002).

J. G. Anderson, Ann. Rev. Phys. Chem. **38**, 489 (1987).

L. Andrews and D. W. Smith, J. Chem. Phys. **53**, 2956 (1970).

F. J. Aoiz, L. Banares, B. Martinez-Haya, J. F. Castillo, D. E. Manolopoulos, K. Stark, and H.-J. Werner, J. Phys. Chem. **101**, 6403 (1997).

S. A. Arrhenius, Z. Phys. Chem. **4**, 226 (1889).

E. Arunan, D. W. Setser, and J. F. Ogilvie, J. Chem. Phys. **97**, 1734 (1992).

S. Bailleux, P. Drean, M. Godon, Z. Zelinger, and C. Duan, Phys. Chem. Chem. Phys. **6**, 3049 (2004).

R. R. Baldwin, G. R. Drewery, and R. W. Walker, J. Chem. Soc., Faraday Trans. **80**, 2827 (1984).

G. G. Balint-Kurti, J. Chem. Phys. **84**, 4443 (1986).

A. M. Bass and H. P. Broida, *Formation and Trapping of Free Radicals*. (Academic Press, New York, 1960).

M. J. Bass, M. Brouard, C. Vallance, T. N. Kitsopoulos, P. C. Samartzis, and R. L. Toomes, J. Chem. Phys. **119**, 7168 (2003).

T. Beiderhase, W. Hack, K. Hoyermann, and M. Olzmann, Z. Phys. Chem. **214**, 625 (2000).

D. J. Bogan and D. W. Setser, J. Chem. Phys. **64**, 586 (1976).

G. P. Brasseur, J. J. Orlando, and G. S. Tyndall, *Atmospheric Chemistry and Global Change*. (Oxford University Press, New York, 1999).

R. D. H. Brown, D. J. Douglas, and J. C. Polanyi, J. Chem. Soc., Faraday Trans. **75**, 422 (1979).

E. F. C. Byrd, D. Sherrill, and M. Head-Gordon, J. Phys. Chem. A **105**, 9736 (2001).

G. A. Carlson and G. C. Pimentel, J. Chem. Phys. **44**, 4053 (1966).

S. D. Chao and R. T. Skodje, Chem. Phys. Lett. **336**, 364 (2001).

S. D. Chao, S. A. Harich, D. X. Dai, C. W. Chia, X. Yang, and R. T. Skodje, J. Chem. Phys. **117**, 8341 (2002).

W. B. Chapman, B. W. Blackmon, S. Nizkorodov, and D. J. Nesbitt, J. Chem. Phys. **109**, 9306 (1998).

Y. Chen and E. Tschuikow-Roux, J. Phys. Chem. **97**, 3742 (1993).

S. Davis, University of Colorado, 1999.

F. Dong, S.-H. Lee, and K. Liu, J. Chem. Phys. **113**, 3633 (2000).

F. Dong.

F. Dong, D. Uy, S. Davis, M. Child, and D. J. Nesbitt, J. Chem. Phys. **122** (2005).

V. L. Dribinski, A. B. Potter, A. V. Demyanenko, and H. Reisler, J. Chem. Phys. **115**, 7474 (2001).

Y. Endo, C. Hamada, S. Saito, and E. Hirota, J. Chem. Phys. **79**, 1605 (1983).

Y. Endo, S. Saito, and E. Hirota, Can. J. Phys. **62**, 1347 (1984).

K. M. Evenson, H. P. Broida, J. S. Wells, R. J. Mahler, and M. Mizushima, Phys. Rev. Lett. **21**, 1038 (1968).

J. T. Farrell, Jr., S. Davis, and D. J. Nesbitt, J. Chem. Phys. **103**, 2395 (1995).

M. Faubel, S. Schlemmer, F. Sondermann, and J. P. Toennies, J. Chem. Phys. **94**, 4676 (1991).

F. Fernandez-Alonso, B. D. Bean, J. D. Ayers, A. E. Pomerantz, R. N. Zare, L. Banares, and F. J. Aoiz, Angew. Chem. Int. Eng. Ed. **39**, 2748 (2000).

R. W. Fessenden and R. H. Schuler, J. Chem. Phys. **39**, 2147 (1963).

R. W. Fessenden and R. H. Schuler, J. Chem. Phys. **43**, 2704 (1965).

B. J. Finlayson-Pitts, *Chemistry of the Upper and Lower Atmosphere: Theory, Experiments, and Applications*. (Academic, New York, 1999).

J. S. Francisco and M. M. Maricq, in *Advances in Photochemistry* (Wiley, New York, 1995), Vol. 20, pp. 79.

J. S. Francisco, J. Phys. Chem. A **104**, 1499 (2000).

M. J. Frisch, G. W. Trucks, and H. B. Schlegel, Computer Program Gaussian98 (Gaussian, Inc., Pittsburgh, 1999).

M. J. Frisch, G. W. Trucks, H. B. Schlegel, G. E. Scuseria, M. A. Robb, J. R. Cheeseman, J. Montgomery, J. A., T. Vreven, K. N. Kudin, J. C. Burant, J. M. Millam, S. S. Iyengar, J. Tomasi, V. Barone, B. Mennucci, M. Cossi, G. Scalmani, N. Rega, G. A. Petersson, H. Nakatsuji, M. Hada, M. Ehara, K. Toyota, R. Fukuda, J. Hasegawa, M. Ishida, T. Nakajima, Y. Honda, O. Kitao, H. Nakai, M. Klene, X. Li, J. E. Knox, H. P. Hratchian, J. B. Cross, V. Bakken, C. Adamo, J. Jaramillo, R. Gomperts, R. E. Stratmann, O. Yazyev, and A. J. C. Austin, R.; Pomelli, C.; Ochterski, J. W.; Ayala, P. Y.; Morokuma, K.; Voth, G. A.; Salvador, P.; Dannenberg, J. J.; Zakrzewski, V. G.; Dapprich, S.; Daniels, A. D.; Strain, M. C.; Farkas, O.; Malick, D. K.; Rabuck, A. D.; Raghavachari, K.; Foresman, J. B.; Ortiz, J. V.; Cui, Q.; Baboul, A. G.; Clifford, S.; Cioslowski, J.; Stefanov, B. B.; Liu, G.; Liashenko, A.; Piskorz, P.; Komaromi, I.; Martin, R. L.; Fox, D. J.; Keith, T.; Al-Laham, M. A.; Peng, C. Y.; Nanayakkara, A.; Challacombe, M.; Gill, P. M. W.; Johnson, B.; Chen, W.; Wong, M. W.; Gonzalez, C.; and Pople, J. A., Gaussian 03 (Gaussian, Inc., Wallington, CT, 2004).

B. C. Gilbert, M. J. Davies, and D. M. Murphy, *Electronic Paramagnetic Resonance*. (Royal Society of Chemistry, Cambridge, UK, 2002).

J. L. Hall, Appl. Phys. Lett. **29**, 367 (1976).

W. W. Harper, S. A. Nizkorodov, and D. J. Nesbitt, J. Chem. Phys. **113**, 3670 (2000).

W. W. Harper, S. A. Nizkorodov, and D. J. Nesbitt, Chem. Phys. Lett. **335**, 381 (2001).

W. W. Harper, S. A. Nizkorodov, and D. J. Nesbitt, J. Chem. Phys. **116**, 5622 (2002).

D. R. Herschbach, Angew. Chem. Int. Engl. Ed. **26**, 1223 (1987).

G. Herzberg, *Molecular Spectra and Molecular Structure III. Electronic Spectra and Electronic Structure of Polyatomic Molecules*. (Van Nostrand, New York, 1966).

E. Hirota, *High-Resolution Spectroscopy of Transient Molecules*. (Springer-Verlag, Berlin, 1985).

E. Hirota, Chem. Rev. **92**, 141 (1992).

E. Hirota, Chem. Rev. **92**, 141 (1992).

J. T. Hougen, P. R. Bunker, and J. W. C. Johns, J. Mol. Spec. **34**, 136 (1970).

K. P. Hubert and G. Herzberg, *Molecular Spectra and Molecular Structure Constants of Diatomic Molecules*. (1979).

J. W. Hudgens, C. S. Dulcey, G. R. Long, and D. J. Bogan, J. Chem. Phys. **87**, 4546 (1987).

M. E. Jacox and D. E. Milligan, J. Chem. Phys. **50**, 3252 (1969).

M. E. Jacox and D. E. Milligan, J. Chem. Phys. **53**, 2688 (1970).

M. E. Jacox, J. Phys. Chem. Ref. Data **32**, 1 (2003).

S. A. Kandel, T. P. Rakitzis, T. Lev-On, and R. N. Zare, J. Phys. Chem. **102** (2270) (1998).

S. A. Kandel, A. J. Alexander, Z. H. Kim, R. N. Zare, F. J. Aoiz, L. Banares, J. F. Castillo, and V. S. Rabanos, J. Chem. Phys. **112**, 670 (2000).

D. A. V. Kliner, D. E. Adelman, and R. N. Zare, J. Chem. Phys. **94**, 1069 (1991).

P. J. Kuntz, Mak, M. H., and Polanyi, J. C., J. Chem. Phys. **50**, 4623 (1969).

I. Last, M. Gilibert, and M. Baer, J. Chem. Phys. **107**, 1451 (1997).

S.-H. Lee, L.-H. Lai, K. Liu, and H. Chang, J. Chem. Phys. **110**, 8229 (1999).

S.-H. Lee and K. Liu, J. Chem. Phys. **111**, 6253 (1999).

S.-H. Lee, F. Dong, and K. P. Liu, J. Chem. Phys. **116**, 7839 (2002).

Y. T. Lee, Angew. Chem. Int. Engl. Ed. **26**, 939 (1987).

S. V. Levchenko and A. I. Krylov, J. Chem. Phys. **115**, 7485 (2001).

S. V. Levchenko and A. I. Krylov, J. Phys. Chem. A **106**, 5169 (2002).

S. V. Levchenko and A. I. Krylov, J. Phys. Chem. A **106**, 5169 (2002).

S. V. Levchenko, A. V. Demyanenko, V. L. Dribinski, A. B. Potter, H. Reisler, and A. I. Krylov, J. Chem. Phys. **118**, 9233 (2003).

G. C. Light, J. Chem. Phys. **68**, 2831 (1978).

J. J. Lin, J. Shu, Y. T. Lee, and X. Yang, J. Chem. Phys. **113**, 5287 (2000).

J. J. Lin, J. Zhou, W. Shiu, and K. Liu, Science **300**, 966 (2003).

K. Liu, Ann. Rev. Phys. Chem. **52**, 139 (2001).

X. Liu, J. J. Lin, S. Harich, G. C. Schatz, and X. Yang, Science **289**, 1536 (2000).

X. Liu, R. L. Gross, G. E. Hall, J. T. Muckerman, and A. G. Suits, J. Chem. Phys. **117**, 7947 (2002).

C. M. Lovejoy and D. J. Nesbitt, Rev. Sci. Instr. **68**, 807 (1987).

D. K. Maity, W. T. Duncan, and T. N. Truong, J. Phys. Chem. A **103**, 2152 (1999).

M. Maneshkarimi and H. Heydtmann, Chem. Phys. Lett. **234**, 182 (1995).

D. E. Manolopoulos, J. Chem. Soc., Faraday Trans. **93**, 673 (1997).

D. H. Maylotte, J. C. Polanyi, and K. B. Woodall, J. Chem. Phys. **57**, 1547 (1972).

A. B. McCoy and D. J. Nesbitt, (in progress).

J. P. Michaut and J. Roncin, Chem. Phys. Lett. **12**, 95 (1971).

D. R. Miller, in *Atomic and Molecular Beam Methods*, edited by G. Scoles (Oxford University Press, Inc., New York, 1988), Vol. 1.

D. E. Milligan and M. E. Jacox, J. Chem. Phys. **48**, 2265 (1968).

M. J. Molina and L. T. Molina, Annu. Rev. Phys. Chem. **47**, 327 (1996).

J. A. Mucha, D. A. Jennings, K. M. Evenson, and J. T. Hougen, J. Mol. Spec. **68**, 122 (1977).

D. J. Nesbitt and R. W. Field, J. Phys. Chem. **100**, 12735 (1996).

D. M. Neumark, A. M. Wodtke, G. N. Robinson, C. C. Hayden, and Y. T. Lee, J. Chem. Phys. **82**, 3045 (1985).

D. M. Neumark, A. M. Wodtke, G. N. Robinson, C. C. Hayden, K. Shobatake, R. K. Sparks, T. P. Schafer, and Y. T. Lee, J. Chem. Phys. **82**, 3067 (1985).

J. Nolte and H. G. Wagner, Ber. Bunsenges. Phys. Chem. **101**, 1421 (1997).

R. G. W. Norrish and G. Porter, Nature **164**, 658 (1949).

P. D. Pacey and J. C. Polanyi, J. Appl. Opt. **10**, 1725 (1971).

K. A. Peterson, D. E. Woon, and T. H. Dunning, Jr., J. Chem. Phys. **100**, 7410 (1994).

A. S. Pine, J. Opt. Soc. Am. **64**, 1683 (1974).

A. S. Pine, J. Opt. Soc. Am. **66**, 97 (1976).

J. C. Polanyi and W. H. Wong, J. Chem. Phys. **51**, 1439 (1969).

J. C. Polanyi, Faraday Discuss. **55**, 389 (1973).

J. C. Polanyi, Science **236**, 680 (1987).

A. B. Potter, V. L. Dribinski, A. V. Demyanenko, and H. Reisler, Chem. Phys. Lett. **349**, 257 (2001).

J. I. Raymond and L. Andrews, J. Phys. Chem. **75**, 3235 (1971).

E. Riedle, S. H. Ashworth, J. T. Farrell, Jr., and D. J. Nesbitt, Rev. Sci. Instr. **65**, 42 (1994).

D. C. Robie, S. Arepalli, N. Presser, T. Kitsopoulos, and R. J. Gordon, Chem. Phys. Lett. **134**, 579 (1987).

P. B. Roussel, P. D. Lightfoot, F. Caralp, V. Catoire, R. Lesclaux, and W. Forst, J. Chem. Soc. Faraday Trans. **87**, 2367 (1991).

D. J. Rush and K. B. Wiberg, J. Phys. Chem. A **101**, 3143 (1997).

A. Schiffman, W. B. Chapman, and D. J. Nesbitt, J. Phys. Chem. **100**, 3402 (1996).

M. Schwartz, L. R. Peebles, R. J. Berry, and P. Marshall, J. Chem. Phys. **118**, 557 (2003).

J. A. Seetula and I. R. Slagle, Chem. Phys. Lett. **277**, 381 (1997).

J. Shu, J. J. Lin, Y. T. Lee, and X. Yang, J. Chem. Phys. **115**, 849 (2001).

W. R. Simpson, A. J. Orr-Ewing, and R. N. Zare, Chem. Phys. Lett. **212**, 163 (1993).

W. R. Simpson, T. P. Rakitzis, S. A. Kandel, T. Lev-On, and R. N. Zare, J. Phys. Chem. **100**, 7938 (1996).

D. Smith and L. Andrews, J. Chem. Phys. **55**, 5295 (1971).

D. Smith and L. Andrews, J. Chem. Phys. **58**, 5222 (1973).

D. J. Smith, D. W. Setser, K. C. Kim, and D. J. Bogan, J. Phys. Chem. **81**, 898 (1977).

K. Stark and H.-J. Werner, J. Chem. Phys. **104**, 6515 (1996).

G. M. Sweeney, A. Watson, and K. G. McKendrick, J. Chem. Phys. **106**, 9172 (1997).

D. G. Truhlar and R. E. Wyatt, Ann. Rev. Phys. Chem. **27**, 1 (1976).

J. J. Valentini, Ann. Rev. Phys. Chem. **52**, 15 (2001).

B. Wang, H. Hou, and Y. Gu, J. Phys. Chem. **103**, 2060 (1999).

J. K. G. Watson, in *Vibrational Spectra and Structure. A series of advances.*, edited by J. R. Durig (University of Southampton, Southampton, England), Vol. 6.

J. S. Wells and K. M. Evenson, Rev. Sci. Instr. **41**, 226 (1970).

H.-J. Werner, P. J. Knowles, M. Schutz, R. Lindh, P. Celani, T. Korona, G. Rauhut, F. R. Manby, R. D. Amos, A. Bernhardsson, A. Berning, D. L. Cooper, M. J. O. Deegan, A. J. Dobbyn, F. Eckert, C. Hampel, G. Hetzer, A. W. Lloyd, S. J. McNicholas, W. Meyer, M. E. Mura, A. Nicklab, P. Palmieri, R. Pitzer, U. Schumann, H. Stoll, A. J. Stone, R. Tarroni, and T. Thorsteinsoon, MOLPRO: a package of ab initio programs (2003).

E. S. Whitney, T. Haeber, M. D. Schuder, A. C. Blair, and D. J. Nesbitt, in press (2006).

E. S. Whitney, F. Dong, and D. J. Nesbitt, J. Chem. Phys. (in press).

E. Wrede, L. Schneider, K. H. Welge, F. J. Aoiz, L. Banares, J. F. Castillo, B. Martinez-Haya, and V. J. Herrero, J. Chem. Phys. **110**, 9971 (1999).

C. Yamada, E. Hirota, and K. Kawaguchi, J. Chem. Phys. **75**, 5256 (1981).

C. Yamada, E. Hirota, and K. Kawaguchi, J. Chem. Phys. **75**, 5256 (1981).

C. Yamada and E. Hirota, J. Mol. Spec. **116**, 101 (1986).

W. T. Zemke, W. C. Swalley, S. R. Langhoff, G. L. Valderrama, and M. J. Berry, J. Chem. Phys. **95**, 7846 (1991).

D. H. Zhang and J. Z. H. Zhang, J. Chem. Phys. **101**, 1146 (1994).

D. H. Zhang and S. Y. Lee, J. Chem. Phys. **110**, 4435 (1999).

Z. Zhou, L. Guo, C. Li, and H. Gao, J. Molec. Struct. **579**, 21 (2002).

APPENDIX

This section documents the numerous computer programs used in JILA B212 for processing data files, concatenating scans, generating spectral predictions, and running least-squares fits on the data. Appendix A details the processing and concatenation programs; it comprises programs which were written before my time but, until now, have no documentation. Appendix B summarizes and directs the user to appropriate programs for generating predicted spectra and running least-squares fits on assigned line centers. Finally, Appendix C comprises my contribution to the data analysis, in the form of an extensive least-squares program used for the fitting of actual line shapes to fine and hyperfine structural parameters. Many thanks are owed to David Nesbitt as well as John Brown's group at Oxford for their assistance with exhaustive benchmark tests and comparisons with program predictions to yield agreement to machine precision.

Chandra Savage and Thomas Haeber have provided helpful reviews of these appendices, and Feng Dong deserves significant recognition for his authorship of the Origin programs.

A. PROCESSING AND CONCATENATION PROGRAMS

A.1 Introduction

If there is one service I would like to leave my successors in JILA B212, it is documentation for the processing, linearization, and spectral concatenation programs required to generate the spectral scrolls. To my knowledge, these procedures have been passed on by word-of-mouth only, and one of my biggest frustrations at the start of experiments in B212 was the lack of overlap with anyone who knew this process. To prevent future such occurrences, this section explains the necessary programs. At the start of my tenure with these experiments, this process used a series of Fortran programs on the VMS system. However, by the time I finished doing experiments, the graphing and visualization program Origin was used exclusively. Instructions for both methods are provided, including hard copies and/or locations of relevant Fortran programs and Origin scripts.

A.2 Pre-processing of data

Master copies of the Fortran 77 programs referenced here are stored in the [b212.source] directory on the JILA server. Ask anyone in B212 for login and password information. This guide is intended only to more quickly facilitate the use of these programs, and the user is advised to review the original code for a more detailed understanding. Programs may not be modified in the [b212.source] directory, but they may be copied to individual directories for use. If changes are necessary, the following compilation, linking, and execution steps are necessary,

```
for program.for
link program.obj,starg/l,nagg/l
run program
```

where "program" stands for the name of the program to change. Once recorded, the individual scans must be converted with the "newbin" program into a readable file format used by the linearization, concatenation, and printing programs. Basically, "newbin" converts the frequencies and intensities into double precision floating point numbers. Execution of the different programs simply requires typing the name of the program (i.e., "newbin"). The output of the "newbin" program adds the prefix "f" to each scan and is hereby referred to as an "fscan," indicating that the file now has the correct binary format.

For most of the programs, there also exists a "multi" counterpart (e.g., "multinewbin") which allows the user to process multiple files by invoking the program only once. The "multi" version will ask the user for the basename (the part before the dot in the filename) of the files to change and the start and stop index of the scan number, used as the file suffix.

Once converted to a readable binary format, each “fscan” needs to be processed by the “et” program. This program analyzes the etalon fringes, simultaneously recorded with the scanned data, and linearizes the frequency axis by using the FSR of the etalon. Use the “setet” program to change program parameters, e.g., the FSR. The user is asked to input internal and overall fringe numbers; at this stage, these inputs can be ignored since the purpose is simply to create a linearized output from which the fringes can be counted. The output of the “et” program adds the prefix “l” to each scan, indicating that it has been linearized, and is hereby referred to as an “lscan”. Each “lscan” can be processed by the “smbl” program, which smoothes the baseline of the scan by averaging over a certain number of points adjacent to each data point and subtracting this value from the intensity. Care must be taken when the spectrum contains particularly intense peaks because the result can be artificially negative regions of the “smoothed” baseline on either side of such peaks. The output of the “smbl” program adds the prefix “s” (e.g., smoothed) to each scan and is hereby referred to as an “sscan”. To prepare the sscan for printing, use the “uni” program. There are various parameters which can be changed in this program to vary the graphical layout of the output. Even more options are available with the “setuni” program. The “uni” program always generates a postscript file called “riedle.pst,” which is the last name of the famous author of many of these programs. Printing from the “uni” program can only be done for parts of the full spectrum for which a frequency range is specified. For final printing of the output from “uni,” type “post riedle.pst/noflag.”

Another useful processing program is “irnorm,” which normalizes the measured signal to the overall infrared power. This program is useful in determining the absolute absorbance of the signals and asks for a scale factor (default 650) which should prevent rounding errors when exporting scan data into ASCII files. Finally, the “viewlin” program is used to convert binary files into ASCII outputs which can then be imported into a spreadsheet program such as Excel, Origin, etc.

A.3 Fringe counting and spreadsheet tabulations

With these print-outs from the pre-processing steps, the fun begins. Starting from the low-frequency end of the scan and the first fully resolvable fringe, count the number of etalon fringes across the length of the scan, ending with and including the top of the fringe at the high-frequency start of the scan (scans are always performed from higher to lower frequencies). There may be counting numbers printed just below the etalon fringes; while helpful, they do need to be verified in the event that a (low intensity) fringe may have been skipped. Also be sure to record the count of the highest-frequency equally-spaced fringe, which will typically be a couple fringes less than the total number of fringes contained in the scan, and will be the fringe at which the scan is linked to the next high-frequency scan. (This last point also underscores the necessity of having sufficient fringe overlap between successive scans if one is trying to create a continuous spectrum over a certain region. However, it should also be noted, and will be explained later, that non-overlapping scans can also be linked.)

After all fringes have been counted in all relevant scans, open or create an Excel file, typically called “scanlist,” as shown in Figure A.1 (split into two panels)

for a sample chloromethyl scan. An understanding of this spreadsheet format is essential to understanding the Fortran programs which will be explained later. The most important piece of information in this spreadsheet is the free spectral range (FSR) of the marker cavity (~250 kHz) specified in cell D7, which should be verified daily and never taken off lock, if at all possible. This value calibrates the distance between etalon fringes, which is critical for accurately determining the frequency. As such, only scans with the same FSR can be concatenated.

	A	B	C	D	E	F	G	H	I
4									
5									
6								Ar+	dye
7	Scan	ref. fringe		Ar+	dye	IR	Dn/cm^{-1}	fringe #	fringe #
8	**scan0513**	**FSR**		**8.298139E-03**	**1/cm**				
9	0513.001	#1d		19429.9176	16215.7217	3214.1959	2.7974	0.0603	3337.0515
10	0513.002	#1d		19429.9172	16216.9332	3212.9840	1.5855	0.0121	3191.0549
11	0513.003	#1d	***R***	19429.9171	16218.5186	3211.3985	0.0000	0.0000	3000.0000
12	0513.004	#1d		19429.9173	16219.8632	3210.0541	-1.3444	0.0241	2837.9637
13	0513.005	#1d		19429.9174	16220.7510	3209.1664	-2.2321	0.0362	2730.9758

	J	K	L	M	N	O	P	Q	R	S
4	offset	*3000*								
5										irregularities
6	IR		# of fringes	ref. fringe			drift	et drift	join freq.	at
7	fringe #		found in file	internal #	ref. #		MHz	MHz	GHz	GHz (internal)
8										
9	3337.1117	*3337*	173	100	3264	3264	0	0		
10	3191.0669	*3191*	54	52	3189	3189	0	0		
11	3000.0000	*3000*	175	172	2997	2997	0	0		
12	2837.9878	*2838*	151	148	2835	2835	0	0		
13	2731.0120	*2731*	169	166	2728	2728	0	0		

Figure A.1 A sample "scanlist" file for chloromethyl radical data collection. The spreadsheet is split into two panels here for ease of display, and the bold numbers on the left side of each panel show how they are linked.

Column A is the datafile label. Column B is optional and contains information on which fringe was used for reference in conjunction with the wavemeter readout. Column C specifies which scan (labeled "***R***" in the figure) contains a known absolute reference line (methane, etc.) against which the frequencies of the other scans in a set can be calibrated. Columns D, E, and F are the user inputs for starting frequencies of the argon ion laser, dye laser, and wavemeter IR readings for the specified scan. It is critical here that each scan starts at the *top* of an etalon fringe, and not to either side, so that an exact starting frequency can be assigned and used in subsequent calculations.

Column G values are the frequency differences (cm^{-1}) between the starting IR frequency of each scan and that of the assigned reference scan ("***R***"). For scan 0513.001, for example, this quantity (G8) is expressed as (F8-$F$10). Column H values are the number of argon ion laser fringes separating the start of the specified scan and the start of the reference scan. For cell H8, in Figure 1, this is calculated as the frequency difference divided by the FSR, or (D8-$D$10)/$D$7. Column I is calculated similarly for the number of dye laser fringes, where the quantity is then *subtracted* from an arbitrary offset (cell K3). This arbitrary offset is also assigned to be the starting fringe number of the reference scan (cell I10). Subsequent scans are then concatenated together based on the fringe number at which they start, relative to that of the reference scan. (For ease of use, it is suggested that this offset be large enough such that the starting fringe of the lowest-frequency scan is greater than zero.) The number of dye laser fringes, as just described, is subtracted from this offset because scans typically proceed towards higher frequencies. For example, in Figure

A.1, I8=-(E8-$E$10)/$D$7+$K$3. The number of IR fringes in column J are again calculated similarly, but instead *added* to the same offset (K3) because the scans typically proceed towards lower frequencies. Again, by way of example, J8=G8/$D$7+$K$3.

The values in column J may also be used to check the stability of the FSR and the quality of the data by the extent to which they differ from integer values. An unstable FSR or sloppy wavemeter measurements of the reference fringe will yield IR fringe numbers which are very different from integers. Generally, any deviation from the correct integral number by less than 5% is acceptable (less than or equal to 0.05). Column K, then, is just the rounded value of the calculated IR fringe number in column J. For example, K8=ROUND(J8,0). Column L is the user input for the total number of fringes in the scan, as detailed at the beginning of this section, where the last fringe must be the one which is referenced by the wavemeter values in columns D, E, and F. (This is quite important !!! because, at this point, the wavemeter readouts are actually linked to the scans.) Also detailed at the beginning of this section, Column M is the count of the highest-frequency equally-spaced fringe, which will typically be a couple fringes less than the total number of fringes contained in the scan, and will be the fringe at which the scan is linked to the next high-frequency scan. By not using the very last and often distorted fringe, a non-linearity (quite typical) in the first stages of the scan is omitted. As such, Column N shifts the value from column M relative to the arbitrary offset in cells K3 and K10. For example, N8=K8-(L8-M8).

Columns P and Q refer to daily frequency drift which can be factored into the "et" programs. Although the marker cavity is quite stable, slightly different alignments from day to day lead to small changes in the absolute frequency of the fringe for the same fringe number. If a part of a spectrum is measured on different days, the same spectral region with distinctive bands needs to be measured on another day of scanning. Afterwards, the frequencies of these bands in both scans can be compared to determine the drift between days. (Ideally, this drift should be no more than 5-10 MHz.)

A.4 Concatenation with Fortran programs

Once the fringes have been counted and the spreadsheet has been completed, the user must go back to the "et" program for each scan and assign "internal reference" and "overall" fringes (from columns N and L, respectively). This process assigns relative frequencies to the scans and prepares them for concatenation. In other words, each scan is put on the same frequency scale by shifting the frequency axis according to the overall fringe number. It is advisable to again create individual print-outs with the "uni" program. Now check the overlap between adjacent scans, pick out a "joining" frequency for the two scans and note it in Column R of the spreadsheet. Both scans will be concatenated at that frequency.

To join the scans, use the joining frequencies from the "scanlist" spreadsheet. Use the "zus" program, starting with the lowest-frequency scan and concatenating the scans in the direction of increasing infrared frequency. (Note, the lowest-frequency scan will typically be the highest-numbered scan after a day of scanning since the

scanning is done in the direction of decreasing frequency). The input for "zus" will go something like this:

Input file name: sno1003.010
Join frequency: (freq from spreadsheet)
Input file name: sno1003.009
Join frequency: (freq from spreadsheet)

At the end, save the newly concatenated file and print using the "uni" program. Printing from the "uni" program can only be done for parts of the full spectrum for which a frequency range is specified.

A.5 Concatenation with Origin scripts

The necessary script for spectral concatenation in Origin is "main_et.ogs," which are available on the J network drive in the [4djn/B212 Origin] directory. This script calls upon the following subroutines (available in the same directory) which also must be accessed. While the "main_et.ogs" script can be renamed and copied to any location, the subscripts must all be in the same directory and cannot be renamed.

scanlist.ogs
openfile.ogs
DAC.ogs
reverteddigitalfilter.ogs
Fringe2GHz.ogs
relativefreq.ogs
concatenate,ogs
con_plots.ogs
modehop.ogs

The concatenation process in Origin is based on the same principles used in the VMS programs, and the only major challenge is learning the script syntax. Ths scripts are written in Origin C, a language similar to C, but with program-specific commands. Once again, this guide is meant to facilitate the concatenation process by highlighting

the main steps and key variables. However, the user is strongly advised to refer to the relevant subroutines for a more detailed understanding, especially of variables that are often not changed.

The key to using the "main_et.ogs" script is to run it in discrete parts and monitor the outputs along the way. The entire script *cannot* be run at once! The subroutine "Path and filename prefix" is run first by highlighting the text from the top of the script to just before the start of the next subroutine ("Import Raw Ascii Data") and hitting the carriage return. The filename prefix (%k) and path to the data files (%t) must be specified along with the FSR. Note that the data files must all be in the same directory. In addition, verify that the subroutines are in fact located in the directory specified by %n, as this is where Origin will look for them. This section only needs to be run once for all scans with the same file name prefix and path. If it doesn't already exist, this section creates a "scanlist" worksheet, which contains the same information as the Excel spreadsheet used for the VMS programs.

The next four subroutines can be run (i.e., highlight + carriage return) together, starting with "Import Raw Ascii Data" and ending *just before* "Calculating Relative Fringes…". This section may be run for each scan individually or in a loop. To loop over multiple scans, modify the FN inputs in the line just below the "Import Raw Ascii Data" header. In this statement, FN is the starting scan number, and "FN <= #" specifies the ending scan number ("#"). To run the loop, comment out (precede with one or more "/" characters) all lines beginning with "FN=" and un-comment (delete all the "/" characters) the line beginning with "for (FN=" as well as the "};" on the line just before "Converting channels."

The first section (beginning with “Import”) reads the raw ASCII data file, puts the scan information into the scanlist, and plots the digitized data. It also creates %kN, %kP, and %kFL files which contain the processed data. The next section (beginning with “Data Baseline”) smoothes the baseline and converts the digitized signal into actual absorbance units. In order to accomplish this, the gain must be set. Currently, its format is [Gain = a x b x c x d], where a is the signal gain on the subtractor box (1.0 to 0.2), b is the overall gain on the subtractor box (0.045 to 450), c is the output gain from the subtractor box (0.01 to 1.0), and d is the gain of the lock-in amplifier, most recently measured at 290. “DACtrue” is a flag to indicate whether analog-to-digital conversion was used and should be set to 1. The variable “SMFWHM” specifies the number of points on either side for adjacent average smoothing. For example, a value of 2 indicates 2 points on either side of each data point for a total 5-point smoothing. “Nblsm” is the parameter used in the smoothing procedure and is set to 100. The third section (beginning with “Dye Laser”) counts the number of fringes from the beginning of the scan, using the parameters “MinY” (the minimum y-value for a point to be counted as a fringe), “err” (the error in the fringe spacing), and “Step” (the estimated step size). If the fringes are strong, set “MinY” to a large value (~ 400). If the program is not picking them up, decrease the value until they are all counted. Similarly, the error and step size can be changed if fringes are missed. The fourth section linearizes the spectrum to obtain relative frequencies and plots the graph. “GHzPerCM” sets the scale of the graph according to how many GHz the user wants plotted on 1 cm of the page. “Abmin” and

"Abmax" are the minimum and maximum y-values, respectively, for the plot. If the default values don't fit all of the data on the page, change them and try again.

The next subroutine ("Calculating Relative Fringes") can only be run after all the raw data has been imported. In order for the fringe to be counted properly, the user must enter the number of missed fringes at the beginning of each scan in the "Missed No" column in the scanlist worksheet. The variable "RefFN" is the reference scan number and is the same as specified in the FN column of the scanlist worksheet. The variable "RefFringe" is also the same arbitrary offset as in the Excel spreadsheet described earlier for the VMS programs. "OffRef" is the daily frequency offset, in GHz, calculated from the reference peak.

At this point, the user should be sure to save the project before concatenating the individual scans. The two sections dealing with concatenating the data should be run separately. The first section does the actual concatenation, and the second plots the data. In order to run this section, the user must enter the starting and ending frequencies, for each scan to be joined together, in the "JointStart" and "JointEnd" columns of the scanlist worksheet. This is the same as the join frequency from the "zus" Fortran program. The variable "TotalSN" must also be changed in the script to the number of scans to be joined.

To concatenate the data and display its absolute frequency relative to a known reference line, the variable "%f_CM" should be modified to reflect the chosen reference line. Both the literature frequency as well as the relative frequency of the reference line (in GHz) are needed. The syntax is: "%f_CM = [literature freq] + (%f_GHz – [relative freq])/29.9792458. Once the user has entered the values and run

this section, Origin will copy the appropriate data from the individual scans and paste them into a single worksheet name %kall. It will then delete the original data, so be sure to save the concatenated file separately from the original.

Once the data are concatenated, there are several choices for plotting the spectrum. If the spectrum is to be plotted in GHz, set "ifGHz" to 1. For cm^{-1}, set it to 0. "GHzPerCm" sets the horizontal scale, again in terms of how many GHz (or cm^{-1} if "ifGHz" = 1) per centimeter of the paper. "AbMin" and "AbMax" set the y-scale as before. They can be the same values used previously or can be different. Finally, if the user would like to have the peaks labeled on the spectrum, choose them first using Origin's "Pick Peaks" tool, rename the resulting worksheet "Peaks" and set "LabelPeaks" = 1. Otherwise, set "LabelPeaks" to 0. This section of script will plot the concatenated data on as many graphs as necessary, based on the value of "GHzPerCm".

The final subroutine is a way of working on mode hopping. It creates the "%pTac" worksheet where one may enter the starting and ending values of the range of points that were hopped and then run the next part ("run %n\modehop.ogs") in order to cut out the specified range of data. This is a tricky procedure and can ruin your concatenation if used carelessly. Ask someone who has used it if you are unsure.

B. SPECTRAL PREDICTION AND LEAST-SQUARES FITTING PROGRAMS

B.1 Predictions

This section outlines the necessary steps for creating spectral simulations that can be compared with experimental data, followed by an overview of the program used for least-squares fitting of spectral line centers. As with the programs outlined in Appendix A, the master copies of these programs are also stored in the [b212.source] directory on JILA.

For simulations, there are currently three programs in circulation: "asy," "asydjn," and "asy2005." Their input files are identical and are shown by the following example . (The numbers preceding each line should not be included in the actual input file; they are only used here to link the respective line of input with its descriptor at the end of the input file.)

---

(1) input file (ch2f asym stretch) for asy2005
(2) 0, 20000
(3) 0.0000001, 0
(4) 1, 2
(5) 1021.0882

(6) 265.27136,30.946966,27.728436
0.00007801, 0.001133, 0.019424, 0.00000828, 0.0010260
0.00000, 0.00000, 0.00000, 0.00000, 0.00000, 0.00000, 0.00000
(7) 261.33515,30.923790,27.701996
0.00007801, 0.001133, 0.019424, 0.00000828, 0.0010260
0.00000, 0.00000, 0.00000, 0.00000, 0.00000, 0.00000, 0.00000
(8) 0., 292.999796, 292.999796, 0.
(9) 0, 20, 1
(10) 0,3000
(11) 21.0, 21.0, 21.0, 21.0
(12) 3.0, 1.0, 1.0, 3.0
(13) 2

(1) name
(2) iprint-brief(0) or full(1) output, # of points in frequency array
(3) minimum intensity saved, data in cm-1(1) or GHz (0)
(unit of all parameters should be the same, in GHz or cm-1)
(4) selection rules (1-photon =1, 2-photon = 2);
for near prolate top band type (A = 1, B = 2, C = 3)
for near oblate top, band type (A = 2, B = 3, C = 1)
(5) band origin
(6) lower state rotational constants (starting with A, B, C...)
(7) upper state rotational constants (starting with A, B, C...)
(8) energies for lowest state of each nuclear spin symmetry
(Ezo(i)=Ezo(1), if Ezo(i)=0, i=2,4)
(9) Jmin, Jmax, Jstep
(jmax will be determined automatically, if jmax is set to 0)
(10) range of frequencies saved
(11) Trot for each symmetry species (unit in K)
(Trot(i)=Trot(1), if Trot(i)=0, i=2,4)
(12) nuclear spin weight for each symmetry species:
(sw(i)=sw(1), if sw(i)=0, i=2,4)
for near prolate top (ee,oo,oe,eo)
for near oblate top (ee,eo,oo,oe)
(13) ipol
[EOB]

Starting with the earliest version of the asy programs, “asy” handles arbitrary asymmetric tops but is not 100% reliable for all limits. Therefore, a more recent program, “asydjn,” is recommended for use. The output of both “asy” and “asydjn” is the binary file “theo.dat.” To convert this output to a readable ASCII format, the

program “asypr” must then be run, creating an unsorted list of predicted frequencies and intensities known as “raus.lis.”

At this point, if one is using the Fortran programs, the “theo.dat” output may be printed as a simulation spectrum using the “uni” programs described in Appendix A. No pre-processing is necessary, in contrast to the treatment of the “scan” files. To obtain a sorted ascii version of “raus.lis,” type the command “sort raus.lis” and enter a filename of the type “*.srt” for the output file.

“Asy2005” is different from both “asy” and “asydjn” in that it does *not* create a binary “theo.dat” output file. It handles oblate or prolate tops and also makes a temperature correction for the nuclear spins (which are handled incorrectly in asy and asydjn). The ascii output of “Asy2005” is, not surprisingly, called “asy2005.dat.” There is no binary output from “asy2005,” and *this program is recommended for primary use* especially if one is *not* using the Fortran processing programs on the VMS system.

B.2 Least-squares fitting programs

To do a least-squares fitting analysis of line centers (*not* lineshapes, as will be discussed in Appendix C), use the program “asybothdjn” which requires input files of the following format called “pinfile.dat.”

```
'generating term values CH2F'
1  10  0  50  50 'A'  1
0      265.2000        0     0     1     265.2000        1
0      30.948322       0     0     1     30.948322       1
0      27.727773       0     0     1     27.727773       1
0      0.00000828      0     0     0     0.00000828      0
0      0.001026        0     0     0     0.001026        0
```

```
0     0.d0            0     0     0     0.d0            0
0     0.d0            0     0     0     0.d0            0
0     0.d0            0     0     0     0.d0            0

0     0.00007801      2     0     0     0.00007801      0
0     0.0011334       1     1     0     0.0011334       0
0     0.019424        0     2     0     0.019424        0
0     0.0d0           0     0     0     0.d0            0
0     0.d0            2     1     0     0.d0            0
0     0.d0            1     2     0     0.d0            0
0     0.d0            0     3     0     0.d0            0
9     1021.           0     0     1     0.d0            0

0     1 1 0   1 0 1   1254.640          1.    0
0     2 1 1   2 0 2   1257.7950          1.    0

9     9 2 7   7 2 5   0.          0.    5
```

The user is referred to the "Asyboth.for Information" document prepared by Miles Weida, Sept. 16, 1993 for thorough documentation of the input and programs. Variations on this program also include "asycombfit," developed by Feng Dong, which allow two upper states to be held in common while floated.

B.3 Gaussian convolutions of predictions using Origin programs

To plot Gaussian convolutions of the "asy2005.dat" output, one can use an Origin script called "GaussConvolution" which is available on the J network drive in the [4djn/B212 Origin] directory. For this procedure, the use will need the main "GaussConvolution.org" scripts, as well as the "GaussConvolutionCore.ogs" and "AsySrtImport.ogs" subroutine. All of the scripts should be in the same folder. "Gaussconvolute" cannot handle the "theo.dat" output from "asy" or "asydjn," but

can handle the “raus.lis” or “*.srt” outputs from these two programs. See the following notes for an unsorted (i.e., “raus.lis”) vs. sorted (i.e., “*.srt”) output file.

As mentioned in Appendix A, Section 5, the key to using the Origin script is to run it in discrete parts and monitor the outputs along the way. The entire script *cannot* be run at once! The first subroutine (up to and including “run.file(%p\AsySrtImport.ogs)”) should be run on the output from the “asy2005” or “asydjn” program. The user must specify “%p” as the path to the script files, “%t” as the path to the “*.srt” files, and “%k” as the file name. “Lsmin” is the minimum calculated intensity that will be imported. Ths “AsySrtImport” script will sort the data by frequency, so it can handle unsorted (raus.lis) as well as sorted (*.srt) files.

If the file is some other list of lines, import it into an Origin worksheet and run the second subroutine. In this case, “%k” is the worksheet name, and the data should be comprised of two columns, the first being frequency and the second being intensity. The script will sort the data by frequency so that the user does not have to sort it before running the convolution. The final subroutine does the actual convolution of the data and then outputs the convolution into another worksheet with the prefix “c” added to the original worksheet name (whatever “%k” is assigned to be). The important parameters are “FWHM,” the line width at half maximum, and the step size for the stimulated spectrum. Both of these values must be entered in MHz. As with the concatenation scripts, setting “IFGHz” to 1 will produce an output in GHz, and setting it to 0 yields wavenumbers.

C. LEAST-SQUARES FITTING PROGRAM FOR *LINESHAPES*

The program "erinhyperfit" is used for least-squares fits of actual CH_2F and CH_2Cl lineshapes. It is based on a core subroutine called "hyperspecatop" and is capable of handling doublet asymmetric top radicals (S=1/2) with two different non-zero nuclear spin atoms and including spin rotation, Fermi contact, dipole-dipole, and electric quadrupole interactions. As with all programs documented in these appendices, they are archived in the [b212.source] directory on the JILA server. We have performed exhaustive benchmark test on this program, including a collaborative comparison with program predictions from John Brown's group at Oxford, yielding agreement to machine precision. In the following text, the format of the input file is detailed for ease of use, and the user is referred to the program "erinhyperfit" for more a more detailed understanding of the calculations. A sample input file is attached at the end for reference.

This input file was used for CH_2F to fit one set of ground state parameters and two sets of excited vibrational state parameters (for the CH_2 symmetric and antisymmetric stretches, respectively). The opening character on line 1, assigned a

value of 0 of 1, denotes whether the program will make a line-shape prediction (1) for *one* transition or do a least-squares fitting (0) of a group of transitions. The prediction option will be discussed in more detail at the end of this section. For now, the remaining input parameters are detailed.

Lines 2-17 are ground state parameters, which are similarly repeated in lines 18-33 and 34-49 for the symmetric and antisymmetric stretch upper states, respectively. All units are in MHz, unless otherwise noted. For the ground state parameters, lines 2-9 are the rotational and centrifugal distortion constants (A, B, C, ΔN, ΔNK, ΔK, δN, δK). These are followed by fine structure (spin-rotation) terms in line 10 (ε_{xx}, ε_{yy}, ε_{zz} where x = b, y = c, and z = a). For a species of orthorhombic symmetry such as CH_2F, only the diagonal matrix elements (ε_{aa}, ε_{bb}, ε_{cc}) are non-zero and need to be considered. The spin-rotation centrifugal distortion terms follow in line 11 (Δ^S_N, Δ^S_{NK}, Δ^S_K, δ^S_N, δ^S_K).

Lines 12-14 (15-17) are the hyperfine structure terms for nucleus #1 (#2), in this case fluorine (hydrogen). The entry at line 12 (15) is the Fermi contact term, *a*, and the three entries in line 13 (16) are the dipole-dipole interaction tensor elements (T_{xx1}, T_{yy1}, T_{zz1}). Line 14 (17) comprises the electric quadropole interaction tensor terms (X_{xx1}, X_{yy1}, X_{zz1}). Lines 18-33 and 34-49 follow similarly for the two upper states.

Line 50 specifies the spin of the electron (*XS*), the spin of nucleus 1 (*XI1*), and the spin of nucleus 2 (*XI2*). The numbering of these two nuclear spins also corresponds to the ordering of the hyperfine input parameters in each of the ground and two excited states. When "erinhyperfit" is run in prediction mode, the individual

electron and nuclear spins can be set to zero or nonzero values to make predictions for a non-perturbed line center, a line with only fine structure, or a line with fully resolved hyperfine structure.

The next three groupings of input values (lines 51-54, 55-58, and 59-62) correspond to the three previous sets of input parameters for the ground and two excited vibrational states. Their values indicate whether to float "0" or fix "1" the corresponding input parameters. In the example shown, the rotational constants (A, B, and C) are floated for each of the ground and two excited states.

Line 63 is the number of *ascii* data files (in a two-column format of frequency and intensity with no headers), up to a maximum of 9, although this maximum number can easily be modified if necessary. The files are then numbered and named in the following lines (64-72). These files should be in the same directory as the program.

The rest of the program comprises the snippets of spectral data whose lineshapes are to be fit. Line 73 is detailed below as it is annotated in the example, for a sample transition $N_{Ka\ Kc\ (upper)} \leftarrow N_{Ka\ Kc\ (lower)}$.

(a) N_{upper};
(b) $K_{a\ (upper)}$;
(c) N_{lower};
(d) $K_{a\ (lower)}$;
(e) Spectrum number from which raw data originates;
(f) Symmetry of band (A = 0, B = +1, C = -1);
(g) Removes the K degeneracy (= 0 for all K, +1 for $K_{c\ (lower)} = J$, and -1 for $K_{c\ (lower)} = J-1$);
(h) M aximum $K_{(upper)}$ over which to do hyperfine calculation (= -1 for all K);
(i) Maximum $K_{(lower)}$ over which to do hyperfine calculation (= -1 for all K);
(j) Low frequency limit for data snippet from *ascii* file (as specified in *(e)*);
(k) High frequency limit for data snippet from *ascii* file (as specified in *(e)*);
(l) Number of points between *(j)* and *(k)* over which the "hyperspecatop" interpolates the calculated spectrum;

(m) Minimum transition intensity included in the calculated spectrum;
(n) experimental data offset
(o) predicted spectrum offset
(p) Band center frequency;
(q) Indicates whether to fix ("1") or float ("0") the band center frequency *(p)*;
(r) Provides the ability to hold the band center in common among more than one transition. The number entered here is the number of the transition to which this transition should be linked. For example, the transition notated in this example is the *first* transition, and it is hence not linked to any transition ("0"). However, the third transition listed is linked to the first transition and is thus assigned a value of "1" for this parameter. Because the transition are not numbered, it is suggested that the transition to which others are linked be listed first so that it is easy to find and reference.
(s) Linewidth (GHz) used in convolution of calculated spectrum;
(t) Indicates whether to fix ("1") or float ("0") the linewidth *(s)*;
(u) The same as *(r)* but for the linewidth *(s)* instead of the band center frequency;
(v) Vertical (intensity) scaling factor for the calculation. This number stretches or shrinks the calculated line shape vertically to match the experimental intensity.
(w) Indicates whether to fix ("1") or float ("0") the vertical scaling factor *(v)*. It is often useful to set the vertical scaling factor based on a preliminary (by eye) comparison of the calculated lineshape with the experimental lineshape and then fix it in the least-squares fit of the lineshapes. This process can often help the program "zero in" on a fit.
(x) Y-axis offset to adjust the baseline of the calculated lineshape to be consistent with that of the experimental lineshape.
(y) Indicates whether to fix ("1") or float ("0") the y-axis offset (see discussion for *(w)*)
(z) Flag indicating whether the entire experimental data snippet should be included in the fit.

Sample input file for CH_2F

(1) 0
(2) 265320.67
(3) 30948.03
(4) 27730.46
(5) 0.07801
(6) 1.1334
(7) 19.424
(8) 0.00828
(9) 1.026

(10) -212.03 10.97 -1040.91

(11) 0. 0.0 0.0 0. 0.

(12) 184.103
(13) -212.310 467.515 -255.205
(14) 0. 0. 0.

(15) -60.734
(16) 24.2 1.4 -25.676
(17) 0.0 0.0 0.0

(18) 261160.34
(19) 30935.23
(20) 27655.81
(21) 0.07801
(22) 1.1334
(23) 19.424
(24) 0.00828
(25) 1.026

(26) -207.06 10.14 -1046.51
(27) 0. 0.0 0.0 0. 0.

(28) 184.103
(29) -212.310 467.515 -255.205
(30) 0. 0. 0.

(31) -60.734
(32) 24.2 1.4 -25.676
(33) 0.0 0.0 0.0

(34) 261230.71
(35) 30921.20
(36) 27698.98
(37) 0.07801
(38) 1.1334
(39) 19.424
(40) 0.00828
(41) 1.026

(42) -191.48 -0.33 -1072.96
(43) 0. 0.0 0.0 0. 0.

(44) 184.103
(45) -212.310 467.515 -255.205
(46) 0. 0. 0.

(47) -60.734
(48) 24.2 1.4 -25.676
(49) 0.0 0.0 0.0

(50) 0.5 0.5 1.0

(51) 0 0 0 1 1 1 1 1
(52) 1 1 1 1 1 1 1 1
(53) 1 1 1 1 1 1 1 1
(54) 1 1 1 1 1 1

(55) 0 0 0 1 1 1 1 1
(56) 1 1 1 1 1 1 1 1
(57) 1 1 1 1 1 1 1 1
(58) 1 1 1 1 1 1

(59) 0 0 0 1 1 1 1 1
(60) 1 1 1 1 1 1 1 1
(61) 1 1 1 1 1 1 1 1
(62) 1 1 1 1 1 1

(63) 9
(64) 1 testascii011404.dat
(65) 2 test_ch2f_asym1_ascii.dat
(66) 3 test_ch2f_asym2_ascii.dat
(67) 4 test_ch2f_asym3_ascii.dat
(68) 5 test_sde0403shifted_all.dat
(69) 6 test_sde0403shifted_all2.dat
(70) 7 ascii0321shifted.all2
(71) 8 ascii_nscan0318.all
(72) 9 ascii_0317shifted.all

(73)

(a)	*(b)*	*(c)*	*(d)*	*(e)*	*(f)*	*(g)*	*(h)*	*(i)*	*(j)*	*(k)*	*(l)*	*(m)*	*(n)*	*(o)*
2	0	1	0	5	0	1	-1	-1	1335.2	1336.2	2000	0.001	0.0	0.0
		1218.6547				0	0	.0602	0	0	420.62	1	23.93	1		1
		(p)				*(q)*	*(r)*	*(s)*	*(t)*	*(u)*	*(v)*	*(w)*	*(x)*	*(y)*		*(z)*
2	1	2	0	3	1	1	-1	2	1257.0	1259.0	2000	0.001	0.0	0.0
		1021.2168				0	0	.0641	1	1	192.93	1	-1.20	1		1
0	0	1	0	1	0	1	-1	-1	1159.5	1160.5	2000	0.001	0.0	0.0
		1218.64				1	1	.074	1	1	78.70	1	-0.83	1		1
3	0	2	0	1	0	1	2	-1	1393.5	1394.5	2000	0.001	0.0	0.0
		1218.54				1	1	.060	1	1	347.0	1	7.61	1		1

```
3  2  3  1  4  1  1  2  2  1919.  1920.  2000  0.001  1919.322  0.0
       1021.22  1  2  .065  1  1  100.  0  0.0  0                 1

2  1  2  2  2  1  -1  -1  -1  511.  512.  2000  0.001  511.582  0.0
       1021.22  1  2  .065  1  1  100.  0  0.0  0                 1

0  0  0  0  -999  0  0  0  0  0  0  0  0  0  0
       0  0  0  0  0  0  0  0  0  0                              0
```

For benchmark testing, we have run the "hyperspecatop" subroutine for the 312←211 transition in CH_2F. The input parameters displayed above for the ground state and symmetric stretch excited state of CH_2F have been used, and the outputs for three scenarios are shown below. The outputs are (1) S=0, I_1=0, and I_2=0; (2) S=1/2, I_1=0, and I_2=0;; and (3) S=1/2, I_1=1/2, and I_2=0.

Output 1 (S=0, I_1=0, and I_2=0)

```
transition NU,KaU - NL,KaL
           3           1  ---            2           1
 A-type band
 NBASISU  =            4
 KMAXU =   -1.00000000000000
 A,B,C UPPER   261160.340000000        30935.2300000000
   27655.8100000000
 SPIN ROT U =   -774.079583548531       0.000000000000000E+000
 AFERMI U =    184.103000000000       -60.7340000000000
 DIP DIP U =   -127.602500000000       -12.8000000000000
 EQUAD U =   0.000000000000000E+000  0.000000000000000E+000

 upper state eigenvalues
 for N =     3.00000000000000
 S,I1,I2 =
     0.00000     0.00000     0.00000
  xn   xk   xs   xj   xi1  xf1  xi2  xf   eigv.
  3.0  1.0  0.0  3.0  0.0  3.0  0.0  3.0   573506.89537
  3.0 -1.0  0.0  3.0  0.0  3.0  0.0  3.0   593183.18432
  3.0  3.0  0.0  3.0  0.0  3.0  0.0  3.0  2436644.28175
  3.0 -3.0  0.0  3.0  0.0  3.0  0.0  3.0  2436644.51280

 NBASISL  =            2
 KMAXL =   -1.00000000000000
 A,B,C LOWER   265320.670000000        30948.0300000000
   27730.4600000000
```

```
 SPIN ROT L =   -767.817054772815       0.000000000000000E+000
 AFERMI L =    184.103000000000       -60.7340000000000
 DIP DIP U =   -127.602500000000       -12.8000000000000
 EQUAD U =   0.000000000000000E+000  0.000000000000000E+000

 lower state eigenvalues
 for N =     2.00000000000000
 S,I1,I2 =
     0.00000     0.00000     0.00000
  xn   xk   xs   xj   xi1  xf1  xi2  xf    eigv.
  2.0  1.0  0.0  2.0  0.0  2.0  0.0  2.0   407161.50724
  2.0 -1.0  0.0  2.0  0.0  2.0  0.0  2.0   416814.21724


 A-type band
 N upper  =     3.00000000000000
 K upper  =     1.00000000000000
 N lower  =     2.00000000000000
 K lower  =     1.00000000000000

 transitions consistent with band type
 and Nupper,Kupper  --- Nlower, Klower

  Eup           Elo         Kup Klo  Jup Jlo F1up F1lo Fup Flo
freq       inten

  593183.18432  416814.21724-1.0-1.0 3.0 2.0 3.0 2.0 3.0 2.0
176.36897 0.88888
 # of non-zero transitions:           1
```

Output 2 (S=1/2, I_1=0, and I_2=0)

```
transition NU,KaU - NL,KaL
           3           1  ---            2           1
 A-type band
 NBASISU  =           14
 KMAXU =   -1.00000000000000
 A,B,C UPPER   261160.340000000        30935.2300000000
   27655.8100000000
 SPIN ROT U =   -774.079583548531       0.000000000000000E+000
 AFERMI U =    184.103000000000       -60.7340000000000
 DIP DIP U =   -127.602500000000       -12.8000000000000
 EQUAD U =   0.000000000000000E+000  0.000000000000000E+000

 upper state eigenvalues
 for N =     3.00000000000000
 S,I1,I2 =
     0.50000     0.00000     0.00000
  xn   xk   xs   xj   xi1  xf1  xi2  xf    eigv.
  3.0  1.0  0.5  3.5  0.0  3.5  0.0  3.5   573321.26302
  3.0  1.0  0.5  2.5  0.0  2.5  0.0  2.5   573753.60908
  3.0 -1.0  0.5  3.5  0.0  3.5  0.0  3.5   592835.27628
  3.0 -1.0  0.5  2.5  0.0  2.5  0.0  2.5   593647.67765
  3.0  3.0  0.5  3.5  0.0  3.5  0.0  3.5  2435425.95744
  3.0 -3.0  0.5  3.5  0.0  3.5  0.0  3.5  2435426.18307
  3.0  3.0  0.5  2.5  0.0  2.5  0.0  2.5  2438263.74571
```

```
  3.0 -3.0  0.5  2.5  0.0  2.5  0.0  2.5  2438263.98409

 NBASISL  =           10
 KMAXL =   -1.00000000000000
 A,B,C LOWER   265320.670000000        30948.0300000000
   27730.4600000000
 SPIN ROT L =   -767.817054772815       0.000000000000000E+000
 AFERMI L =    184.103000000000       -60.7340000000000
 DIP DIP U =   -127.602500000000       -12.8000000000000
 EQUAD U =   0.000000000000000E+000  0.000000000000000E+000

 lower state eigenvalues
 for N =     2.00000000000000
 S,I1,I2 =
     0.50000     0.00000     0.00000
  xn   xk   xs   xj   xi1  xf1  xi2  xf    eigv.
  2.0  1.0  0.5  2.5  0.0  2.5  0.0  2.5   406958.56428
  2.0  1.0  0.5  1.5  0.0  1.5  0.0  1.5   407464.92725
  2.0 -1.0  0.5  2.5  0.0  2.5  0.0  2.5   416500.38129
  2.0 -1.0  0.5  1.5  0.0  1.5  0.0  1.5   417285.39840

 A-type band
 N upper  =     3.00000000000000
 K upper  =     1.00000000000000
 N lower  =     2.00000000000000
 K lower  =     1.00000000000000

 transitions consistent with band type
 and Nupper,Kupper  --- Nlower, Klower

  Eup           Elo         Kup Klo  Jup Jlo F1up F1lo Fup Flo
freq       inten

  592835.27628  416500.38129-1.0-1.0 3.5 2.5 3.5 2.5 3.5 2.5
176.33489 1.01546
  593647.67765  417285.39840-1.0-1.0 2.5 1.5 2.5 1.5 2.5 1.5
176.36228 0.71179
  593647.67765  416500.38129-1.0-1.0 2.5 2.5 2.5 2.5 2.5 2.5
177.14730 0.05051
 # of non-zero transitions:           3
```

Output 3 (S=1/2, I_1=1/2, and I_2=0)

```
transition NU,KaU - NL,KaL
           3           1  ---            2           1
 A-type band
 NBASISU  =           42
 KMAXU =   -1.00000000000000
 A,B,C UPPER   261160.340000000        30935.2300000000
   27655.8100000000
 SPIN ROT U =   -774.079583548531       0.000000000000000E+000
 AFERMI U =    184.103000000000       -60.7340000000000
 DIP DIP U =   -127.602500000000       -12.8000000000000
 EQUAD U =   0.000000000000000E+000  0.000000000000000E+000
```

```
upper state eigenvalues
for N =     3.00000000000000
S,I1,I2 =
    0.50000     0.50000     0.00000
 xn   xk   xs   xj   xi1  xf1  xi2  xf    eigv.
 3.0  1.0  0.5  3.5  0.5  3.0  0.0  3.0   573203.85090
 3.0  1.0  0.5  3.5  0.5  4.0  0.0  4.0   573411.39967
 3.0  1.0  0.5  2.5  0.5  3.0  0.0  3.0   573646.00464
 3.0  1.0  0.5  2.5  0.5  2.0  0.0  2.0   573906.25852
 3.0 -1.0  0.5  3.5  0.5  3.0  0.0  3.0   592777.85391
 3.0 -1.0  0.5  3.5  0.5  4.0  0.0  4.0   592869.05920
 3.0 -1.0  0.5  2.5  0.5  3.0  0.0  3.0   593650.09171
 3.0 -1.0  0.5  2.5  0.5  2.0  0.0  2.0   593663.97581
 3.0  3.0  0.5  3.5  0.5  3.0  0.0  3.0  2435395.58206
 3.0 -3.0  0.5  3.5  0.5  3.0  0.0  3.0  2435395.80996
 3.0  3.0  0.5  3.5  0.5  4.0  0.0  4.0  2435444.91870
 3.0 -3.0  0.5  3.5  0.5  4.0  0.0  4.0  2435445.14239
 3.0  3.0  0.5  2.5  0.5  2.0  0.0  2.0  2438245.67784
 3.0 -3.0  0.5  2.5  0.5  2.0  0.0  2.0  2438245.91145
 3.0  3.0  0.5  2.5  0.5  3.0  0.0  3.0  2438282.60288
 3.0 -3.0  0.5  2.5  0.5  3.0  0.0  3.0  2438282.84491

NBASISL  =           30
KMAXL =   -1.00000000000000
A,B,C LOWER   265320.670000000        30948.0300000000
  27730.4600000000
SPIN ROT L =   -767.817054772815       0.000000000000000E+000
AFERMI L =    184.103000000000       -60.7340000000000
DIP DIP U =   -127.602500000000       -12.8000000000000
EQUAD U =   0.000000000000000E+000  0.000000000000000E+000

lower state eigenvalues
for N =     2.00000000000000
S,I1,I2 =
    0.50000     0.50000     0.00000
 xn   xk   xs   xj   xi1  xf1  xi2  xf    eigv.
 2.0  1.0  0.5  2.5  0.5  2.0  0.0  2.0   406845.69419
 2.0  1.0  0.5  2.5  0.5  3.0  0.0  3.0   407037.60442
 2.0  1.0  0.5  1.5  0.5  2.0  0.0  2.0   407369.26226
 2.0  1.0  0.5  1.5  0.5  1.0  0.0  1.0   407627.79087
 2.0 -1.0  0.5  2.5  0.5  2.0  0.0  2.0   416441.19535
 2.0 -1.0  0.5  2.5  0.5  3.0  0.0  3.0   416531.23150
 2.0 -1.0  0.5  1.5  0.5  1.0  0.0  1.0   417277.84557
 2.0 -1.0  0.5  1.5  0.5  2.0  0.0  2.0   417306.06874


A-type band
N upper  =     3.00000000000000
K upper  =     1.00000000000000
N lower  =     2.00000000000000
K lower  =     1.00000000000000

transitions consistent with band type
and Nupper,Kupper  --- Nlower, Klower
```

```
  Eup           Elo         Kup Klo  Jup Jlo F1up F1lo Fup Flo
freq       inten
  592777.85391  416531.23150-1.0-1.0 3.5 2.5 3.0 3.0 3.0 3.0
176.24662 0.03027
  592777.85391  416441.19535-1.0-1.0 3.5 2.5 3.0 2.0 3.0 2.0
176.33666 0.85816
  592869.05920  416531.23150-1.0-1.0 3.5 2.5 4.0 3.0 4.0 3.0
176.33783 1.14238
  593650.09171  417306.06874-1.0-1.0 2.5 1.5 3.0 2.0 3.0 2.0
176.34402 0.81775
  593663.97581  417306.06874-1.0-1.0 2.5 1.5 2.0 2.0 2.0 2.0
176.35791 0.07204
  593663.97581  417277.84557-1.0-1.0 2.5 1.5 2.0 1.0 2.0 1.0
176.38613 0.53368
  593650.09171  416531.23150-1.0-1.0 2.5 2.5 3.0 3.0 3.0 3.0
177.11886 0.06804
  593663.97581  416531.23150-1.0-1.0 2.5 2.5 2.0 3.0 2.0 3.0
177.13274 0.00282
  593650.09171  416441.19535-1.0-1.0 2.5 2.5 3.0 2.0 3.0 2.0
177.20890 0.00355
  593663.97581  416441.19535-1.0-1.0 2.5 2.5 2.0 2.0 2.0 2.0
177.22278 0.02670
 # of non-zero transitions:          10
```